WL-TR-96-2144

ADVANCED DIAGNOSTIC TECHNIQUES DEVELOPMENT FOR SUPERSONIC AND SUBSONIC COMBUSTING FLOWFIELDS

L.P. GROSS

INNOVATIVE SCIENTIFIC SOLUTIONS, INC
3845 WOODHURST COURT
BEAVERCREEK, OH 45430-1658

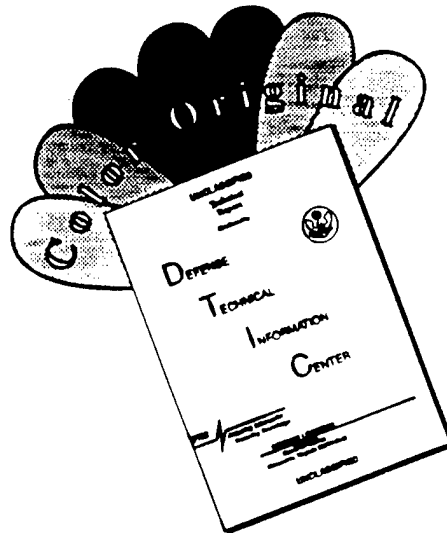NOVEMBER 1996

FINAL REPORT FOR 04/15/96-10/14/96

APPROVED FOR PUBLIC RELEASE; DISTRIBUTION IS UNLIMITED.

PLANS AND PROGRAMS DIRECTORATE
WRIGHT LABORATORY
AIR FORCE MATERIEL COMMAND
WRIGHT PATTERSON AFB OH 45433-7523

19970313 053   DTIC QUALITY INSPECTED 1

DISCLAIMER NOTICE

THIS DOCUMENT IS BEST QUALITY AVAILABLE. THE COPY FURNISHED TO DTIC CONTAINED A SIGNIFICANT NUMBER OF COLOR PAGES WHICH DO NOT REPRODUCE LEGIBLY ON BLACK AND WHITE MICROFICHE.

NOTICE

WHEN GOVERNMENT DRAWINGS, SPECIFICATIONS, OR OTHER DATA ARE USED FOR ANY PURPOSE OTHER THAN IN CONNECTION WITH A DEFINITE GOVERNMENT-RELATED PROCUREMENT, THE UNITED STATES GOVERNMENT INCURS NO RESPONSIBILITY OR ANY OBLIGATION WHATSOEVER. THE FACT THAT THE GOVERNMENT MAY HAVE FORMULATED OR IN ANY WAY SUPPLIED THE SAID DRAWINGS, SPECIFICATIONS, OR OTHER DATA, IS NOT TO BE REGARDED BY IMPLICATION, OR OTHERWISE IN ANY MANNER CONSTRUED, AS LICENSING THE HOLDER, OR ANY OTHER PERSON OR CORPORATION; OR AS CONVEYING ANY RIGHTS OR PERMISSION TO MANUFACTURE, USE, OR SELL ANY PATENTED INVENTION THAT MAY IN ANY WAY BE RELATED THERETO.

THIS REPORT IS RELEASABLE TO THE NATIONAL TECHNICAL INFORMATION SERVICE (NTIS). AT NTIS, IT WILL BE AVAILABLE TO THE GENERAL PUBLIC, INCLUDING FOREIGN NATIONS.
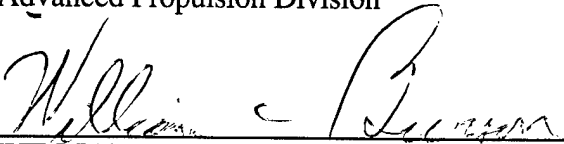
THIS TECHNICAL REPORT HAS BEEN REVIEWED AND IS APPROVED FOR PUBLICATION.

MARK R. GRUBER, PhD
Project Manager, WL/POPT
Experimental Research Branch
Advanced Propulsion Division

ABDOLLAH S. NEJAD, PhD
Acting Chief, WL/POPT
Experimental Research Branch
Advanced Propulsion Division

WILLIAM C. BURSON, PhD
Acting Chief
Advanced Propulsion Division

IF YOUR ADDRESS HAS CHANGED, IF YOU WISH TO BE REMOVED FROM OUR MAILING LIST, OR IF THE ADDRESSEE IS NO LONGER EMPLOYED BY YOUR ORGANIZATION PLEASE NOTIFY _____WL/POPT_____ WRIGHT-PATTERSON AFB OH 45433-_7251___ TO HELP MAINTAIN A CURRENT MAILING LIST.

Copies of this report should not be returned unless return is required by security considerations, contractual obligations, or notice on a specific document.

REPORT DOCUMENTATION PAGE

Form Approved
OMB No. 0704-0188

1. AGENCY USE ONLY (Leave Blank)	2. REPORT DATE 13 November 1996	3. REPORT TYPE AND DATES COVERED Final 15 April 1996 – 14 October 1996

4. TITLE AND SUBTITLE

ADVANCED DIAGNOSTIC TECHNIQUES DEVELOPMENT FOR SUPERSONIC AND SUBSONIC COMBUSTING FLOWFIELDS

6. AUTHOR(S)

L. P. Goss

5. FUNDING NUMBERS

C F33615-96-C-2638
PE 65502
PR 3005
TA PO
WU TA

7. PERFORMING ORGANIZATION NAME(S) AND ADDRESS(ES)

Innovative Scientific Solutions, Inc.
3845 Woodhurst Court
Beavercreek, OH 45430-1658

8. PERFORMING ORGANIZATION REPORT NUMBER

2638 Final

9. SPONSORING/MONITORING AGENCY NAME(S) AND ADDRESS(ES)

Aero Propulsion and Power Directorate
Wright Laboratory
Air Force Materiel Command
Wright-Patterson AFB OH 45433-7251
POC: Mark R. Gruber; WL/POPT; WPAFB OH; 937-255-4141

10. SPONSORING/MONITORING AGENCY REPORT NUMBER

WL-TR-96-2144

11. SUPPLEMENTARY NOTES

THIS IS A SMALL BUSINESS INNOVATION RESEARCH (SBIR) PHASE I REPORT.

12a. DISTRIBUTION/AVAILABILITY STATEMENT

Approved for public release; distribution unlimited.

12b. DISTRIBUTION CODE

13. ABSTRACT (Maximum 200 words)

The goal of this program was to address instrumentation problems associated with studying unsteady supersonic and subsonic combustion flows by extending the Particle Imaging Velocimetry (PIV) technique and developing surface techniques capable of pressure, temperature, and heat-transfer measurements. Optical-based non-intrusive instrumentation was designed and demonstrated in the Supersonic Combustion Tunnel at Wright Laboratory. The following tasks were accomplished: 1) Significant improvements in PIV analysis software included a new 2D-FFT correlator, a new graphic-user interface, increased capacity to read the Kodak color-camera files directly, and enhancement of post-processing routines. 2) New and improved pressure and temperature paints were developed, allowing--for the first time--measurements in diverse, high-temperature environments. The temperature range of the pressure paints was significantly increased to ~ 160°C. 3) New pressure and temperature paints were applied in the Supersonic Combustion Facility for studying fuel injectors in a Mach 2 flowfield. 4) The design of a lifetime-based pressure and temperature instrument was finalized and preliminary experiments conducted. 5) An optical heat-flux sensor based on thermographic phosphors was developed and evaluated in a backward-facing-step test apparatus. Potential applications of these techniques include testing and evaluation in the aerospace, automotive, industrial processing, and architectural industries.

14. SUBJECT TERMS

PIV, PSP, TSP, Pressure-Sensitive Paints, Temperature-Sensitive Paints, Laser Diagnostics, Optical Heat-Flux Sensor

15. NUMBER OF PAGES

68

16. PRICE CODE

17. SECURITY CLASSIFICATION OF REPORT UNCLASSIFIED	18. SECURITY CLASSIFICATION OF THIS PAGE UNCLASSIFIED	19. SECURITY CLASSIFICATION OF ABSTRACT UNCLASSIFIED	20. LIMITATION OF ABSTRACT SAR

i

Table of Contents

List of Illustrations

List of Illustrations (Continued)

Section 1

INTRODUCTION

This final report describes R&D efforts on Air Force Contract F33615-96-C-2638 during the period 15 April 1996 - 14 October 1996. Contributing to the program effort were Dr. Larry Goss of Innovative Scientific Solutions, Inc., and Prof. Mingking Chyu of Carnegie Mellon University (subcontractor).

The purpose of this Phase I SBIR program was to address the instrumentation problems associated with studying unsteady supersonic and subsonic combustion flows by extending the Particle Imaging Velocimetry (PIV) technique and developing surface techniques capable of pressure, temperature, and heat-transfer measurements. Optical-based non-intrusive instrumentation was designed and demonstrated in the Supersonic Combustion Tunnel at Wright Laboratory. A summary of progress made during this Phase I effort follows:

1. Signficant improvements in PIV analysis software were made, including a new 2D-FFT correlator, a new graphic-user interface, increased capacity to read the Kodak color-camera files directly, and enhancement of the post-processing routines. This software was employed in subsequent analysis of data taken in a Mach 2.7 wind tunnel.

2. New and improved pressure and temperature paints were developed, allowing--for the first time--measurements in diverse high temperature environments. The temperature range of the pressure paints was significantly increased to ~ 160 °C. These improvements allowed the extension of pressure paints to preheated flowfields.

3. Application of the new pressure and temperature paints in the Supersonic Combustion Tunnel was undertaken for the study of fuel injectors. The performance of fuel injectors of various geometries was examined in a Mach 2 flowfield.

4. The design of a lifetime-based pressure/temperature instrument was finalized and preliminary experiments conducted.

5. An optical heat-flux sensor based on thermographic phosphors was developed.

6. The optical sensor was evaluated in a backward-facing-step test apparatus.

Section 2

WORK ACCOMPLISHED

Improvements in PIV Software

Major modifications to the PIV analysis and post-processing software were made in attempts to read the compressed file directly, simplify the use of the software (better graphic-user interface), improve the speed of analysis, and add new features to the post-analysis software.

Reading the Compressed Kodak File Directly

The importance of reading the compressed Kodak camera file directly rather than expanding it with a graphics program such as Adobe Photoshop represents a tremendous savings in storage space for each image. The raw Kodak image is ~ 6 MBytes in size; however, this file cannot be read directly and used for PIV processing; expansion into a full (18-Mbytes) 32-bit RGB color TIFF image is required. For understanding why this operation is necessary, a discussion of the Kodak camera is in order. The Model DCS 460 camera utilizes a single CCD to record color images. This is accomplished by coating each camera element (pixel) with a red, a green, or a blue filter. Because the green color yields the best measure of brightness, the green pixels make up 50% of the camera sensor. The remaining 50% is equally divided between red and blue pixels. Achieving a full RGB image requires a multi-step process in which red, green, and blue pixels are interpolated. First the 8-bit 3072 x 2048 image (see Fig. 1) is converted into a 12-bit image by scaling with a gray response curve. Next, a pattern correction of the camera image is undertaken to account for variation in pixel-to-pixel sensitivity. The pattern correction is unique for each individual camera. Interpolation of the compressed image into three 3072 x 2048 images (red, green, and blue) is achieved using Kodak proprietary algorithms. Because green captures the luminance levels that can translate across to the red and blue planes, the green interpolation is carried out first, followed by the red and blue. The RGB images are then processed through both a toe-shoulder and gamma look-up table. The result is a color-corrected full RGB image that can be used for PIV analysis. Software for the decompression of the Kodak camera image before processing has been successfully developed by ISSI. The software subdivides the image into strips corresponding to the image width and the interrogation region height. The strip is expanded, processed, and then discarded; this eliminates the need for large disk storage.
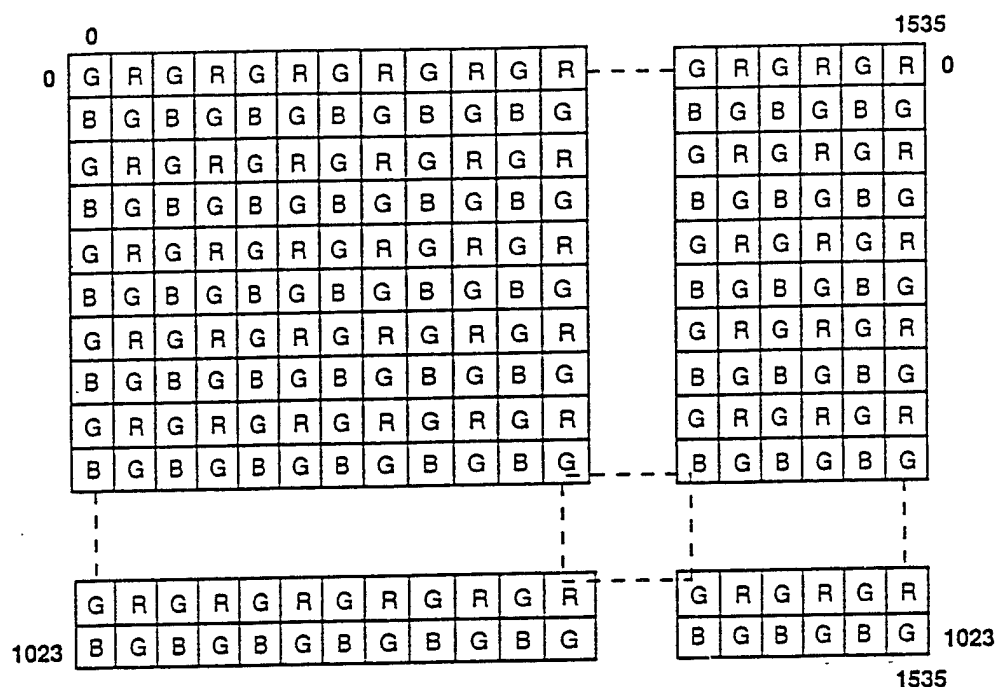
Figure 1. Color-Image Pixel Grid for DCS 460 Kodak Color Camera

Once the PIV tiff image has been obtained, it must undergo cross-correlation analysis to convert the particle images to velocity vectors. This is accomplished by the use of two-dimensional fast-Fourier-transform (2D-FFT) routines. The 2D-FFT is employed to construct the correlation map, the peak in which should correspond to the average velocity displacement in the interrogation volume of the image being processed. The interrogation volume is swept throughout the entire image and the velocity vectors determined. Once these vectors have been determined, filtering software can be used to correct for erroneous vectors resulting from poor seed levels, edges, or poor signal to noise. Typically, a nearest-neighbor filter is applied in which each velocity vector is compared to its closest eight neighbors. If the velocity vector being compared deviates excessively from its neighbors, it is made invisible and flagged for elimination. A manual filter can also be used which allows the user to hand select the vectors to be eliminated. Once vectors have been flagged for elimination, an interpolation routine can be used to replace them. The interpolation routine employs a weight average of the surrounding velocity vectors to determine the value of the new vectors.

3

Incorporation of Faster 2D-FFT

The 2D-FFT routine incorporated into the analysis software was found to be 30% faster than the previous 2D-FFT routine. Since the 2D-FFT is the major workhorse of the PIV analysis, this change resulted in a substantial improvement in the processing speed of the software.

Graphic-User-Interface Improvement

The graphic user interface of the program was significantly improved, including reorganization of the menus, a large display of the PIV image, overlay of the velocity vectors and PIV image, and introduction of image and vector printing capabilities.

Cross-Talk Improvements

Experimentally it is difficult to remove all cross-talk between the two colors used to record the PIV image because several problems are inherent in both film and color CCD sensors. Cross-talk manifests itself as a self-correlation in the correlation map, resulting in a strong zero-displacement peak. If the cross-talk is sufficiently strong, the self-correlation peak will be the dominant peak in the map, resulting in an erroneous velocity vector. The PIV image is separated into its individual red, green, and blue components by the analysis software before processing. In the case of an image displaying cross-talk, one of these color components bleeds into another (for example, red bleeds into the green image). The analysis software was modified to allow the bleeding color to be subtracted from the other colors before cross-correlation analysis occurs. This process has resulted in significant improvements in the determination of velocity vectors—especially with color film.

Addition of Correlation-Map Graphics

For improving the diagnostic capabilities, the software was modified to allow display of individual cross-correlation maps. When this mode is selected, the cursor becomes a box which can be moved to an area in the image where the user wishes to examine the correlation map. Clicking the mouse button allows the two-color components corresponding to the selected area to be displayed along with the resulting cross-correlation map. Superimposed on the map is the velocity vector determined from the map. This allows the user to pinpoint trouble areas as well as determine precisely the parameters for the cancellation of cross-talk. In both film and color CCD images, this feature was found to be of great help in understanding and diagnosing problems.

4

Incorporation of Post-Processing Software

To simplify the number of programs needed for analysis of the PIV images and for post-processing of the velocity vectors, the analysis and post-processing programs were combined. This combination allows the user to view the effects of various filters and interpolation on the velocity vectors. Also included was enhancment of the performance and usability of the post-processing software.

Displaying the Velocity Vector

Calibration of the PIV image can be directly entered, allowing the velocity vectors to be displaced in real units (meters/second). This requires that the pixels per millimeter and the time between laser pulses be measured (routinely accomplished for each experiment) and input into the program. The operator can then employ the mouse to examine the magnitude and direction of any velocity vector.

Plotting the Instantaneous Velocity Along a Row or Column

The ability to plot the velocity information obtained along a row or column of the PIV image was one of the features needed for the supersonic tests. Line plots along a user-selected row or column were, thus, incorporated to allow the operator to evaluate rapidly the quality and performance of the PIV instrument.

Plotting the Average Velocity Along a Row or Column

The ability to plot the average velocities along a row or column is also a useful tool. The PIV software was modified to allow the user to select a region of interest over which the average row or column data would be displayed.

The above modifications and improvements to the PIV analysis software represent a significant step forward in user-friendliness, performance, and diagnostic capabilities. This software greatly improved the identification of problems during experimental runs and allowed changes to be made in a timely manner.

Application of the two-color PIV technique to a supersonic wind tunnel using the new PIV analysis software was completed during this program. In cooperation with Professor Rodney Bowersox of

AFIT and Dr. Diana Glawe of WL/POPT, several PIV studies were conducted in a Mach-2.7 wind tunnel. Good agreement was obtained with velocity data taken previously with an LDV system. This cooperative effort led to five publications and presentations; these are included in the Appendix of this report.

Development of Improved Pressure and Temperature Paints

The design criteria for pressure-sensitive paints for aerodynamic applications are 1) high quantum efficiency, 2) good sensitivity to pressure changes (long lifetimes), 3) good photostability, 4) ease of application, 5) availability of excitation and detection sources, 6) insensitivity to temperature changes, and 7) rapid response to pressure changes. Understanding the origin of these goals requires a discussion of basic pressure-paint physics. Pressure paints respond to pressure changes through the quenching effect of molecular oxygen. The emission of luminescent molecules (fluorescent or phosphorescent) is quenched by collisional energy transfer with molecular oxygen. Because the oxygen partial concentration varies with pressure, the luminescent quenching is a measure of total pressure. The dynamic quenching of pressure probe molecules (luminescent paints) is given by

$$\frac{I_o}{I} = \frac{\tau_o}{\tau} = 1 + K_q Q \tag{1}$$

where Q is the concentration of quencher molecules (oxygen partial pressure), K_q the bimolecular quenching coefficient, and τ_o the unquenched lifetime of the fluorophore. From this equation the basic nature of the paints can be identified. First, as the partial pressure of oxygen increases, the luminescent signal level decreases; thus, pressure measurements are the result of ratioing the signal strengths for an unknown and a known pressure condition. Second, the lifetime of the probe molecule directly affects the sensitivity of the paint to pressure, i.e., the longer the lifetime of the paint, the more likely the occurrence of a quenching collision with oxygen. Phosphorescent and long-lived fluorescent compounds are, thus, the optimum paint candidates. Third, K_q is a measure of the efficiency of quenching during a collision with oxygen; K_q is a function of temperature and viscosity and is given by

$$K_q = 8RT/3000\eta \tag{2}$$

K_q contains effects due to the binder; thus, the behavior of pressure paints is affected not only by the fluorophore used for luminescence but also by the binder in which the fluorophore is suspended.

6

Notice also that Eq. (2) predicts that pressure paints will be sensitive to temperature. Pressure paints are sensitive to temperature in another way--through the solubility of oxygen in the binder. The solubility of oxygen in a silicone binder is given by Henry's Law

$$[O_2(T)] = [O_2]_0 \exp(- \Delta H/RT) \tag{3}$$

where ΔH is the enthalpy of solution (- 3.0 kcal/mole for silicone). Because the oxygen solubility of the binder is a function of temperature, care must be taken in choosing the correct binder to minimize this effect. Figure 2 displays the effects of temperature on both the dynamic and the static quenching processes in solution. Note that as the temperature increases, the sensitivity of the luminescence to quencher concentration (oxygen, in the present case) increases. Thus, if the binder used in the paint displays a strong temperature sensitivity, then the temperature must be monitored simultaneously with pressure to ensure accurate measurements.

The objective of this research was to determine the optimum paint formulation that can be applied to a wide range of supersonic flowfields. Because of the need to heat the inlet air to the Supersonic Combustion Tunnel (Bldg. 18), the tunnel walls are likely to experience a wide range of temperatures. Thus, paints that could withstand large temperature excursions were needed. High temperatures not only degrade the performance of pressure paints but also lead to their destruction. Fluorescence-based pressure paints are less sensitive to temperature changes but are subject to sublimation and eventual destruction. Phosphorescent paints are more sensitive to temperature changes and, thus, were not investigated further.

At temperatures below 150°C, sublimation of the fluorophore of the pressure paint is the most significant problem. For circumventing this problem, the acid forms of the standard fluorescent fluorophore were evaluated for pressure sensitivity (see Figs. 3 - 6). All acid derivatives of the fluorophore, with the exception of the carboxylic-acid form, exhibited good pressure sensitivity. Because of the relatively short natural lifetime of the carboxylic-acid form of the fluorophore (15 ns), its sensitivity to oxygen quenching is greatly reduced. The natural lifetime of the other fluorophores was ~ 300 ns.

7

Collisional Quenching

(F^*)

f(t) $G = \tau_0^{-1}$ $k_q[Q]$

Q

Q

Static Quenching

F^* $(F{\cdot}Q)^*$

hv $\Gamma = \tau_0^{-1}$ (No Emission)

$F + Q$ $\rightleftharpoons$ $F{\cdot}Q$

K_s

Higher
Temperature

F_0/F and τ_0/τ

Slope = $k_q\tau_0 = K_0$

[Q]

Higher
Temperature

Slope = K

F_0/F

τ_0/τ

[Q]
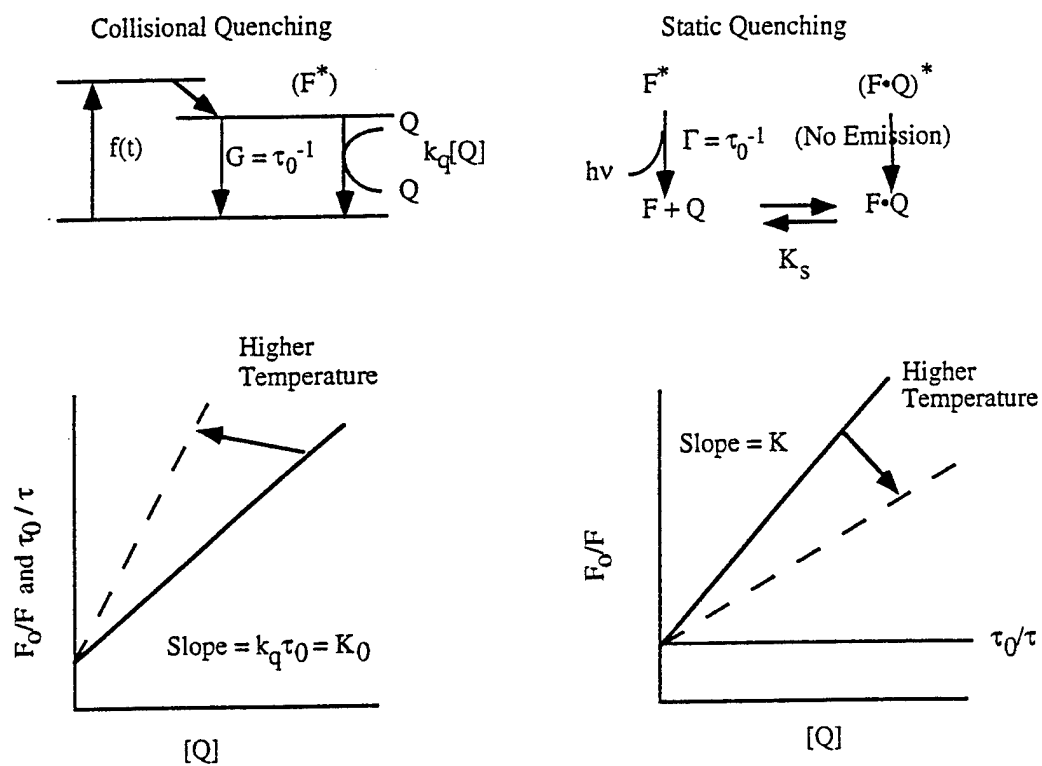
Figure 2. Effects of Temperature on Both Dynamic and Static
Quenching Processes in Solution.

8
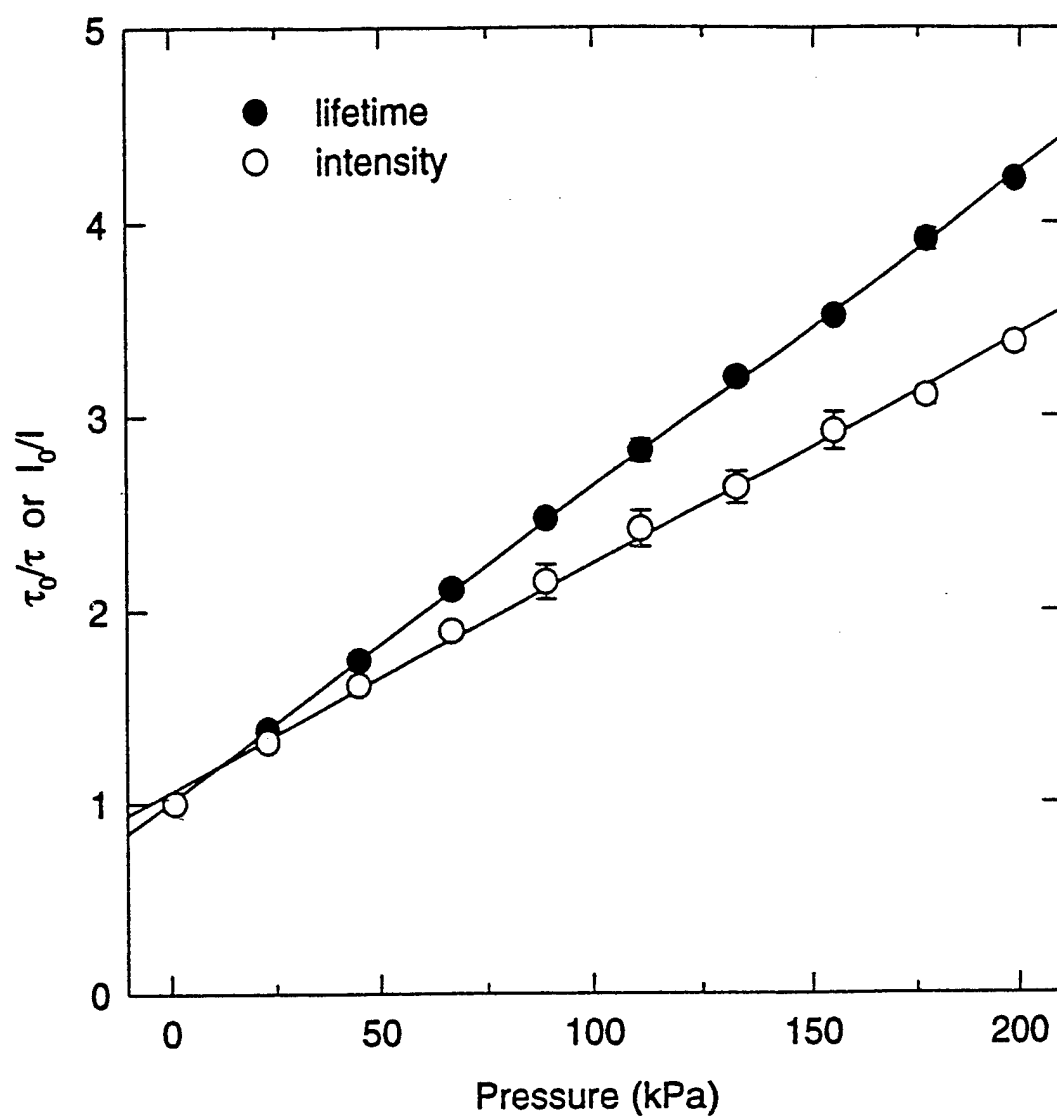
Lifetime

b[0]. 1.0062404633
b[1]. 0.0163331418
r². 0.9996837685

Intensity

b[0]. 1.0580260085
b[1]. 0.0118598974
r². 0.9974302382

Figure 3. Stern-Volmer Plot for Standard Fluorophore in Silicone Binder for Both Lifetime- and Intensity-Based Measurement Approaches.
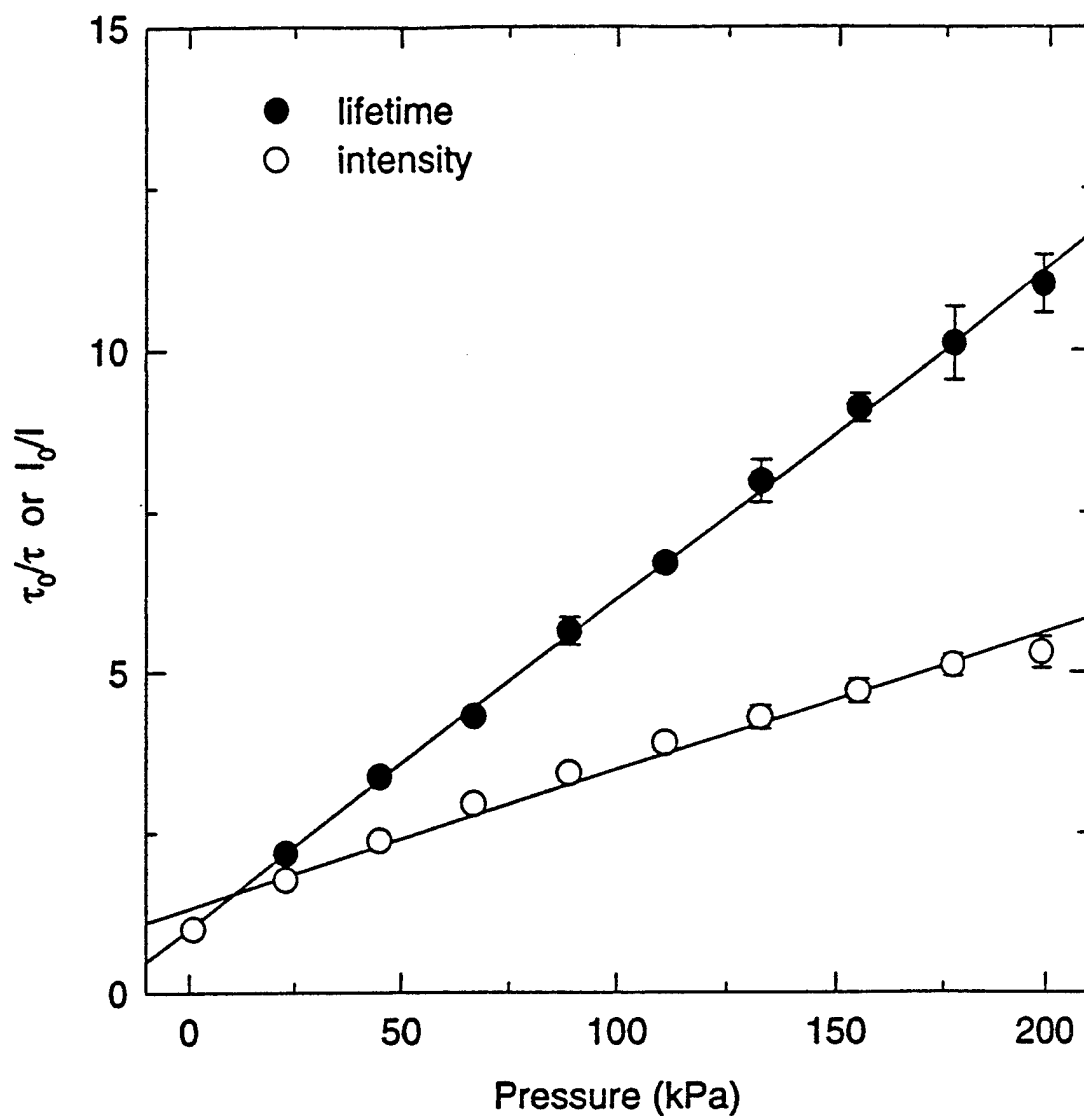
Lifetime	Intensity
b[0], 1.0040608499	b[0], 1.3233601121
b[1], 0.0513979131	b[1], 0.0215662157
r², 0.9990058033	r², 0.9828816288

Figure 4. Stern-Volmer Plot for Acetic-Acid Form of Standard Fluorophore in Silicone
Binder for Both Lifetime- and Intensity-Based Measurement Approaches.
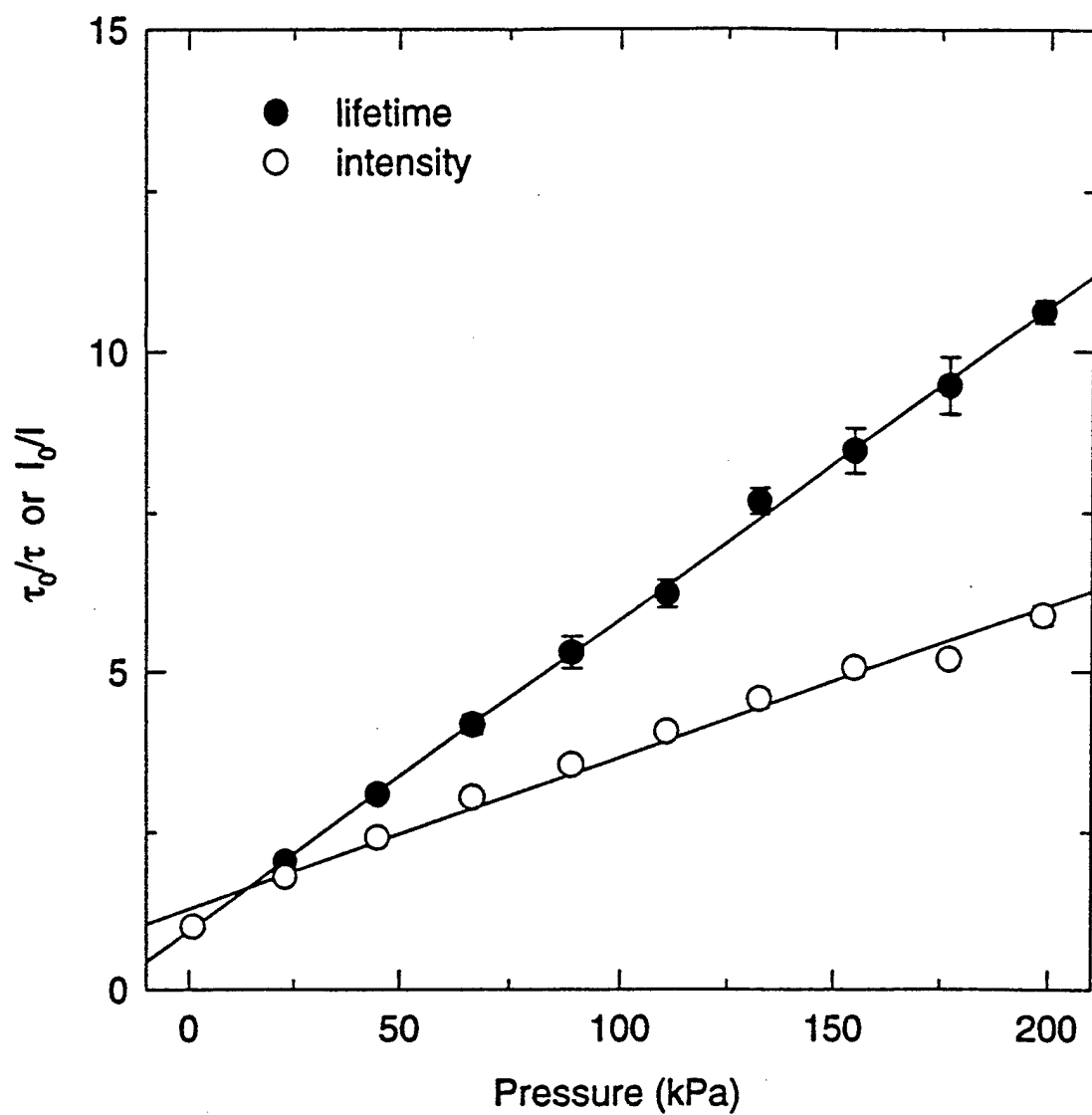
Figure 5. Stern-Volmer Plot for Butyric-Acid Form of Standard Fluorophore in Silicone Binder for Both Lifetime- and Intensity-Based Measurement Approaches.

Lifetime	Intensity
b[0], 0.9298402089	b[0], 1.2825992116
b[1], 0.0487625561	b[1], 0.0237446055
r^2, 0.9989250196	r^2, 0.9870290003

Lifetime
b[0], 1.0130687923
b[1], 2.2358056114e-3
r², 0.9901055292

Intensity
b[0], 1.0145483454
b[1], 2.0524974435e-3
r², 0.9883732893

Figure 6. Stern-Volmer Plot for Carboxylic-Acid Form of Standard Fluorophore in Silicone Binder for Both Lifetime- and Intensity-Based Measurement Approaches.

For determining the effects of temperature on the new paint formulations, the acetic-acid form was chosen for long-term heating experiments. This form of the pressure-se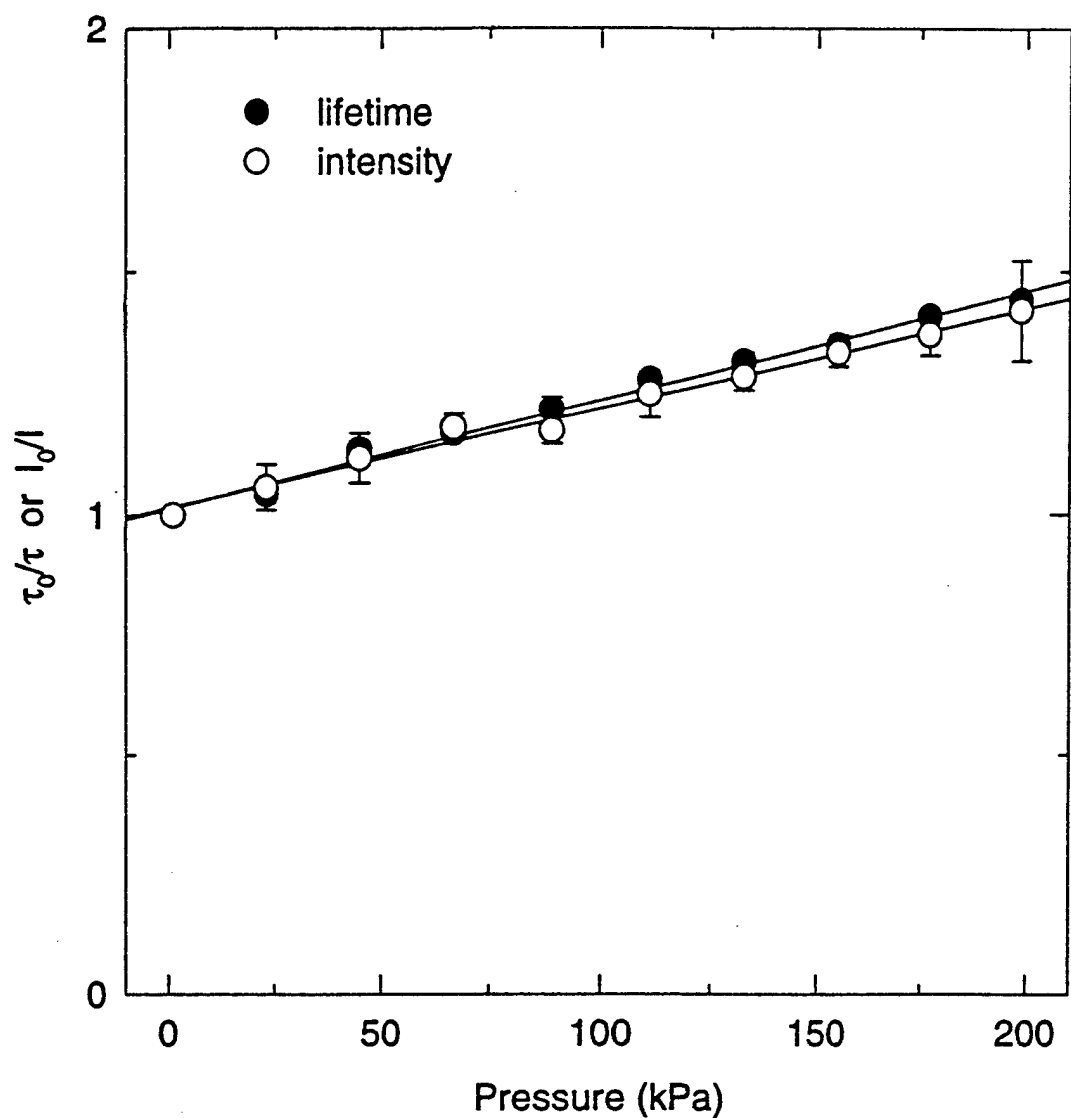nsitive fluorophore has a melting point ~ 80 °C higher than that of the standard form. Because the wall temperatures of the supersonic tunnel are expected to reach 150°C, this temperature was chosen for testing the new paint formulation. The standard form of the pressure paint would be destroyed within seconds at this elevated temperature. The new paint formulation was subjected to a short-term (30-min.) and a long-term (13-hr.) exposure to the elevated temperature and then re-evaluated for pressure sensitivity. The results are shown in Figs. 7 - 8. The paint exhibited no adverse effects from the long-term heat exposure. The overall loss in sensitivity was ~ 10% for lifetime-based measurements and ~ 20% for intensity-based measurements after 13 hr. Considering the extreme temperatures and time periods used in this study, the performance of the paint is quite remarkable. The acetic-acid form is a good candidate for pressure measurements in the supersonic facility discussed below.

Supersonic Combustion Tunnel Tests

Supersonic-fuel-injector pressure fields were measured in the Wright Laboratory Supersonic Combustion Tunnel. Several fuel injectors were studied during these tests. A nitrogen-gas laser was employed to excite the pressure-sensitive paint (PSP) surrounding the fuel injector. The fluorescence emission from the paint was captured with an intensified CCD array (Photometrics). Synchronization electronics were used to coordinate the firing of the laser and the capture of the fluorescence signal by the ICCD camera. During each tunnel run several different images were obtained. First a background image was taken to account for the thermal noise of the camera electronics. Second, a wind-off image was acquired to facilitate the conversion to pressure. Third, images were obtained at different injection pressures for studying the interaction of the transverse jet injection and the Mach-2 crossflow. Multiple images were taken under each injection condition to allow the study of transient events. The temporal behavior of the pressure paint is determined by the 500-ps laser pulse and the 50 - 300 ns fluorescence of the pressure-probe molecule. Pressure response in excess of 2 kHz is possible with the fluorescence-based pressure paints. Three fuel injectors were studied using different pressure- and temperature-sensitive (TSP) paint formulations. These measurement results are discussed below.

Circular Fuel Injector. Results of pressure measurements on the surface surrounding the circular injector are shown in Figs. 9(a), 9(b), 9(c), and 9(d). The injection air pressures were 23.8, 47.6, 71.3, and 95.2 psi, respectively. As can be seen in this figure, increasing the injection pressure results in an increase in jet spreading angle and strength of the bow shock. The pressure range
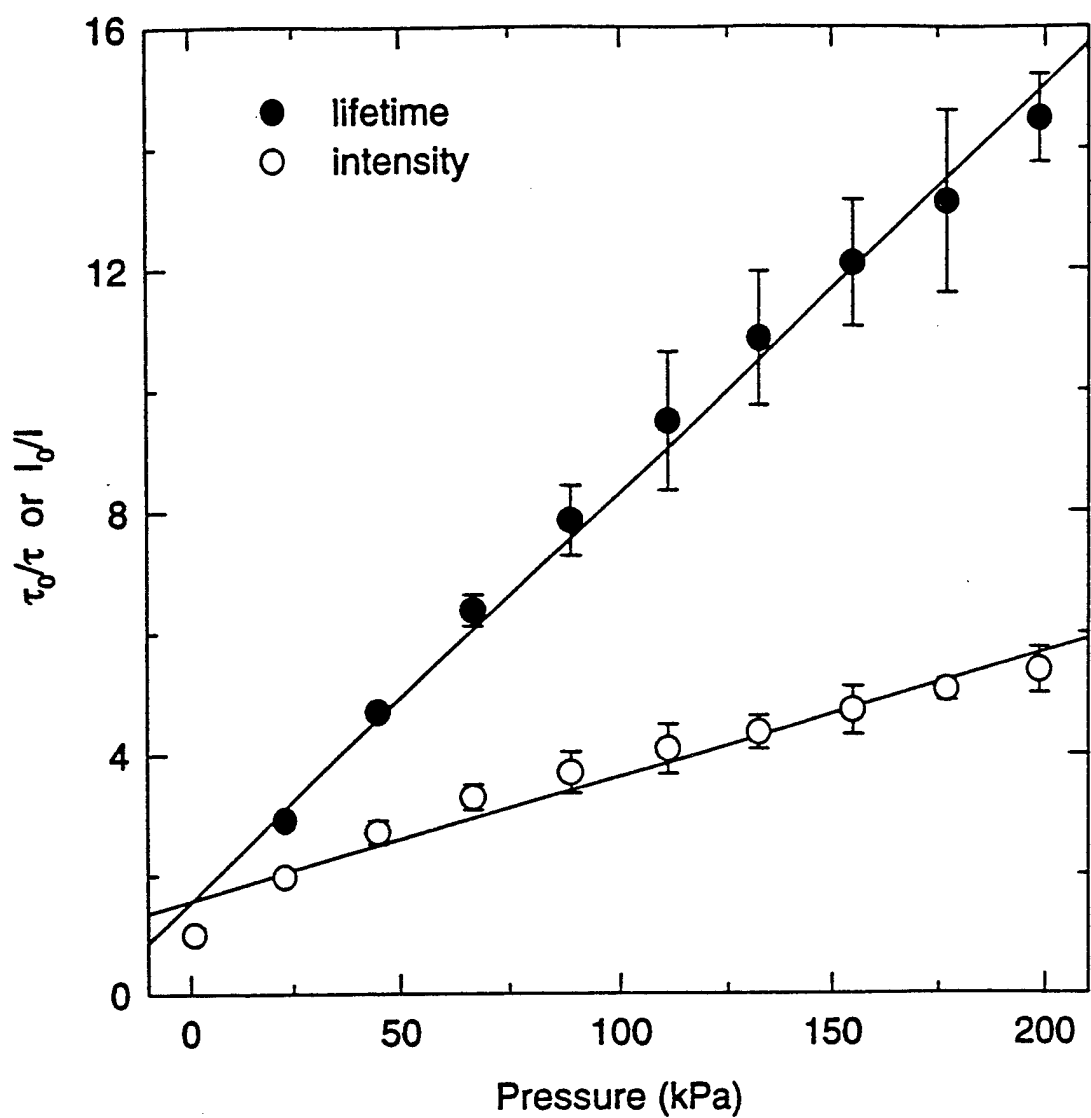
13

Lifetime	Intensity
b[0], 1.5431186485	b[0], 1.5682404531
b[1], 0.0675499715	b[1], 0.0206092021
r^2, 0.9928722065	r^2, 0.9568010574

Figure 7. Stern-Volmer Plot for Acetic-Acid Form of Standard Fluorophore in Silicone Binder After Heating at 150°C for 30 min.

14
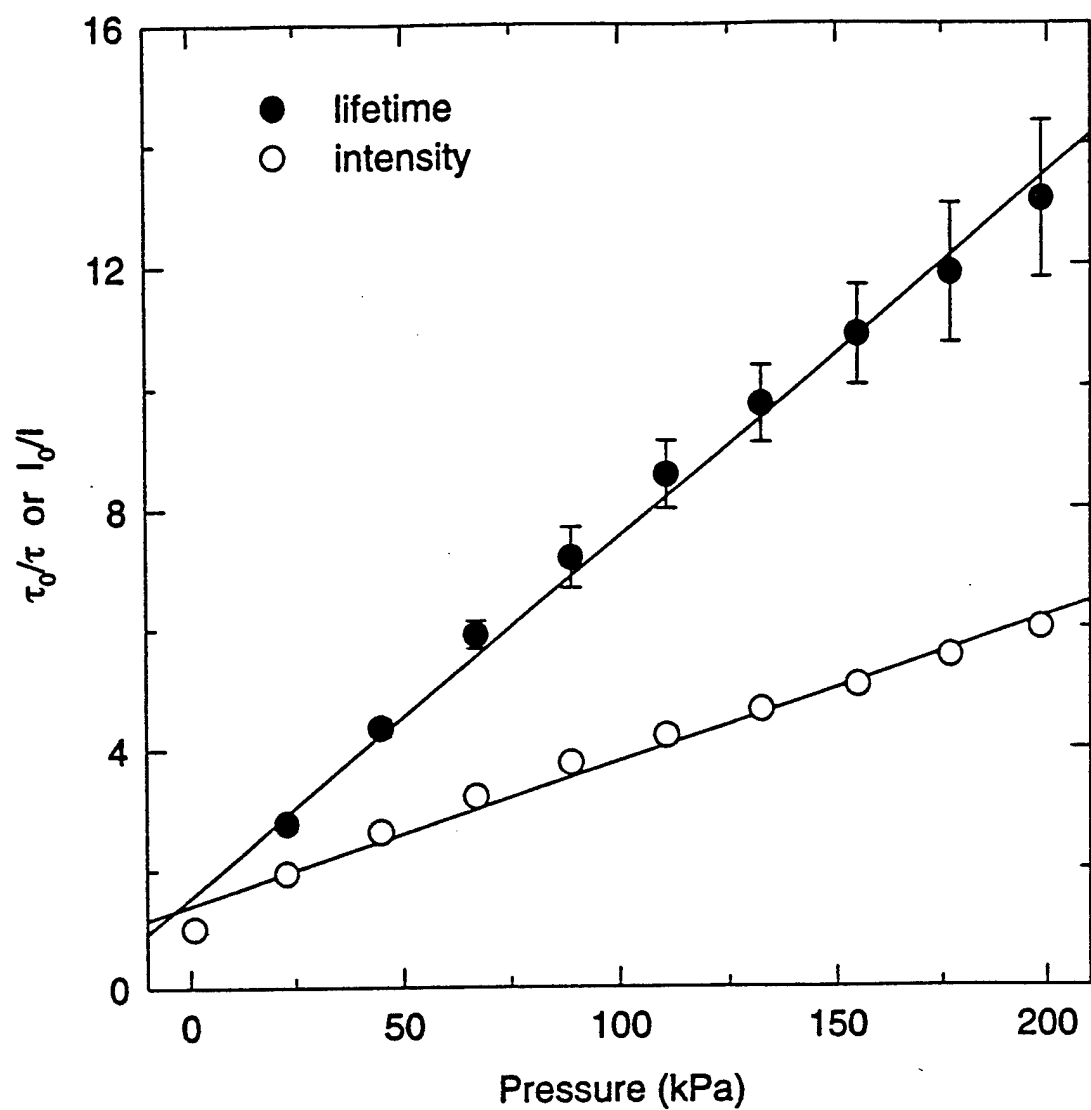
Lifetime
b[0], 1.5282683215
b[1], 0.0600485731
r², 0.9930045287

Intensity
b[0], 1.3974264771
b[1], 0.0240019775
r², 0.9843666563

Figure 8. Stern-Volmer Plot for Acetic-Acid Form of Standard Fluorophore in Silicone Binder After Heating at 150°C for 13 hr.

15
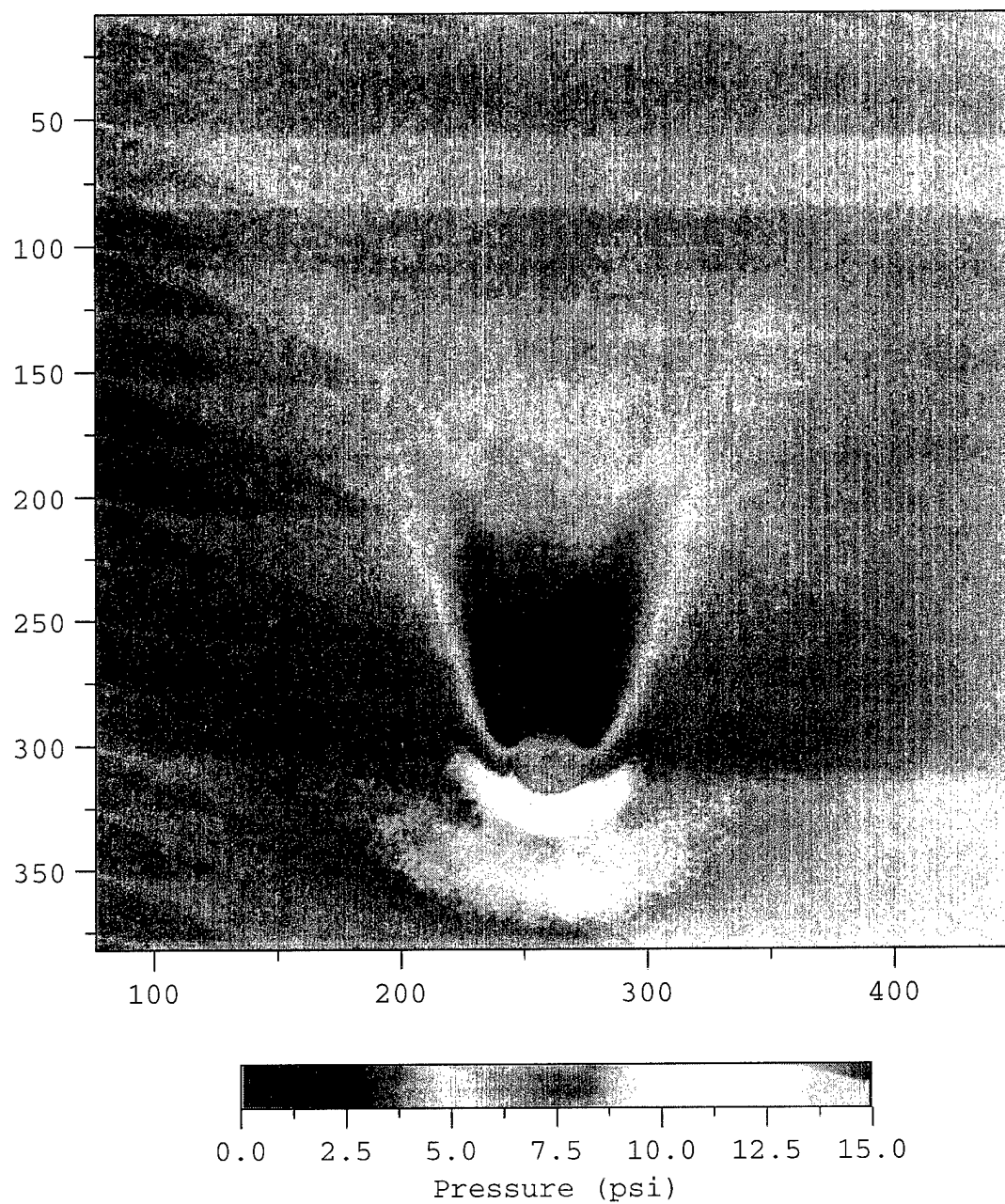
Figure 9(a). Pressure Field Surrounding Circular Injector at
Injection Pressure of 23.8 psi.

Figure 9(b). Pressure Field Surrounding Circular Injector at
Injection Pressure of 47.6 psi.

Figure 9(c). Pressure Field Surrounding Circular Injector at
Injection Pressure of 71.3 psi.

18

Figure 9(d). Pressure Field Surrounding Circular Injector at Injection Pressure of 95.2 psi.

encountered in the tunnel was from 3 to 15 psi, with the lowest pressure occurring downstream of the fuel injector and the highest occurring upstream. The images shown in Fig. 9 are the average of 10 individual laser shots. The high signal-to-noise ratio of the experiment ensured the fidelity of the data. The pressure was determined from each image by subtracting a background and dividing by the wind-off image. The resulting ratioed image was converted to pressure using the calibration curve shown in Fig. 10. The large slope of this Stern-Volmer curve helped to ensure good pressure sensitivity over the entire pressure range of interest.

Elliptical Fuel Injector. Results of the pressure measurements made with the elliptical fuel injector are shown in Figs. 11(a)-11(d). The injection pressures were the same as those used in the circular-injector study discussed above. The elliptical injector displays characteristics similar to those of the circular injector, including a wide jet-spread angle and high shock strength. The calibration curve for this study was the same as that shown in Fig. 10. The pressure field surrounding the fuel injector varied from 3 to 20 psi.

$y = -3.4843 + 20.501x - 2.0566x^2$ $R^2 = 0.999$
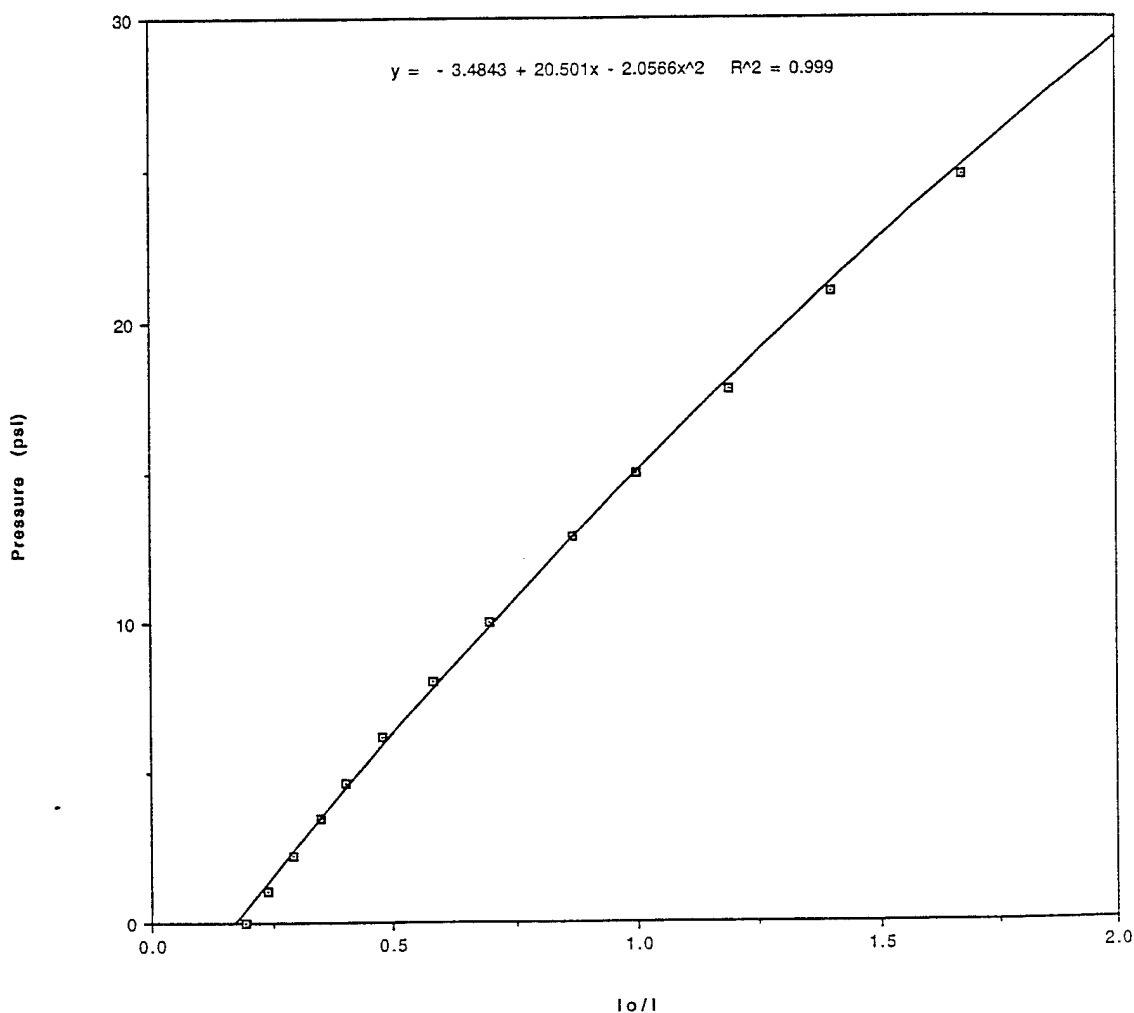
Figure 10. Stern-Volmer Calibration Curve for Pressure Paint Used in Tunnel Experiments.
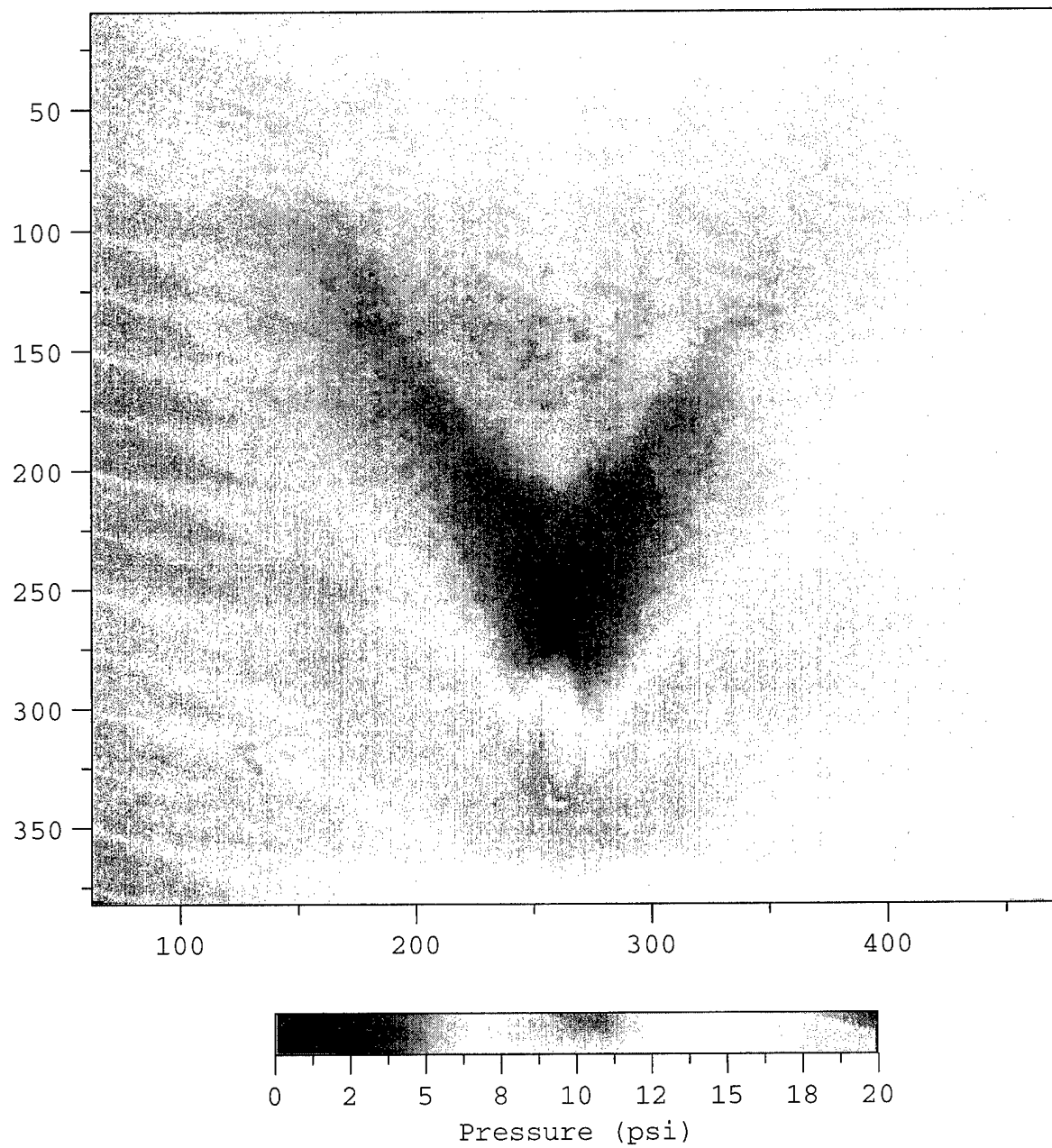
Figure 11(a). Pressure Field Surrounding Elliptical Injector at
Injection Pressure of 23.8 psi.

21
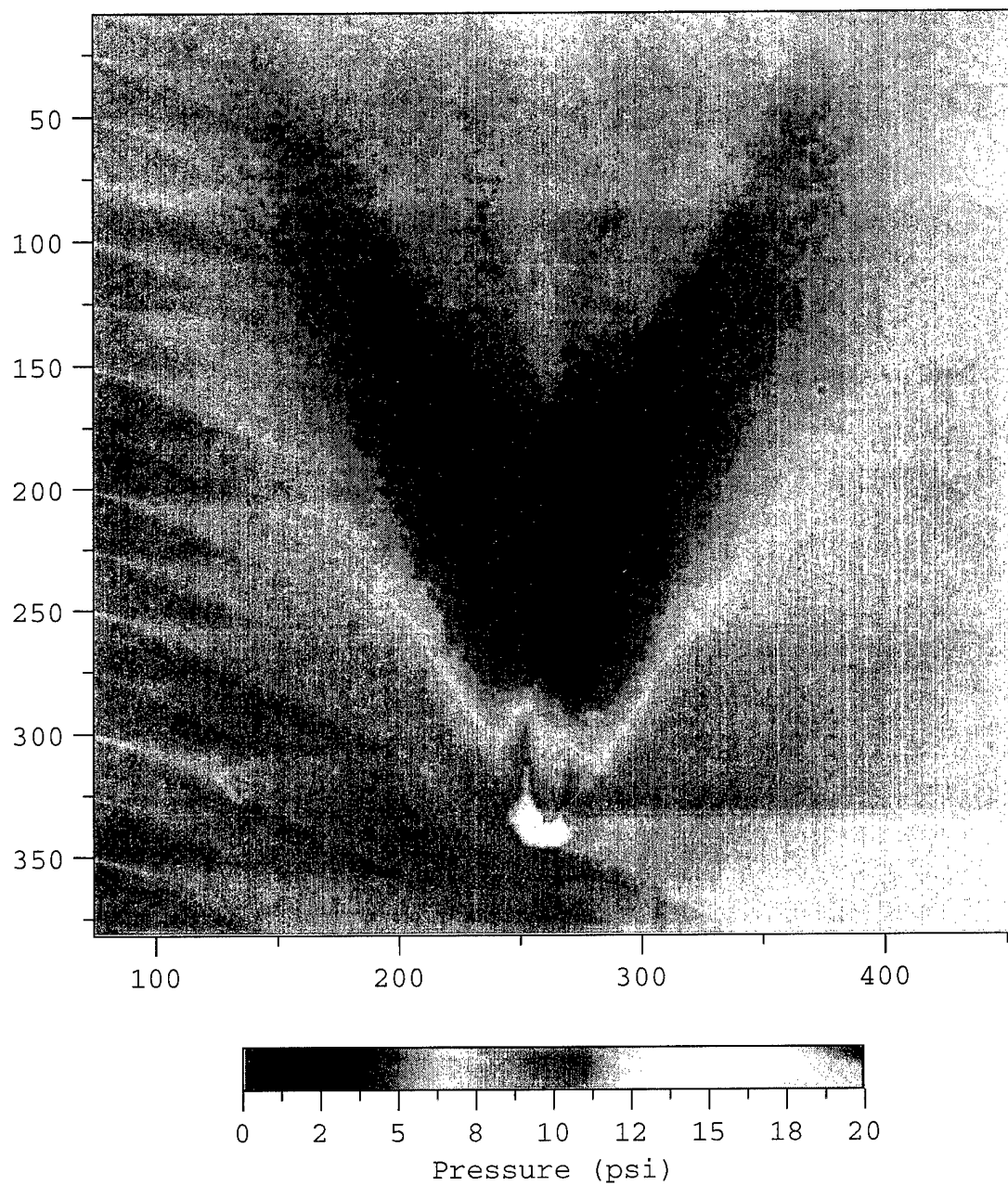
Figure 11(b). Pressure Field Surrounding Elliptical Injector at
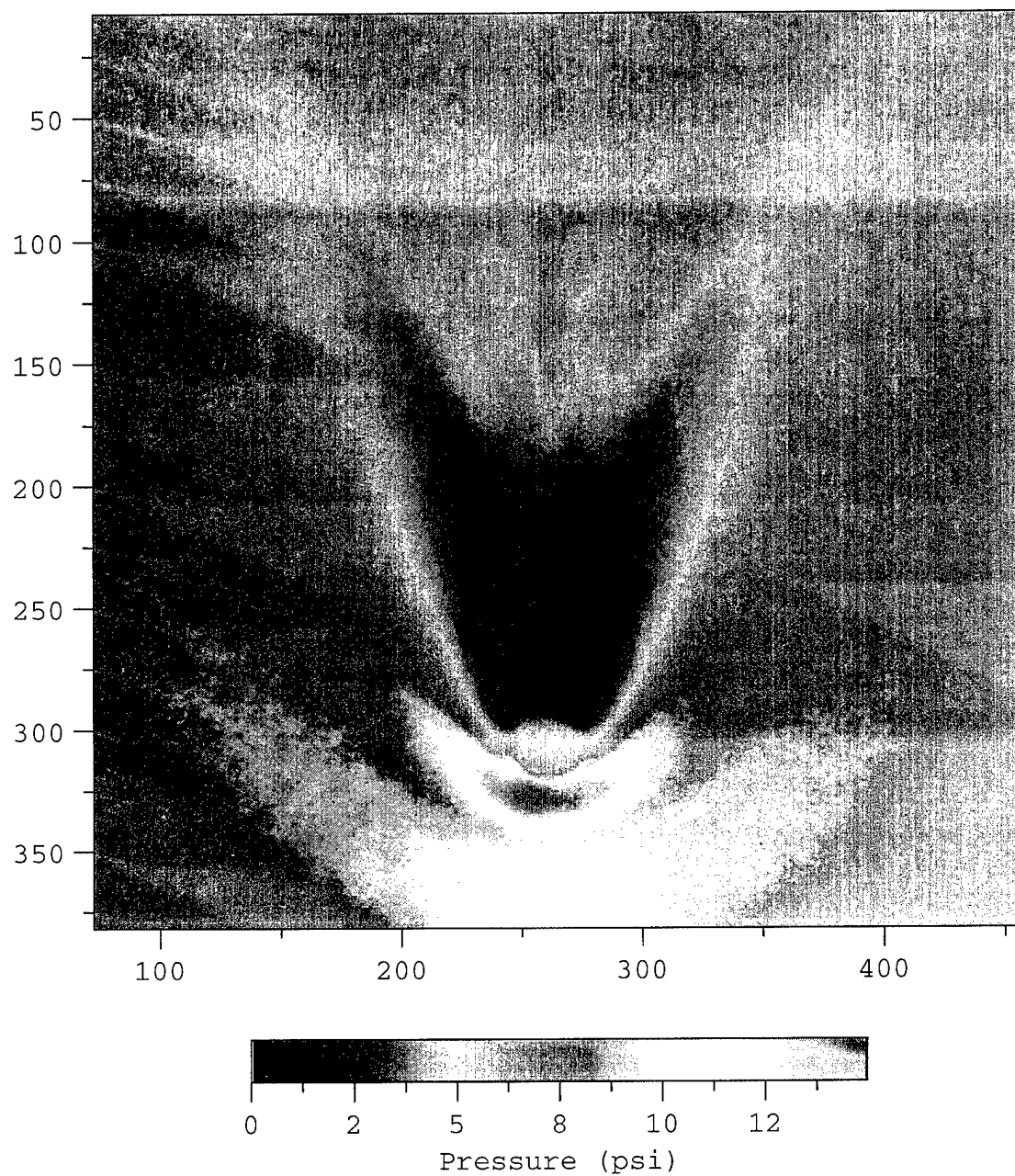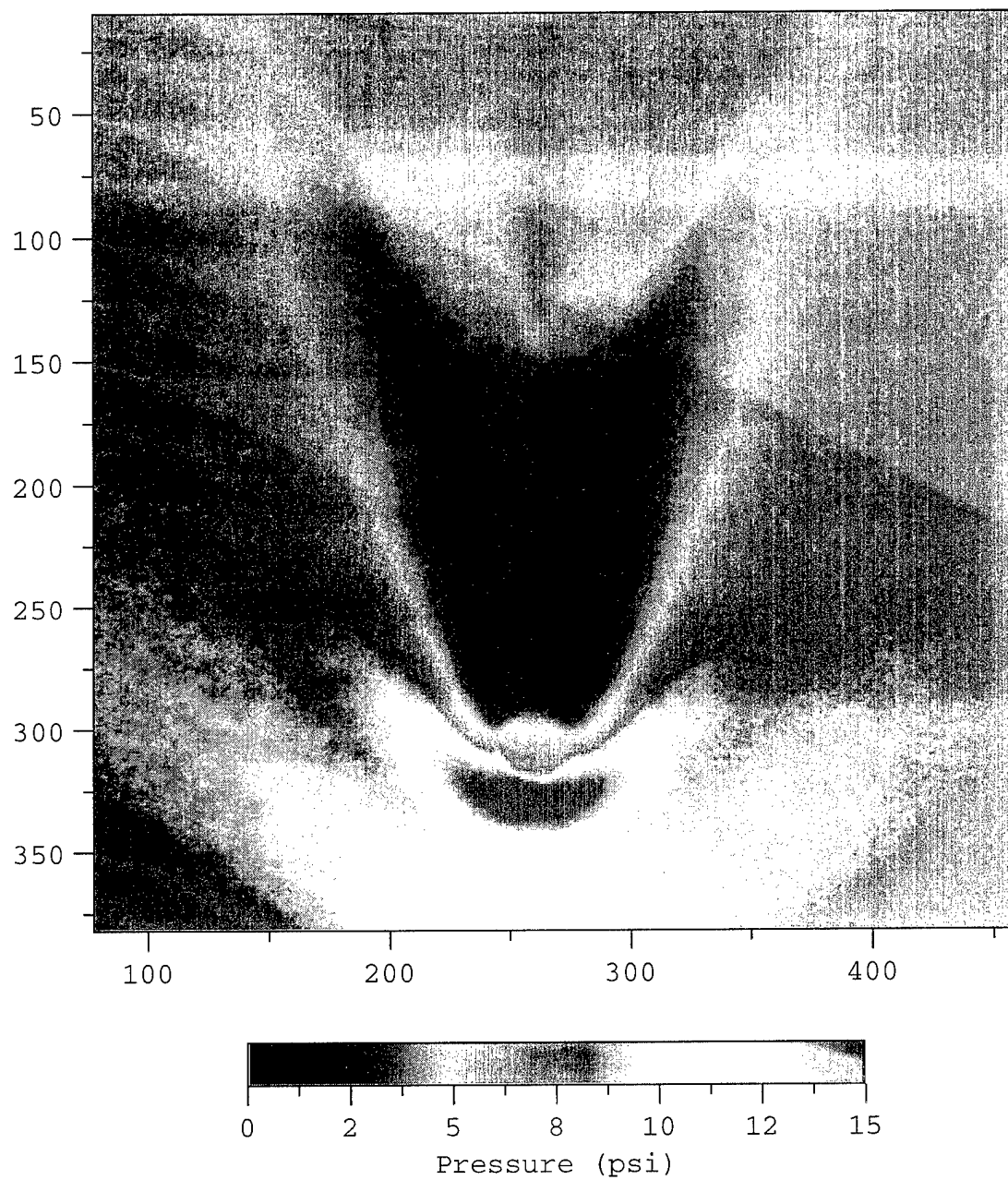Injection Pressure of 47.6 psi.
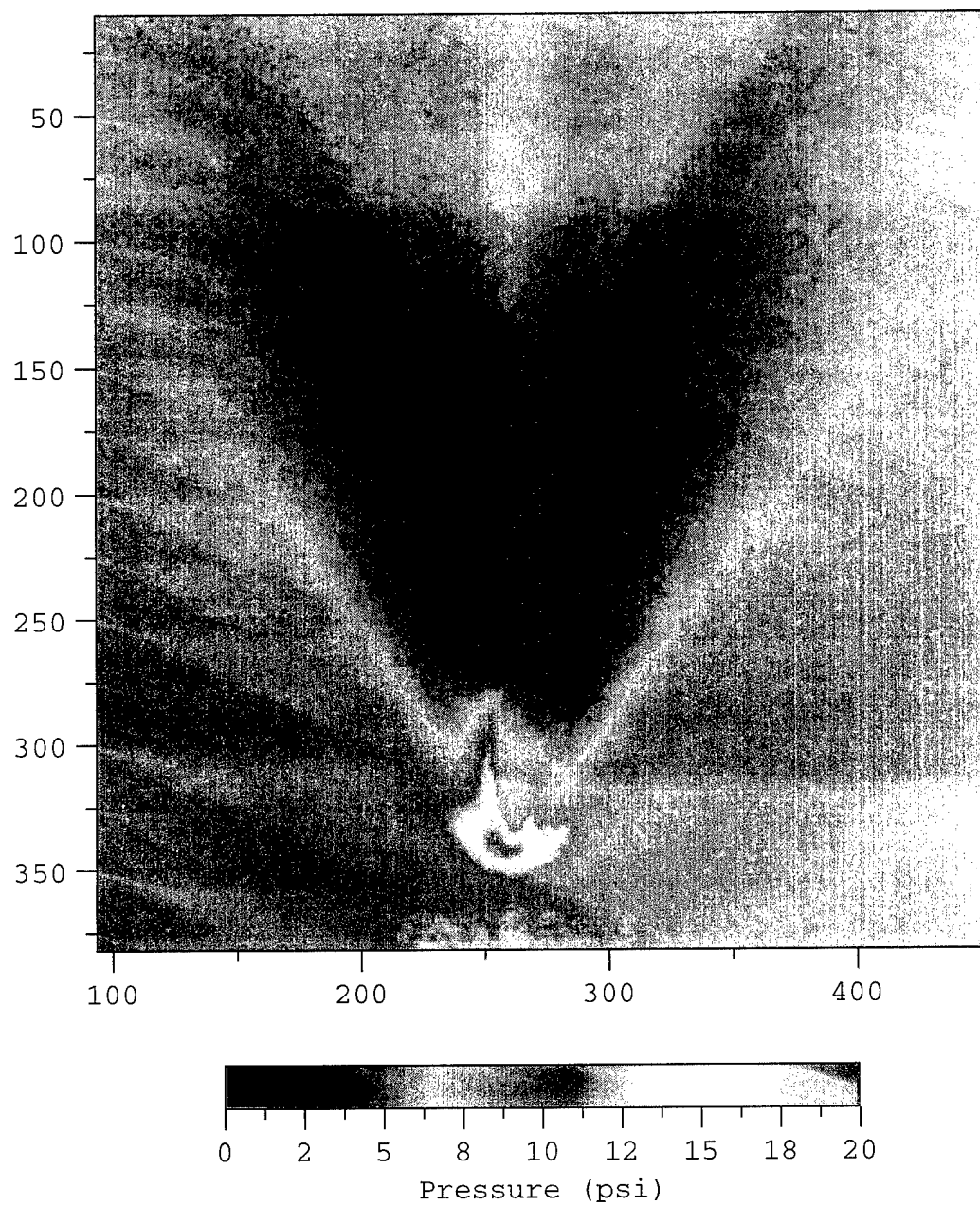
Figure 11(c). Pressure Field Surrounding Elliptical Injector
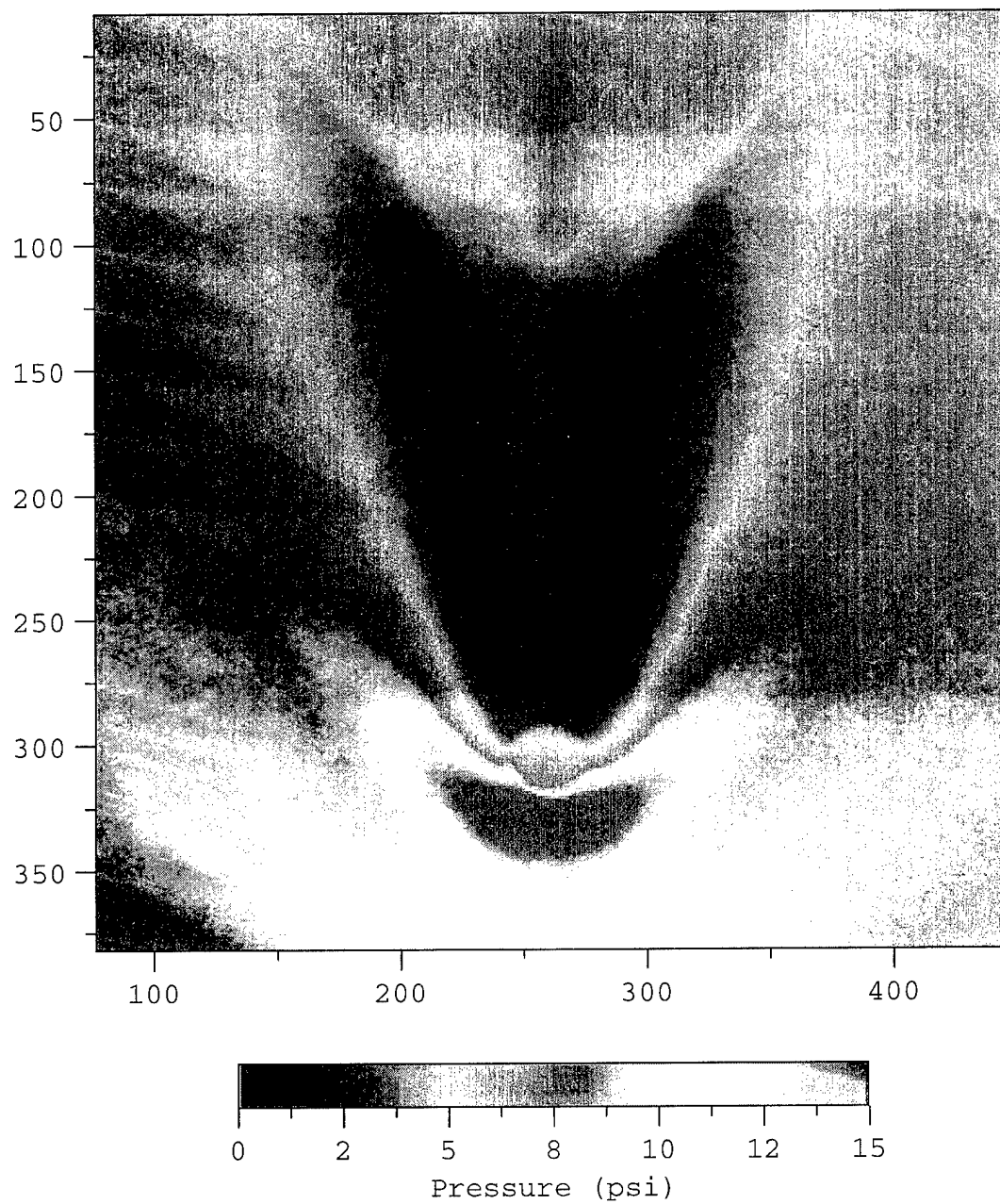at Injection Pressure of 71.3 psi.
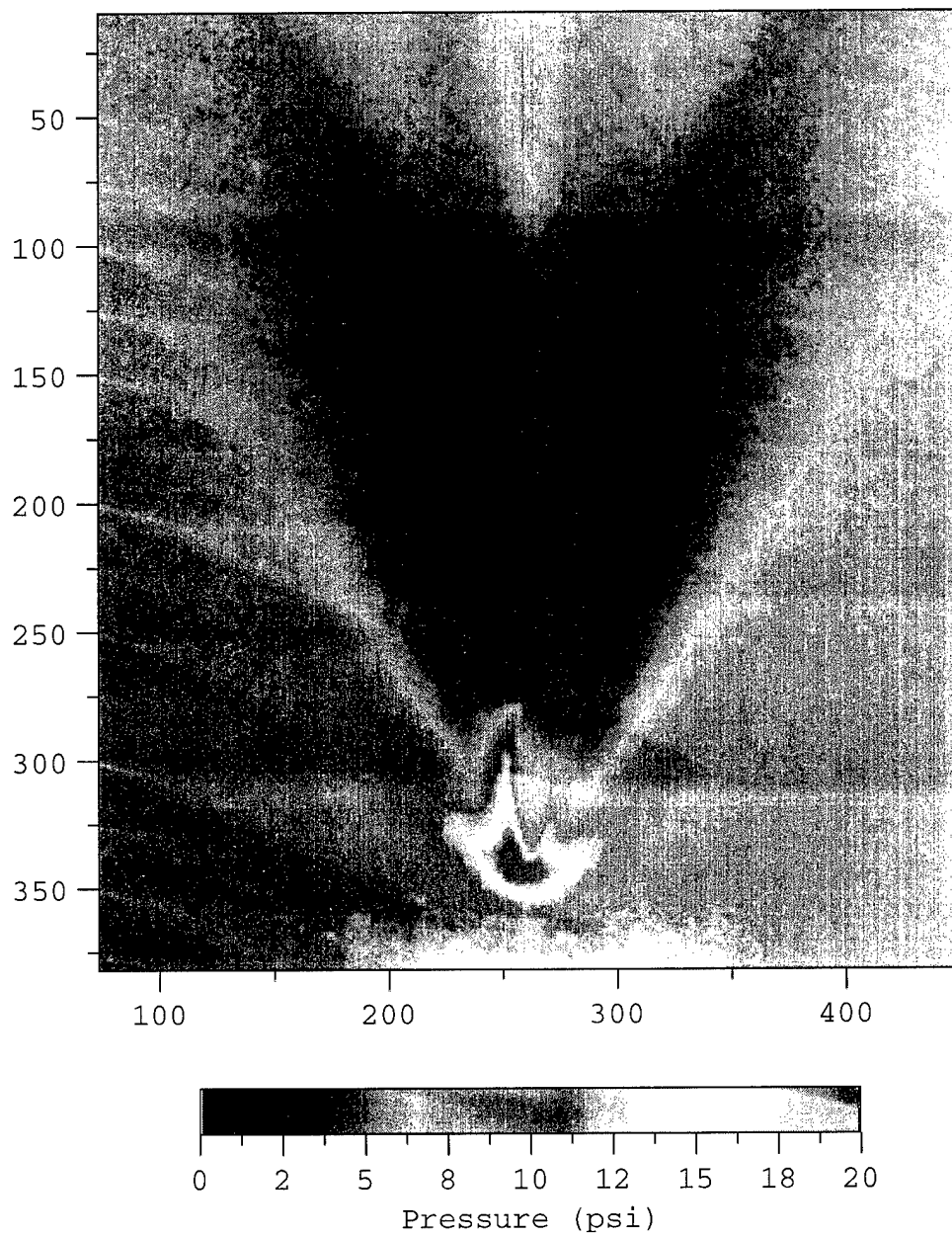
Figure 11(d). Pressure Field Surrounding Elliptical
Injector at Injection Pressure of 95.2 psi.

Nine-Hole Injector. The nine-hole injector was designed to simulate the effects of a ramp injector while minimizing shock losses. As can be seen in Figs. 12(a)-12(c), the injector, in general, meets these design goals. The injector displays a wide coverage at high injection pressures while exhibiting only weak shocks. The interaction between the individual elliptical injectors, however, is complex and will require further study. Figure 13 shows an image taken with the tunnel off and under reduced pressure (2.9 psi). The agreement of the PSP-derived pressure and that from the pressure transducer lends confidence to the calibration procedure and the quantitative nature of the PSP results.

Design of Lifetime-Based Instrumentation

Based on the successful demonstrations of the Phase I program, a lifetime-based pressure, temperature, and heat-flux instrument was designed and preliminary measurements made for supersonic wind-tunnel applications. The principal elements are shown in Fig. 14. The laser system to be employed in this instrument is a pulsed N_2 gas laser with energies in excess of 1 mJ and a pulse width of ~ 500 ps. The short duration of the laser pulse is crucial to the lifetime approach for pressure and temperature measurements. The laser-induced emission from the pressure or temperature paint will be collected by two gatable intensified CCD cameras having 16-bit digital resolution. The gates of the intensified cameras will be positioned temporally in such a way that the fluorescence decay of the pressure or temperature paint can be captured during a single laser excitation (see Fig. 15). The first camera will monitor the initial decay of the fluorescence with an integration time of ~ 50 ns. This camera will take into account the shot-to-shot variation of the fluorescence with laser excitation and paint degradation which may occur. The second camera will capture the fluorescence decay over a period of ~ 300 ns and will be more sensitive to changes in fluorescence lifetime caused by temperature or pressure variations. The ratio of the images from the two cameras allows a two-dimensional fluorescence lifetime to be determined from which the instantaneous pressure or temperature field can be obtained.
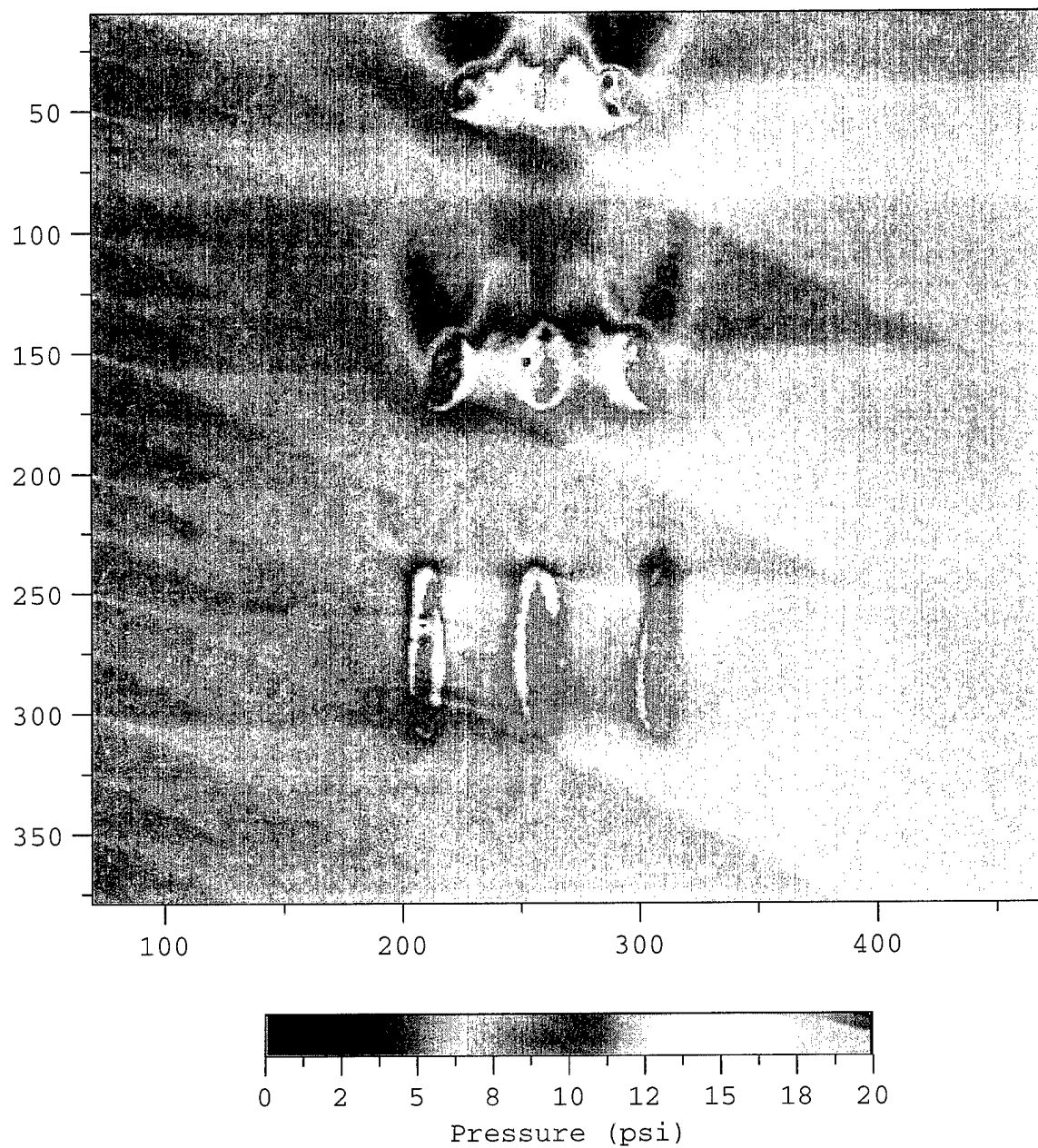
Figure 12(a). Pressure Field Surrounding Nine-Hole Injector at Low Injection Pressure.
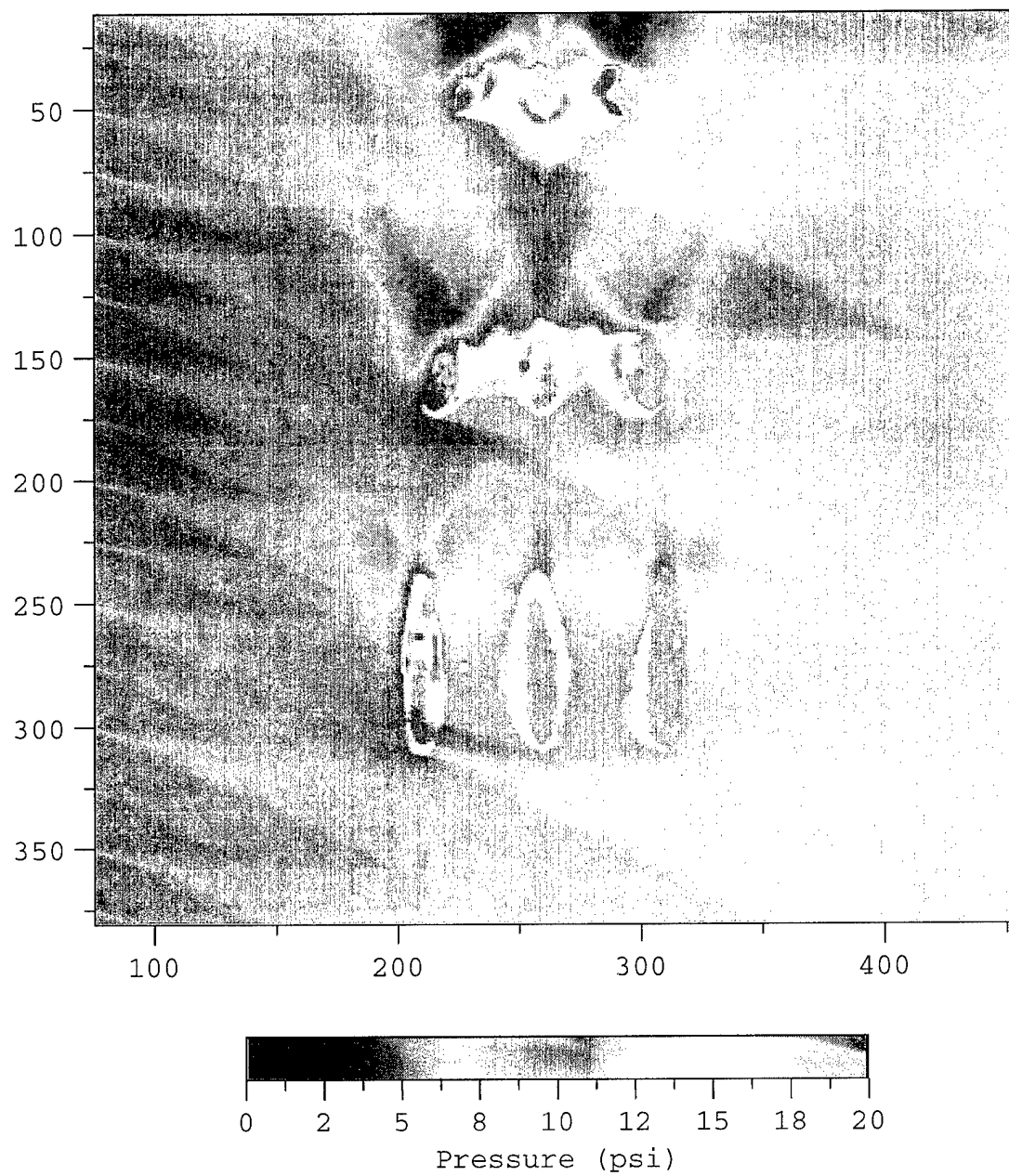
Figure 12(b). Pressure Field Surrounding Nine-Hole Injector
at Medium Injection Pressure.
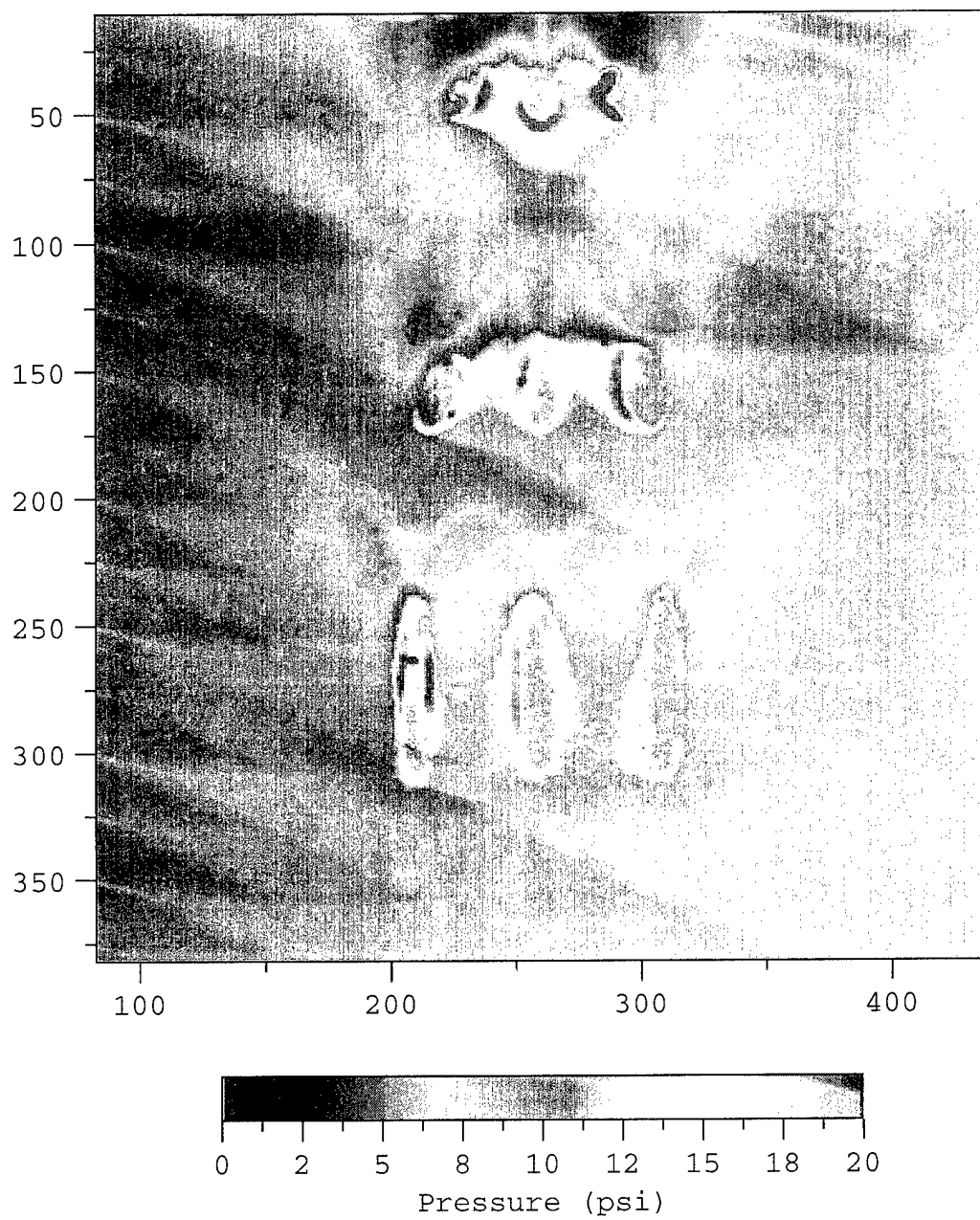
Figure 12(c). Pressure Field Surrounding Nine-Hole Injector
at High Injection Pressure.
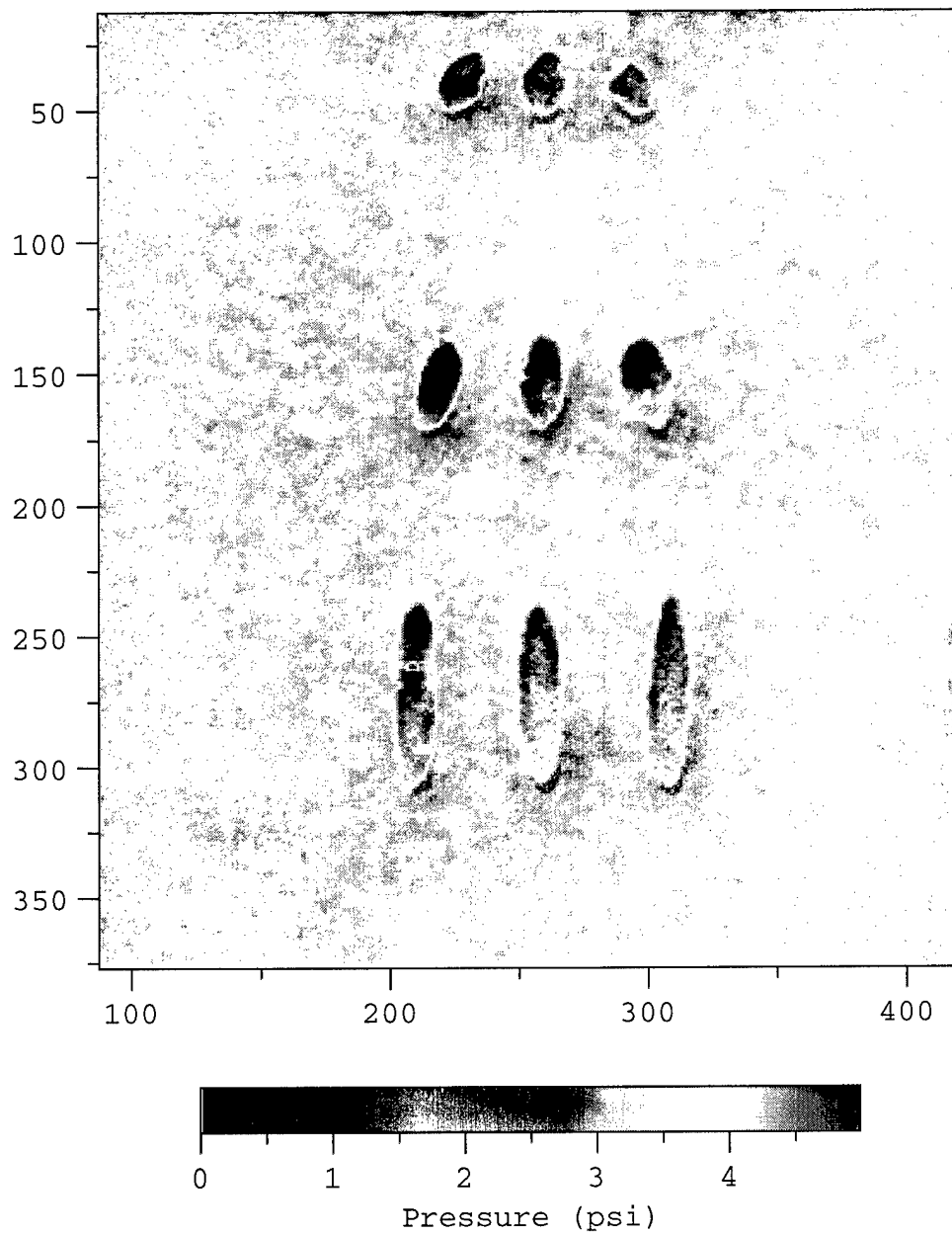
Figure 13. Pressure Field of Nine-Hole Injector with
Tunnel at 2.9 psi.
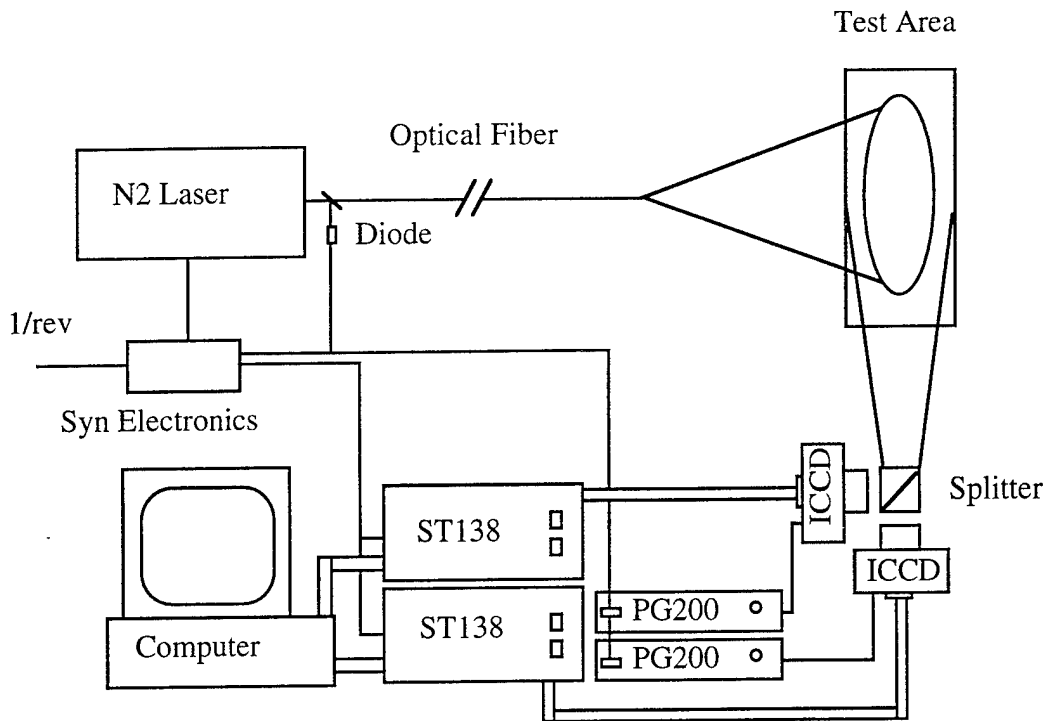
Figure 14. Schematic of Lifetime-Based Pressure, Temperature, and Heat-Flux Instrument.

Figure 15(a) displays the fluorescence lifetime of a pressure-sensitive paint as a function of pressure. As the pressure increases, the oxygen quenching of the fluorescent probe molecule increases, resulting in reduced paint fluorescence and lifetime. Since the paint lifetime is very sensitive to pressure, it can be used as a quantitative measurement. Integrating under the fluorescence decay curves shown in Fig. 15(a) with various gate widths results in the pressure functions shown in Fig. 15(b).

The laser-induced fluorescence from a painted surface will be collected and split into two paths leading to the two ICCD cameras. Each camera will record the fluorescence image at different times. Ratioing the recorded images will result in an image which is uniquely dependent on pressure or temperature. The instrument will be capable of single- or multiple-shot operation, with the maximum operation rate being limited by the digitization speed of the two cameras. The cameras will be controlled by a Pentium computer which will communicate with the camera controllers through a PCI card and with the camera pulsers through RS232 interfaces. Synchronization of the camera electronics with experimental events will be accomplished with ISSI custom-built hardware and software.
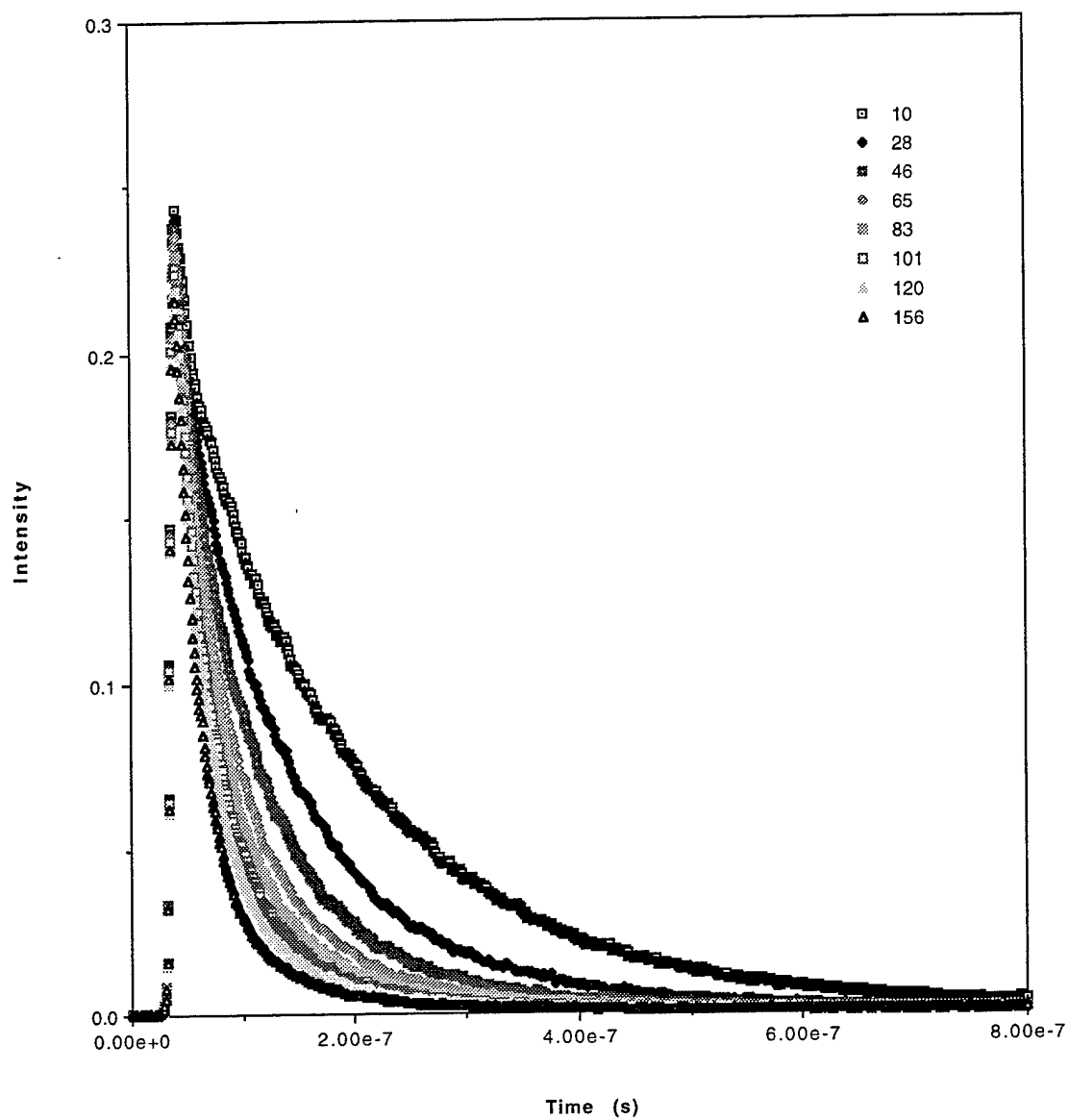
Figure 15(a). Variation of Fluorescence Lifetime with Pressure Over the Range
10 - 156 kPa.
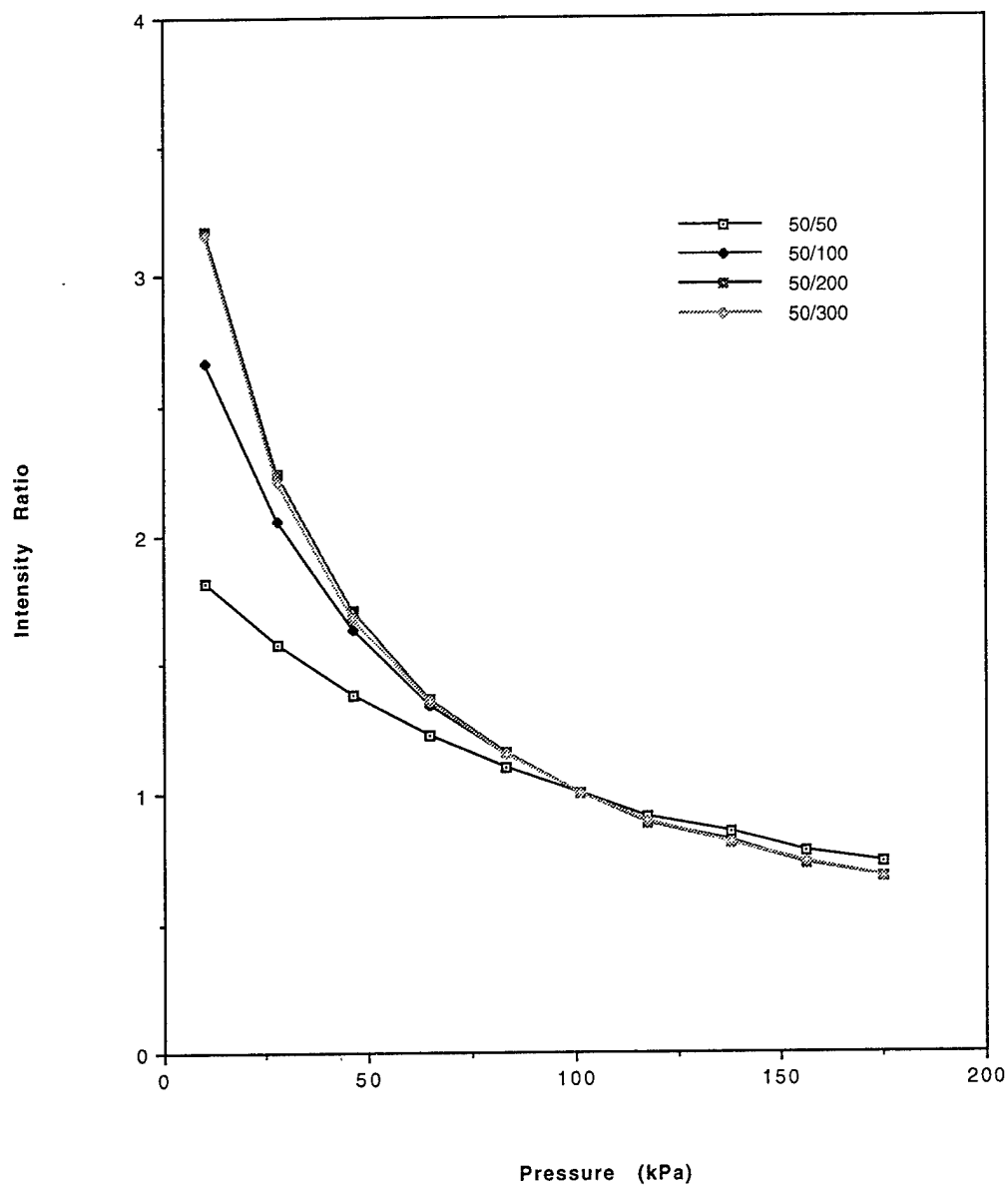
Figure 15(b). Ratio of Integrated Lifetimes for Various Camera Gate Widths in the Range 50 - 300 ns.

Because of the single-shot jitter of the N_2 laser and the inherent temporal delays of the electronics, a fiber-optic delivery system will be used both to delay the excitation pulse and to direct the laser excitation onto the painted surface. A 30-ft length of quartz fiber will delay the laser pulse ~ 40 ns and allow the ICCD gate pulser and the laser firing to be synchronized directly. The timing diagram for the synchronization electronics is shown in Fig. 16. The laser is fired on an external-event trigger. The laser light pulse is split between a delay line (optical fiber) and a pin diode. The output of the pin diode is used to trigger the first camera gate (50 ns) and, subsequently, the second (300 ns).

Development of Optical Heat-Flux Sensor

The research effort during this program was also focused on the design and fabrication of an optical heat-flux sensor based on a thermographic phosphor. The sensor is based on the concept of a three-layer structure, with phosphor coated on both sides of a UV-transparent layer. A potential approach was to use a commercially available PMT sheet and apply different phosphors coated on both sides of the PMT sheet. Because PMT sheets melt around 400°C, such a design may be unsuitable for high-temperature combustion applications. The design of choice would employ quartz glass or a similar material as the substrate, with a hardened-glass resin binder for the phosphor coating. A quartz substrate provides sufficient UV transmittance for phosphor excitation. The particular binder being tested is an organic compound produced by Owens Illinois. With the proper curing process, the binder transforms into quartz that can sustain temperatures up to 1200°C.
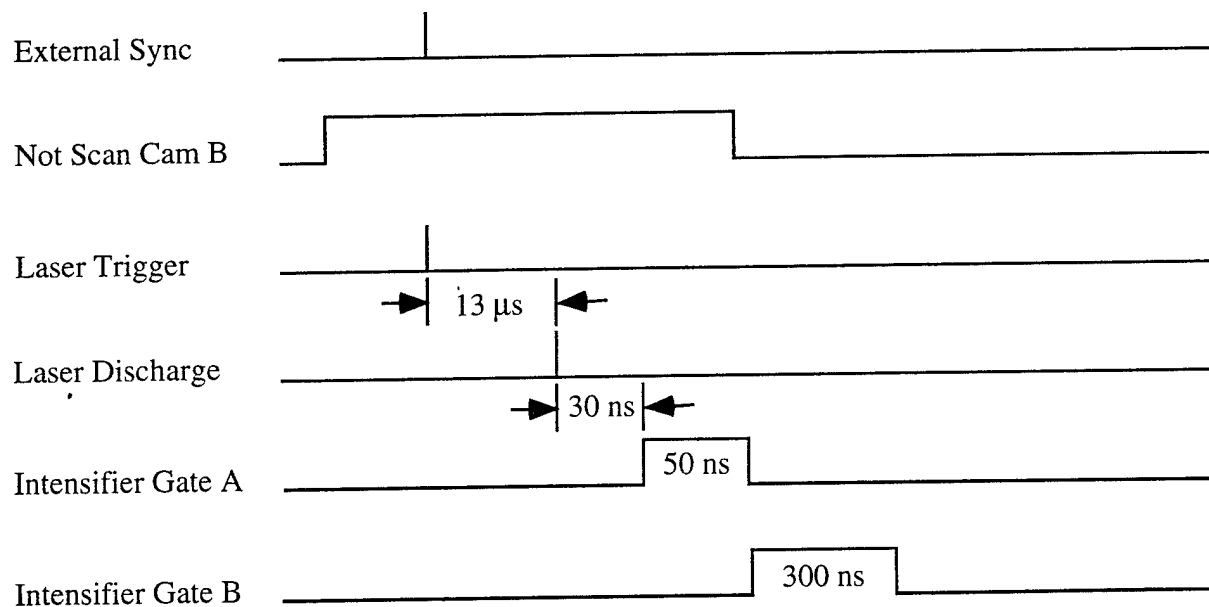
Figure 16. Timing Diagram of Synchronization Electronics for Optical Instrument.

33

Application of phosphor coating on a substrate was achieved by spraying phosphor particles mixed with resin binder. Instead of using two different phosphors on each side of the substrate, the present design permits use of the same phosphor but different coating patterns. The established fluorescence-imaging system is capable of discerning these patterns and resolving the temperature distributions on both sides of the substrate. The heat flux can thus be inferred by applying Fourier's law. Producing an effective heat-flux gauge requires great manufacturing precision in laying out the desirable patterns on a glass substrate. Two approaches were explored during this program, and both techniques were found to be quite promising.

The first approach is to prepare a glass photomask using photolithography techniques currently in use at Carnegie Mellon University. The pattern is made on rubylith paper and the remaining parts cut at forty times the desired size. After this step, the pattern is photographed onto a 2.5-in.-square piece of Kodak glass film. The glass film is developed using standard dark-room procedures. The next step in the fabrication process involves surface micromachining. A positive organic photoresist layer (AZ4210) of 0.7-mm thickness is spin-coated onto the glass substrate. Then the photomask and glass substrate are placed in a mask aligner and exposed to ultraviolet light, which causes the regions of the photoresist layer unprotected by the mask to degrade; the regions protected by the opaque portions of the mask are unaffected. Hydrofluoric acid is used to etch away the now-exposed portions of the glass substrate for ~ 80 min. Since the etching rate of hydrofluoric acid on glass is ~ 100 nm/min., this process etches the pattern on the glass substrate to a depth of ~ 8 μm. The remaining photoresist is eliminated by immersing the glass substrate in acetone. The second side of the substrate is processed in the same manner, but the pattern is offset by one-half a cell width in both the horizontal and the vertical directions. Finally, the alcohol solution of phosphor and binder is sprayed on both sides of the substrate; the substrate is baked, and both sides are then flushed. Thus, the phosphor remains in the etched cavity of the pattern.

The second approach is to prepare a patterned substrate by mechanically pressing a pre-patterned "die" onto a nearly softened glass layer. The particular glass used here is Corning 7059 glass substrate which has a thickness of 0.5 mm and ~ 90% transmittance in the range 340 - 2500 nm. The glass shop at Carnegie Mellon University is capable of heating the substrate uniformly, exceeding its softening temperatures (~ 850°C) and producing a patterned cavity on the glass layer with a depth accuracy of 1 μm. Through the use of a spray technique similar to that of photolithography, the phosphor can be deposited in these cavities on both sides of the glass substrate.

A comparison of the two prototype gauges described above has shown that the one developed by coating a phosphor pattern on a Corning 7059 glass substrate yields stronger fluorescence signals.

34

The gauge is manufactured by pressing a pre-patterned "die" onto one of the surfaces of a 0.5-mm-thick, nearly softened glass substrate. The other side of the substrate is processed in the same manner, but the pattern is offset by one-half a cell width in both horizontal and vertical directions. This process produces a number of diamond-shaped cavities on both sides of the substrate. A standard spin-coating process is then used to fill these cavities with thermographic phosphor in preparation for heat-flux measurements. Shown in Fig. 17 is a gauge prototype ~ 0.5 mm thick; the phosphor-filled cavities are ~ 0.1 mm deep. Note that the diamonds on each surface are staggered to allow viewing of the upper and lower surfaces at the same time. Such a feature provides the present fluorescence-imaging system with a guideline for distinguishing the temperature on each side of the substrate.

Evaluation of Optical Heat-Flux Sensor in Backward-Facing-Step Apparatus

As part of the development effort to evaluate the performance of the gauge, the gauge was used to measure convective heat transfer over a backward-facing step--one of the most fundamental problems involving flow separation and reattachment. This gauge also has a wide range of engineering applications, particularly for combustors and heat exchangers. In addition, flow and heat-transfer characteristics downstream of a backward-facing step have become benchmarks for calibration standards and CFD-code validation.

Fabrication of the test section that houses a backward-facing step was completed. As shown in Fig. 18, the test channel is a square duct, 33 mm on a side, made of 12.7-mm-thick Plexiglas. A circular heat-flux sensor, 25.4 mm in diameter, is mounted flush with the floor of the test channel. For covering the entire measurement domain of interest, the sensor is moved progressively downstream to approximately ten times the step height. The backward-facing step has a height of
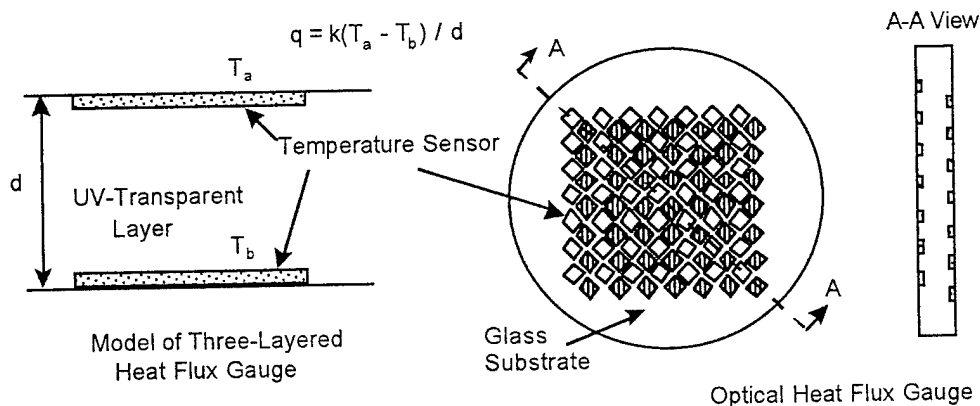
Figure 17. Schematic Diagram of Prototype of Optical Heat-Flux Gauge.
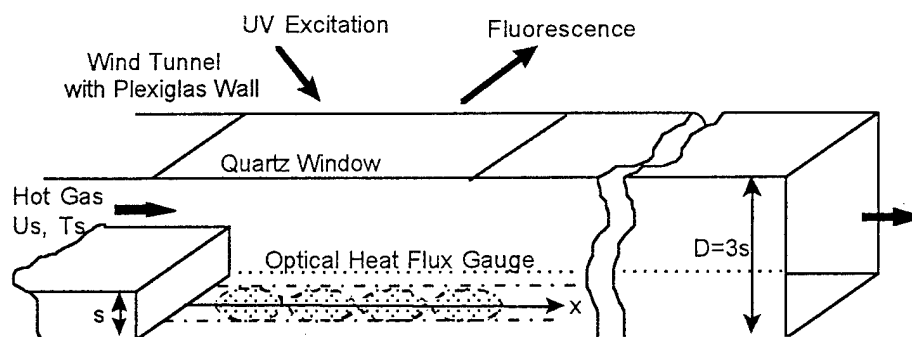
Figure 18. Schematic Diagram of Backward-Facing-Step Test Apparatus.

11 mm, which leads to a step-to-duct ratio s/D = 1/3. Compressed air is routed through a flow regulator and a tubular heater, where the flow is heated to 70°C before entering the test section. Downstream of the test section, the flow eventually discharges to the ambient. The turbulence intensity measured at one step-height upstream to the separation edge and directly above the edge is ~ 1% and 3%, respectively.

In an actual test the heated flow is directed into the test channel. A PC-based data-acquisition system is initiated simultaneously to record the temperature history of the heated flow. For improving the signal-to-noise ratio, each image frame represents the integrated fluorescent signal accumulation over 11 laser pulses--or 1 s--with the signal-integration period following each pulse being 40 μs. After the the raw fluorescence image data has been acquired, an image-processing program to compute the temperatures on both sides of the sensor is executed in the PC. Because of the offset coating pattern, the local heat flux is evaluated using the temperature signified by a diamond-shaped phosphor in conjunction with the average temperature of the four surrounding diamonds of phosphor on the other side of the sensor. With the values of sensor thickness and thermal conductivity being known, the magnitude of the local heat flux is determined using the one-dimensional conduction model and Fourier's Law. Furthermore, the local heat-transfer coefficient can be calculated directly since the local surface temperature has already been measured by the heat-flux sensor.

As discussed above, a prototype optical sensor which is fabricated by the glass-pressure technique was tested for its overall performance in a convective heat-transfer model with separated flow over a backward-facing step. The backward-facing step was chosen for two reasons. First, it is one of the most fundamental problems involving flow separation and reattachment. Second, it also has a viable application as a flame holder in a combustion system. The geometry of the test section and the fabrication procedure were described previously. The test section has a square cross section

36

with 33 mm on a side. A circular heat-flux sensor, 25.4 mm in diameter, is mounted flush with the floor of the test channel. To cover the entire measurement domain behind the step, the sensor is moved progressively downstream to a location approximately ten times the step height. The step-to-duct size ratio is ~ 1/3.

Figure 19 shows the streamwise distribution of the dimensionless local heat-transfer coefficient Nusselt number (Nu), normalized by its flat-plate counterpart (Nu_o) along the centerline of the test channel behind a backward-facing step. The actual value of Nu_0 is evaluated from an empirical correlation for fully developed flow in a flat duct. The figure shows that heat transfer is at a minimum near the corner of the step, where the value of Nu/Nu_0 is ~ 1. Because of strong recirculation behind the step, the flow in the region immediately adjacent to the step is relatively stagnant. The value of Nu then increases progressively in the downstream direction as the recirculation region becomes thinner. Due mainly to shear-layer reattachment, the heat transfer eventually reaches a local maximum (Nu/Nu_0 ~ 3/4) around six step-heights downstream of the step. The value of the heat-transfer coefficient then decreases as the boundary layer grows thicker in the downstream direction. Also included in the figure for comparison purposes is the benchmark data of the backward-facing step acquired by Seban in 1964. The data were obtained by performing detailed--while somewhat tedious--thermal measurements using discrete thermocouples. With advanced fluorescence imaging, the corresponding data obtained with the present optical heat-flux sensor show excellent agreement with the benchmark data. The estimated uncertainties of the present Nusselt number, based on single-sample error analysis, are less than ± 4%.
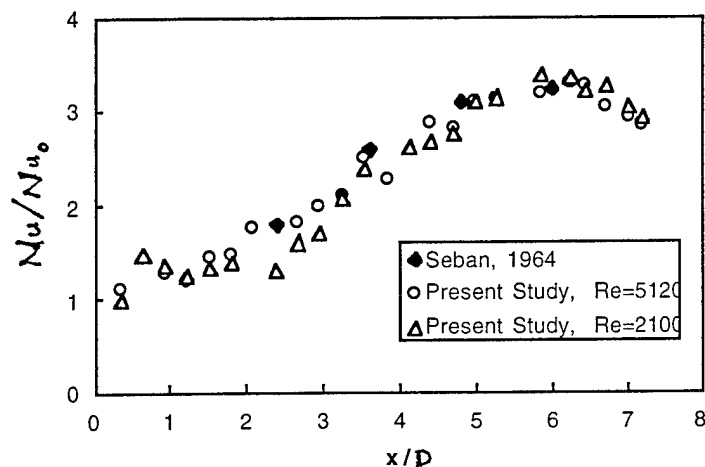
Figure 19. Nu/Nu_0 Distribution at a Backward-Facing Step.

Section 3

POTENTIAL APPLICATIONS

The proposed Phase II program will directly benefit the Federal Government. Specifically, the Air Force Wright Laboratory will receive a state-of-the-art diagnostic system and paints which have been especially designed and tested for application in their major test facilities. More generally, the technology that has been advanced in the prototype-development program will be widely applicable to government-operated test facilities throughout the Department of Defense and NASA Laboratories. Since the research and development on advanced aircraft in the aerospace industry is directly supported by the government, the proposed program will also benefit the Federal Government by increasing the productivity of industrial test facilities and, thereby, reducing development costs.

The proposed pressure, temperature, and heat-flux instrument and paint formulations are expected to have a significant impact on the aerospace testing and evaluation community by providing the first practical demonstrated application to realistic test tunnel environments. ISSI plans to use the engineering data gathered during the prototype testing and demonstrations at Wright Laboratory to enhance its marketing position in the aerospace, automotive, industrial-processing, and architectural industries. Throughout the Phase II program, this application-oriented approach will be maintained. Commercial sales will be pursued by providing complete diagnostic support to commercial customers, including on-site support of existing diagnostic capability, design and delivery of custom instrumentation and paints, and continued in-house development of new diagnostic capabilities.

APPENDIX

Publications and Presentations

AIAA-96-2799

DIGITAL TWO-COLOR PIV MEASUREMENTS IN A MACH-2.8 BOUNDARY LAYER

D. D. Glawe
Aero Propulsion and Power Directorate
Wright-Patterson AFB, OH

R. D. W. Bowersox
Air Force Institute of Technology
Wright-Patterson AFB, OH

L. P. Goss
Innovative Scientific Solutions, Inc.
Beavercreek, OH

W. F. Terry and S. Dasgupta
Taitech, Inc.
Dayton, OH

S. P. Gogineni
Systems Research Laboratories
Dayton, OH

32nd AIAA/ASME/SAE/ASEE
Joint Propulsion Conference
July 1-3, 1996 / Lake Buena Vista, FL

DIGITAL TWO-COLOR PIV MEASUREMENTS IN A MACH-2.8 BOUNDARY LAYER

D. D. Glawe*
Aero Propulsion and Power Directorate
Wright-Patterson AFB, OH 45433

R. D. W. Bowersox[§]
Air Force Institute of Technology
Wright-Patterson AFB, OH 45433

L. P. Goss[†]
Innovative Scientific Solutions, Inc.
3845 Woodhurst Ct.
Beavercreek, OH 45430

W. F. Terry and S. Dasgupta[¶]
Taitech, Inc.
3675 Harmeling Dr.
Dayton, OH 45440

S. P. Gogineni[‡]
Systems Research Laboratories
2800 Indian Ripple Rd.
Dayton, OH 45440

Abstract

A digital two-color particle-image velocimetry (DC2PIV) system is used to make instantaneous planar-velocity measurements in a Mach-2.8 boundary layer. Results from DC2PIV measurements of mean streamwise velocity are in agreement with LDV data. As compared with the LDV data, the larger fluctuation in the measured-velocity values can likely be attributed to a relatively small sample and a relatively large interrogation volume, both of which can be resolved in future experiments.

Introduction

In the area of aerodynamics, the velocity field is arguably the most important physical parameter. For incompressible flows a number of established techniques can be used for accurate and direct measurement of velocity; e.g., pitot-static pressure probes, hot-wire anemometry, laser Doppler velocimetry (LDV), and particle-image velocimetry (PIV). On the other hand, in supersonic flows inherent compressibility effects make the direct measurement of velocity somewhat more difficult. For example, the pitot-static probe is ineffective in supersonic flow because of the inherent wave structure created by the probe and the additional requirement for temperature or density measurements. Likewise, the hot-wire probe becomes sensitive to the local mass-flux and total temperature. Hence, data-acquisition and -reduction procedures are subsequently more complicated, and velocity cannot be measured

directly. However, non-intrusive techniques such as LDV and PIV do provide direct measurement of the velocity in supersonic compressible flows. LDV has been used extensively in high-speed flows and is considered to be the scientific standard. However, PIV has the added obvious benefit of providing an instantaneous measurement of the entire velocity field along a given plane, which is especially useful in unsteady flows. Thus, PIV has been the focus of recent development efforts for turbulent and high-speed flows.[1,2]

The PIV technique allows measurement of the complete velocity field in a plane of the flow in a nanosecond time frame. This not only provides otherwise unobtainable instantaneous information about unsteady flow fields, but also saves operational time in the wind tunnel. For accurate PIV measurements, optimization of several parameters is required. As with all particle imaging techniques for flow diagnostics, the seed particles must be sufficiently small to track the large velocity gradients in the flow but sufficiently large to scatter ample light for detection.[2] Sub-micron particles are required to track turbulent supersonic flows such as the one addressed in this paper. Equally critical factors

---

* Research Engineer. Member AIAA
† President (ISSI). Member AIAA
‡ Research Engineer. Member AIAA
§ Assistant Professor. Member AIAA
¶ Research Engineer. Member AIAA

in optimization of PIV image analysis are spatial resolution of the recording media, temporal delay between laser pulses, density of seed particles in the measurement volume, interrogation spot size and correlation algorithms.

Until recently, the use of PIV measurements was limited to reasonably well-behaved subsonic and transonic flows. Two recent developments have greatly expanded the realm of application for PIV measurement techniques. The first involves the use of two different-wavelength (color) laser pulses and a color-sensitive recording medium.[3] This resolves the problem of directional ambiguity encountered in double-exposure black-and-white images without the complexities associated with the image shifting techniques. In the second a high-resolution color CCD camera is used.[4] This eliminates the tedious and time-consuming data-reduction process required with color film and significantly increases the image signal-to-noise ratio. Both of these developments are incorporated into the PIV system used in this study. A detailed discussion of PIV theory can be found in publication by Adrian et al.[5]

Experimental Setup

Facility

All tests were performed at the Air Force Institute of Technology at Wright-Patterson Air Force Base. A blow down supersonic wind tunnel (Fig. 1) provided 25 seconds of Mach-2.8 air flow at the test section before losing vacuum. The settling-chamber pressure and temperature were maintained at 2.0 ± 0.03 atm and at 297 ± 2K, respectively, resulting in a Reynolds number per meter value of ~ 18 x 10^6 in the freestream. Previously recorded data reveal a variation in Mach number of ± 0.02 across the test section, confirming a two-dimensional flow.[6] The cross-sectional area of the test section is constant and measures 6.35 x 6.35 cm. A pair of Vicor windows mounted in the top and bottom walls of the wind tunnel provide access for the laser sheet light, and a quartz window mounted in one sidewall provides a view port for the camera. The other sidewall, which acts as a backdrop for the images, is painted black to reduce spurious light scatter. The coordinate system is defined such that x is positive in the streamwise direction, with its origin located at the nozzle throat. The streamwise center of the images is located at ~ x = 73. Since the boundary layer of interest is located on the top wall of the wind tunnel, y is defined normal to the top wall of the test section, with its origin at the surface of the wall. Z is the dimension

spanning the wind tunnel. Previously recorded LDV data show the normalized turbulence properties to remain constant over a 30-cm span including the measurement region and the boundary-layer growth to be undetectable within the field of view.[6]

Two-Color PIV System

The two-color PIV system uses color for temporal marking of the seed particles in the flow field. The green (532-nm) laser output is obtained directly from a frequency-doubled Nd:YAG laser. The red (607 nm) laser output is obtained by passing the output from an Nd:YAG laser through a nitrogen-filled Raman cell. The red and green beams are combined by a dichroic beam splitter and directed through a series of sheet-forming optics to generate a sheet with a thickness of < 1mm at the test section (Fig. 2). Details of the optical setup and proposed future developments are published elsewhere.[7] The lasers are pulsed at 10 Hz with a 10-ns pulse width. The laser-sheet energies are typically 2-3 mJ/pulse from the green and red beams. The temporal delay between the two lasers is controlled by a pulse generator and is set as a function of gas velocity, desired interrogation spot size, and optical magnification (m) which is defined as

$$m = \frac{d_{image}}{d_{object}}, \qquad (1)$$

where d_{image} is the dimension of the projection of an object onto the image plane (the 3060 x 2036 pixel array in this case) and d_{object} is the true physical dimension of the object. In the present experiments, two magnifications and, thus, two different time delays were selected and monitored by a photodiode. For a magnification of 0.69, a 400-ns time delay was selected, while a 100-ns time delay was chosen for a magnification of 1.92.

The Mach 2.8 flow is seeded with fog particles formed from a mixture of polypropylene glycol and water (fog fluid # 8207 by Rosco) and vaporized by a Dantec 2927 UL fog generator. The fog particles are thought to be sub-micron in size, with a nominal diameter of ~ 0.5 μm. This will be verified in the future. The smoke generator is designed to operate at atmospheric pressure. However, by enclosing the generator in a pressurized vessel, smoke can be injected into environments having a pressure equal to or less than the pressure of the vessel. In the present study, smoke was injected into the settling chamber of the wind tunnel through

a perforated injection strut mounted just upstream of the flow conditioners. This injection strut was designed to disperse smoke only in the upper half of the tunnel along the spanwise centerline. This provided sufficient seeding for PIV measurements in the boundary layer on the top wall.

The Mie scattering from the seed particles is recorded on a Kodak DCS 460 CCD array. This CCD sensor has a resolution of 3060 x 2036 pixels, and each pixel is 9-μm square. The CCD camera has a built-in 12-bit analog-to-digital converter for increased dynamic range and a frame rate of 1 frame/sec. It also features a PC-MCIA storage drive that delivers ~ 26 exposures, with each PIV image occupying 18 Mbytes. Only three to four images were obtained during each 25 seconds of tunnel operation because of the time required for the camera to reset after the first two images. A 105-mm micro lens with an f-number of 5.6 is used to record the 0.69-magnification images. A 2x extension ring is added to the lens to achieve the 1.92 magnification. A recent study has proven that the proprietary interpolation software developed by Kodak is effective in maintaining the equal red, green, and blue pixel spatial resolution required for accurate PIV measurements, despite unequal pixel color distribution.[8]

Data Analysis

Once the PIV image has been captured and digitized, the velocity field is obtained using a cross-correlation technique. To improve the analysis of the seeded flowfield, the output of the linear camera was convolved with a logarithm-like function prior to cross-correlation analysis. The two-dimensional cross-correlation technique used in the present study is based on intensity maps of the red and green images of scattered light.[8] Innovative Scientific Solutions, Inc. developed the image-processing software used to analyze the data presented in this paper.

The correlation function is calculated over small segments of the PIV image. Thus, prior to processing the digitized PIV image, it is dissected into small sub-regions called interrogation spots. The dimensions of each interrogation spot depend on the particle seed density, estimated local velocity gradients, particle image size, and desired spatial resolution. The maximum displacement of each particle must be less than half the interrogation spot size. In the present experiments, the interrogation domain measured 128 x 128 pixels, corresponding to 1.66 x 1.66 mm with 0.69 magnification and 0.60 x 0.60 mm with 1.92 magnification in the measured

flow. For enhancing the overall resolution, the interrogation domains are overlapped by one-half the domain size. The peak of the correlation map corresponds to the average velocity displacement within the interrogation spot. An intensity-weighted peak-searching routine is used to determine the exact location of the peak to sub-pixel accuracy. The number of particle pairs that are normally necessary to ensure a desirable signal-to-noise ratio is reduced to four or five pairs when the cross-correlation analysis is employed.

Uncertainty Analysis

The experimental uncertainties are calculated based on knowledge of the instrumentation used and a simple root-mean-square error analysis.[9] This method assumes that the contributions to uncertainties arise mainly from unbiased and random sources. Uncertainty in the velocity measurement arises from the time required to keep the large out-of-plane velocity and fluctuating components within the laser sheet during both pulses. The resulting number of pixels of displacement, typically > 10, and the sub-pixel resolution of 0.1 pixels then dictate the uncertainty of < 1%. The data are acquired at resolutions of 1.66 and 0.6 mm, using 77 and 213 pixels/mm, respectively.

Results and Discussion

The Mach-2.8 boundary-layer flow was seeded with presumably sub-micron fog particles generated from a propylene glycol and water mixture. Twenty-nine PIV images were recorded with a magnification of 0.69, while five images were acquired with a magnification of 1.92. PIV system properties for the two image groups are displayed in Table 1.

Figures 3a and 3b show typical double-pulsed two-color images for m = 0.69 and 1.92, respectively. The field of view for both images is centered at ~ x = 73 cm. The LDV data presented in this paper were recorded at ~ x = 72cm. Boundary-layer structures are evident in the top portion of Fig. 3a. The streaks in the middle of the m = 0.69 image are due to partial blockage of the holes in the injection strut. The red-green particle pairs are clearly visible in the m = 1.92 image. The typical separation between red and green images in the particle pairs is 13 - 15 pixels in the freestream flow for both magnifications, based on the time delay and pixel resolution. The red beam was pulsed first.

Inspection of the red-green particle pairs in Fig. 3b shows the flow velocity to be from right to left.

Corresponding vector plots are shown in Figs. 4a and 4b. Invalid vectors omitted from the velocity maps account for the blank spots. It is evident that system optimization made it possible to obtain a high percentage of valid vectors. The invalid vectors were due to an insufficient number of particle pairs within the interrogation spots. An increase in the density of seed particles in the flow is proposed for future experiments to alleviate this problem. Several fog generators are commercially available and warrant investigation for use with PIV, and possibly LDV, systems.

A consistent transverse velocity v ~ 20 m/s in the freestream flow indicates that the camera was slightly tilted relative to the top wall of the tunnel. This introduces a negligible error ($< 0.06\%$) in the streamwise velocity values. A large tilt would require corrective calculations for both the frame of reference and the measured velocity values.

A ± 10 ns jitter in the time delay caused the overall velocity measurements to shift a different amount for each image with a maximum deviation of 5%. Normalizing the velocity vectors with the freestream or boundary "edge" velocity for each m = 0.69 image would resolves this deviation.. A similar normalization for the m = 1.92 images would yield similar results. Once the valid velocity vectors have been determined the statistical analysis can be performed.

Mean velocity, turbulence intensity and shear stress values are calculated over the image ensemble for each interrogation spot. Figure 5 shows the normalized mean streamwise velocity values for each interrogation spot as a function of y/δ, where y is the distance from the wall and δ is the boundary-layer thickness determined to be 9.9 mm in an earlier LDV study.[6] The series of PIV data points shown at each y/δ location corresponds to the interrogation spots across the image in the x-direction. Contrary to the LDV data, which show the boundary-layer thickness to vary less than $\pm 0.34\%$ in this region,[6] suggesting axial homogeneity, measurement results in the current study show variation in the streamwise velocity along the axial direction. The mean freestream velocity appears to increase as much as 10 m/s across the 18-mm flow region captured in the PIV image (Fig. 6). This suggests that the boundary layer is not fully developed at the measurement location ~ x = 73 cm downstream of the nozzle throat.

Figure 7 shows the fluctuation of velocity values for each interrogation spot in terms of normalized RMS values. Again, each data point represents the average value through the 29 images, and the series of points at each y/δ corresponds to the series of interrogation spots across the image in the x-direction. A portion of the velocity fluctuation is due to the ± 10 ns jitter in the time delay between laser pulses, as previously discussed. The RMS values for the PIV measurements are equal to the RMS values near the wall and are nearly twice as large as the RMS values for the LDV measurements away from the wall. The number of samples in the sample set used for these calculations greatly influences the RMS values. For PIV, the number of samples remains constant at ~ 29 per interrogation volume, whereas the LDV measurement sample size for each measurement volume varies from ~ 5000 near the wall to ~ 30,000 in the freestream. All other factors being constant, an increase in sample size of this magnitude would cause the RMS values to decrease from the wall to the freestream. The calculated shear stress values are even more sensitive to the number of samples in a sample set. As expected, the shear stress values calculated from the limited sample of PIV measurements are notably scattered (Fig.8). In addition to sample size, interrogation volume influences the resulting velocity distribution. The interrogation spot size, similar to the LDV measurement volume, allows for a finite velocity distribution within the interrogation spot itself which is most significant near the wall where the largest velocity gradients are present. The velocity value at each 1.66 x 1.66 mm interrogation spot is the spatial average for that spot.

Slight deviation in contour shape could be attributed to compressibility-related velocity biasing which can occur in LDV measurements. If the seed is uniform in the stagnation region of the flow, then as the flow compresses, the regions of highly compressed flow will contain more seed particles than the regions of highly expanded flow. Thus, burst-mode-type LDV processors will "see" more seed in the compressed regions of the flow. Thus, the results may be biased toward the velocity of the highly compressed region. Generally, this density-bias error is most significant for flows with large density variations (e.g., combusting flow).

A rather simple solution to this potential-bias problem is uniform LDV sampling of the flow; hence, the time of the sample is decoupled (i.e., uncorrelated) from the flow. However, this generally results in far fewer valid Doppler bursts for a given amount of test time, which for blow-down-type facilities can be a serious limitation.

In theory, PIV is also susceptible to the density-bias error. However, since the PIV technique does not utilize a Doppler burst, accurate velocity measurements are attainable with minimal compressibility effects.

Conclusions

The high spatial resolution and high signal to noise ratio inherent in the D2CPIV system allow effective measurements of two-dimensional flow velocity in supersonic flows. The PIV results are sufficiently promising to warrant further studies in a well documented supersonic flow with more images per sample set, smaller interrogation size, and increased seeding.

References

[1] Yao, C., and Paschal, K., "PIV Measurements of Airfoil Wake-Flow Turbulence Statistics and Turbulent Structures," AIAA Paper 94-0085, January 1994.

[2] Bryanston-Cross, P.J., and Epstein, A., "The Application of Sub-Micron Particle Visualization for PIV (Particle Image Velocimetry) at Transonic and Supersonic Speeds," *Prog. Aerospace Sci.*, Vol. 27, No. 1990, pp. 237-265.

[3] Goss, L.P., Post, M. E., Trump, D. D., and Sarka, B., "Two-Color Particle Imaging Velocimetry," *J. Laser Appl.*, Vol. 3, No. 1991, pp. 36-42.

[4] Gogineni, S., and Trump, D., and Goss, L., "Two-Color PIV Employing a Color CCD Camera," *48th APS/DFD Meeting*, November 19-20, 195. Abstract Pub. in Bull. APS 40(12), 1950(1995), 1995.

[5] Adrian, R.J., "Particle Imaging Techniques for Experimental Fluid Mechanics," *Ann. Rev. Fluid Mech.*, Vol. 23, No. 1991, pp. 261-304.

[6] Bowersox, R.D.W., and Buter, T. A., "Mass-Weighted Turbulence Measurements in a Mach 2.9 Boundary Layer Including Mild Pressure Gradients," AIAA Paper 96-0659, January 1996.

[7] Dasgupta, S., Terry, W. F., Vuppuladhadium, R., Bowersox, R. D. W., Glawe, D.D., Chen, T.H., and Nejad, A.S., "Two-Color Particle Imaging Velocimetry Systems for Supersonic Flow Studies," AIAA-96-2798, July 1996.

[8] Gogineni, S., Trump, D., Goss, L., Rivir, R., Pestian, D., "High-Resolution Digital Two-Color PIV (D2CPIV) and Its Application to High Freestream Turbulent Flows," *Proceedings of the 8th International Symposium on Applications of Laser Techniques to Fluid Mechanics*, Lisbon, Portugal, 1996.

[9] Kline, S.J., and McClintock, F. S., "Describing Uncertainties in Singe Sample Experiments," *Mech. Eng.*, Vol. 75, No. 1953, pp. 3-8.

TABLE 1: PIV system parameters

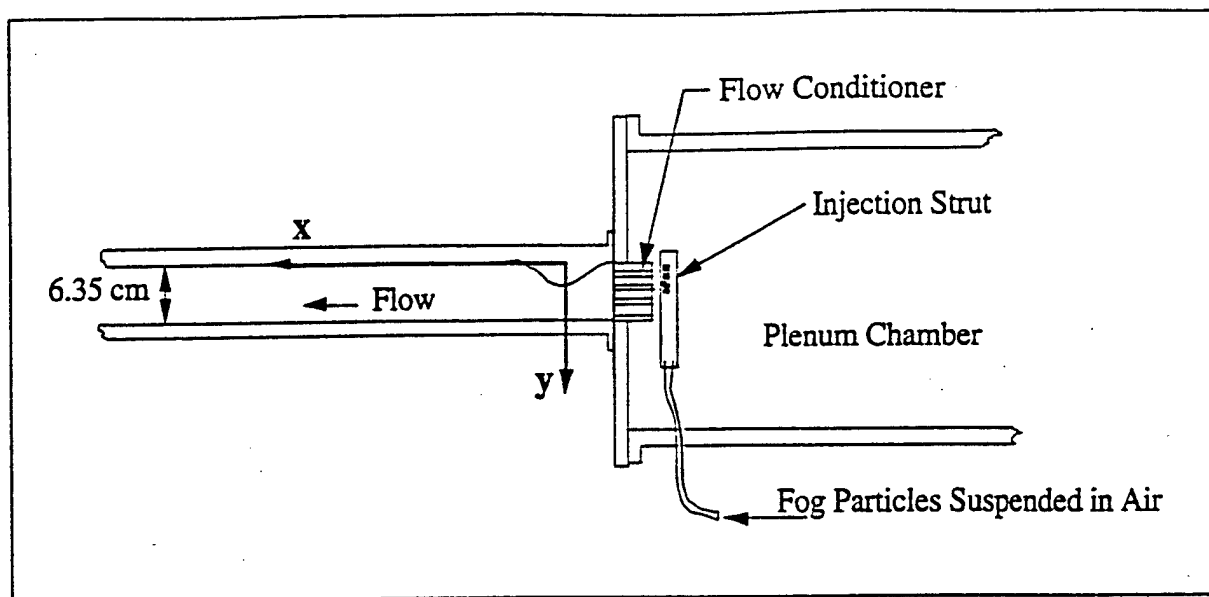| Magnification	Resolution	Time delay	Interrogation spot dimension	
	(pixels/mm)	(ns)	(pixels)	(mm)
0.69	77	400 ±20	128 x 128	1.66 x 1.66
1.92	213	100 ± 20	128 x 128	0.60 x 0.60

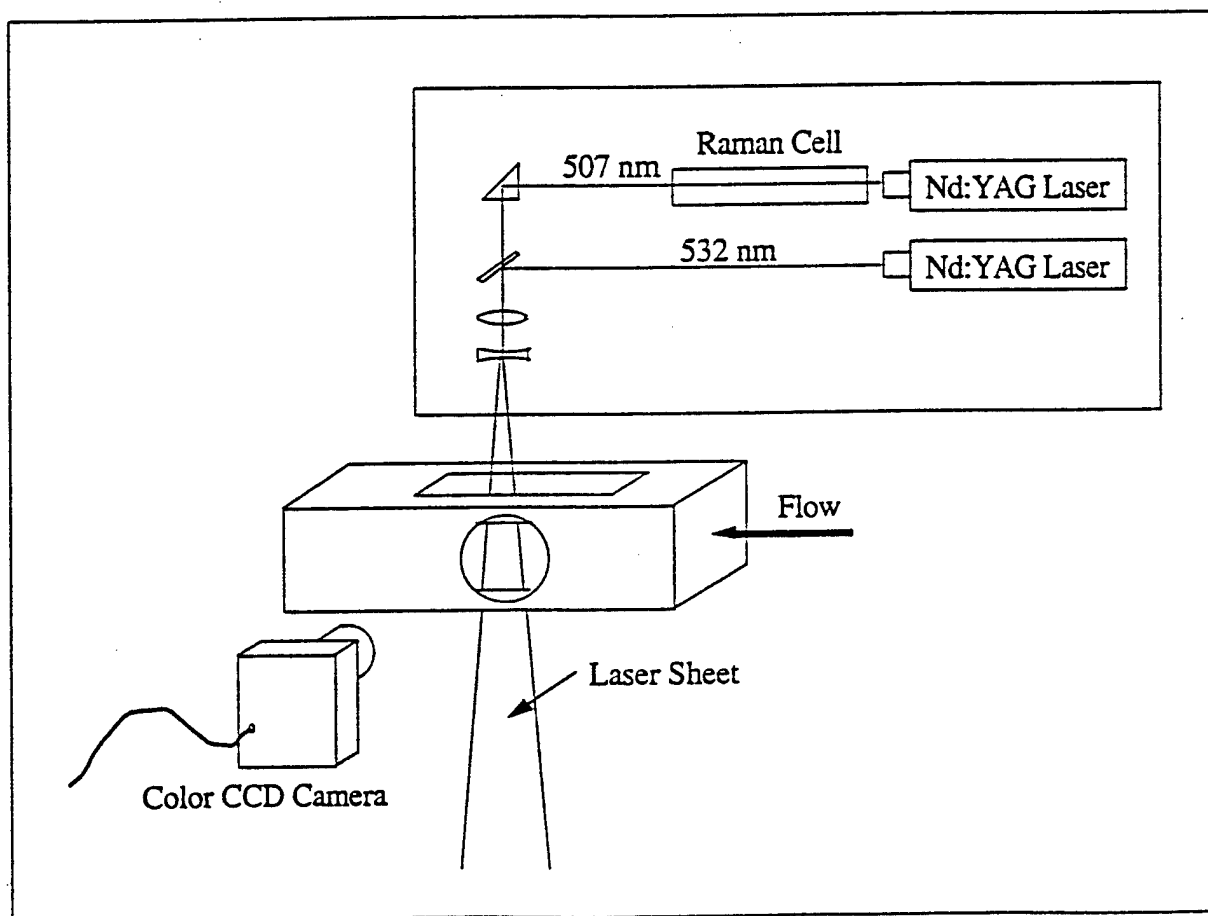Figure 1. Schematic of tunnel cross section

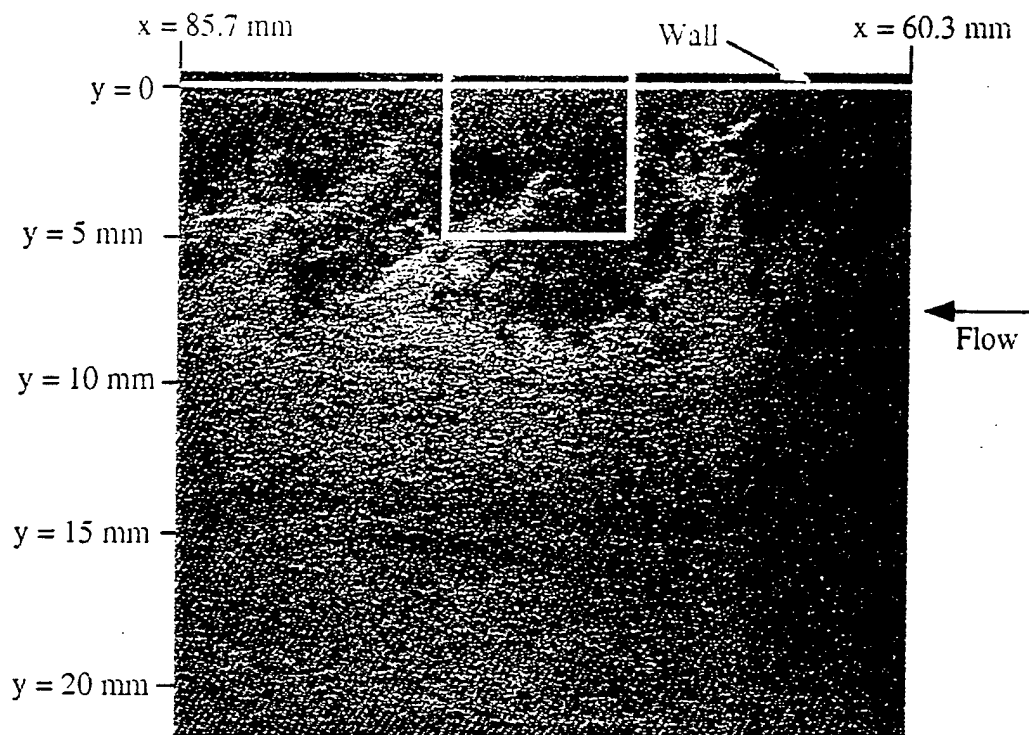
Figure 2. Schematic of PIV optical system

Figure 3(a). Double exposed PIV image with magnification 0.69
[Box represents field of view for Figure 3(b)]
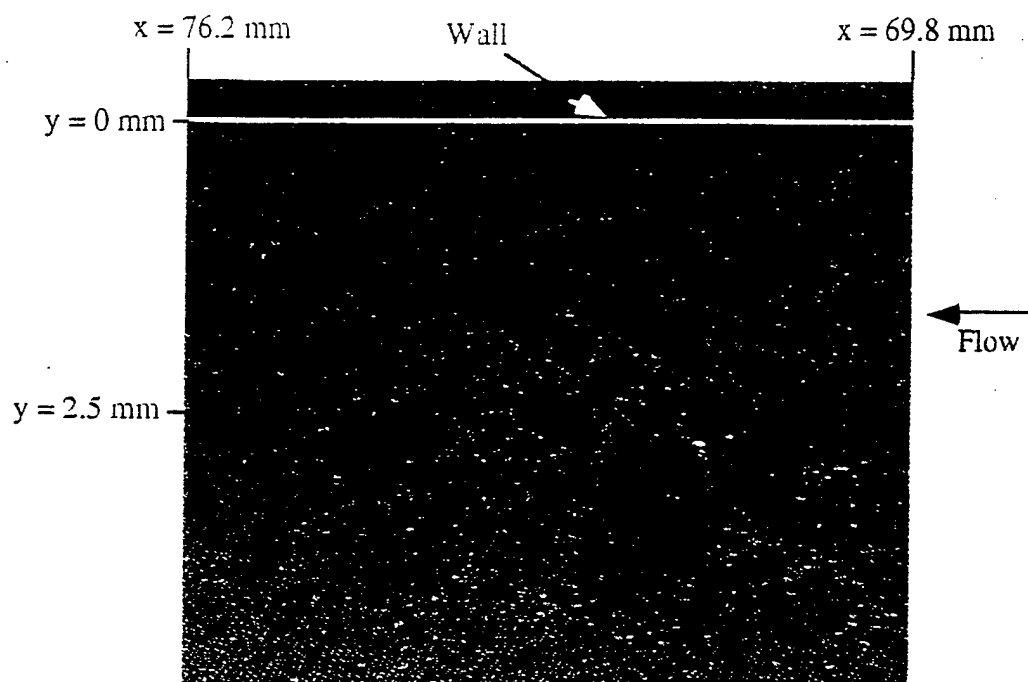
Figure 3(b). Double exposed PIV image with magnification 1.92

x = 85.7 mm   x = 60.3 mm

y = 0 mm

                                                              ← Flow

y = 10 mm

y = 20 mm
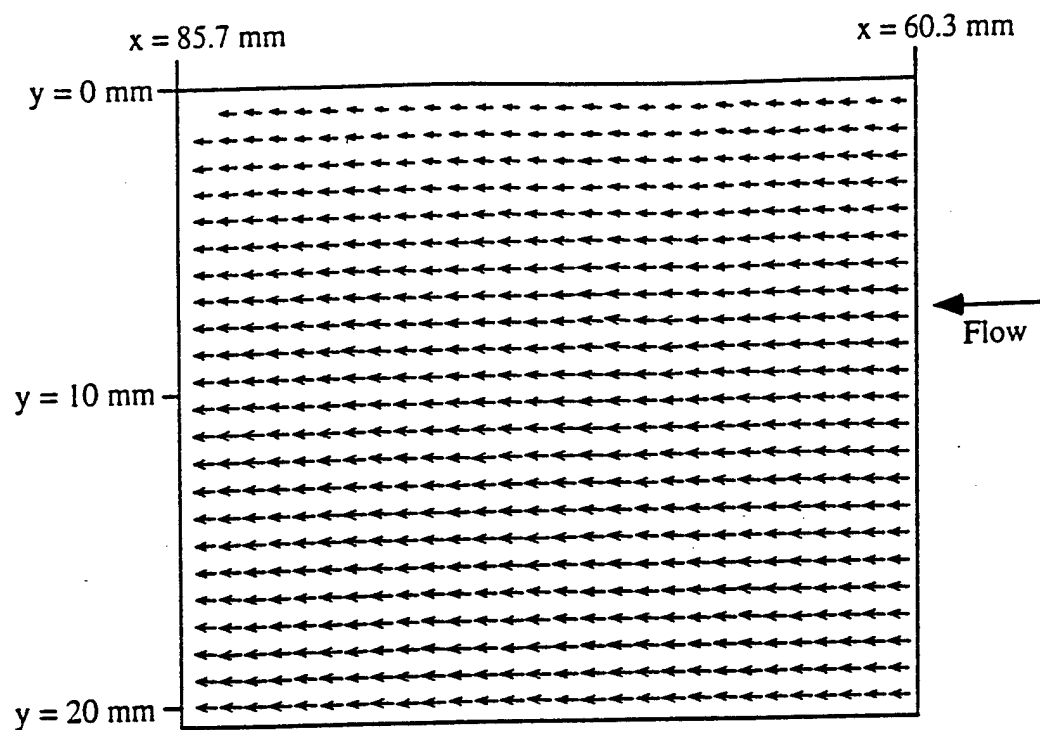
Figure 4(a). Instantaneous velocity distribution corresponding to Figure 3(a)

x = 76.2 mm   x ≅ 69.8 mm

y = 0 mm

                                                              ← Flow

y = 2.5 mm

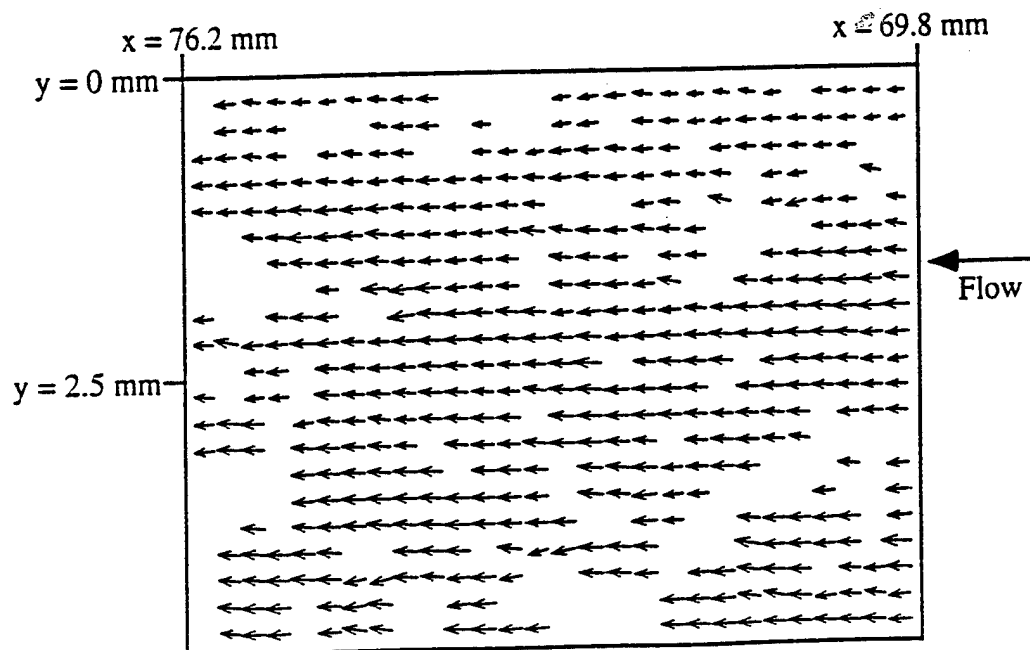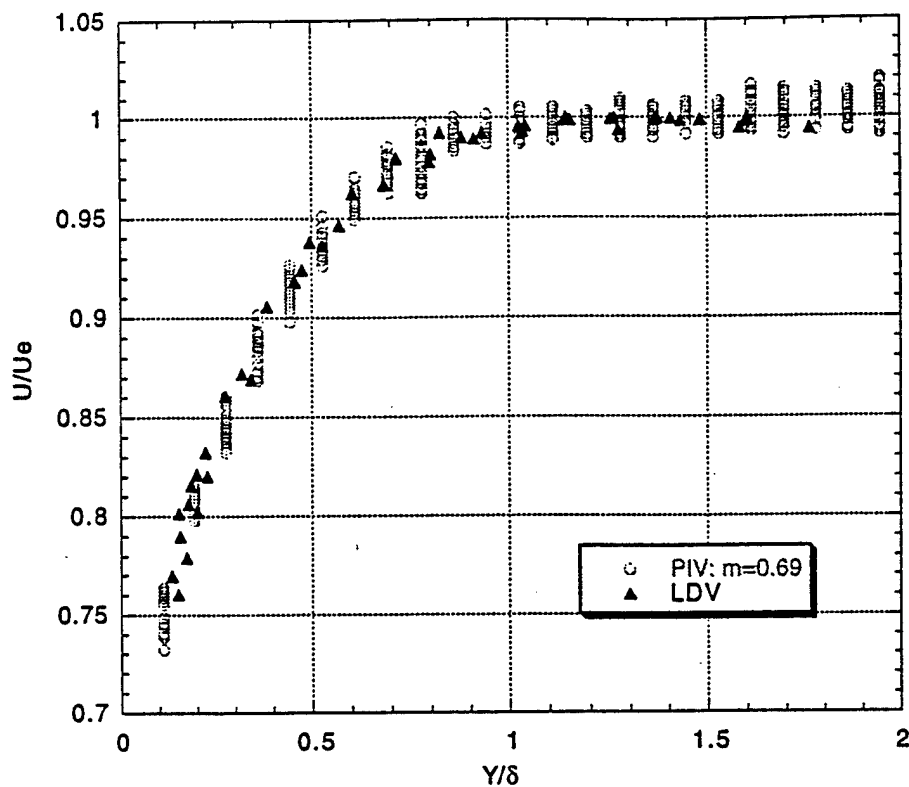Figure 4(b). Instantaneous velocity distribution corresponding to Figure 3(b)
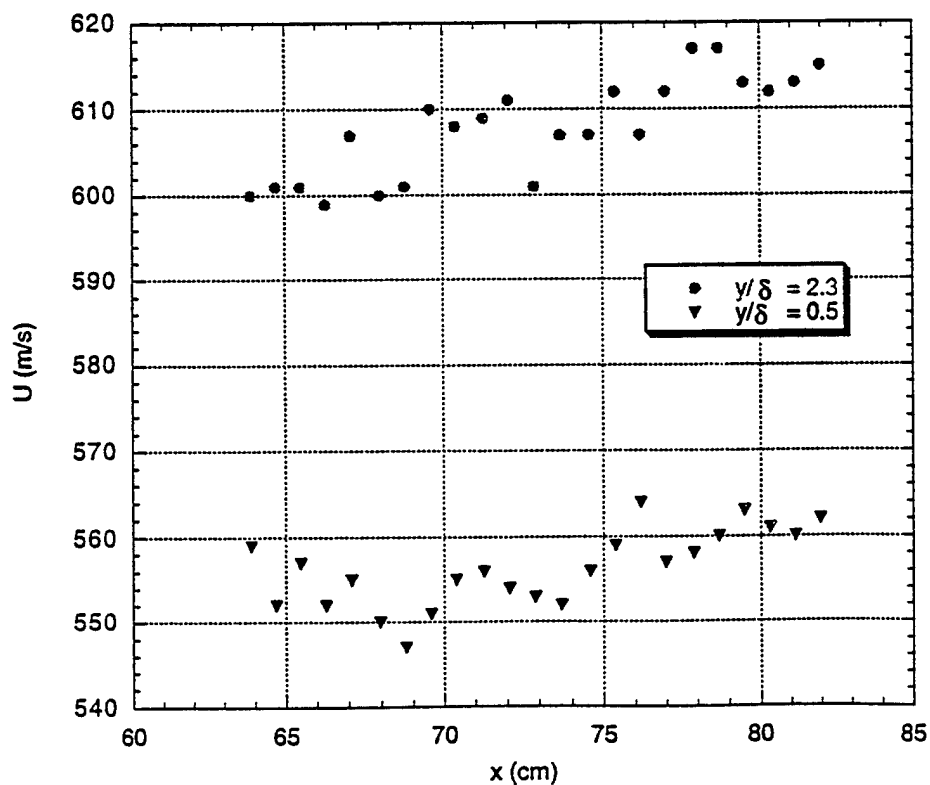
Figure 5. Normalized mean streamwise velocity

Figure 6. Mean streamwise velocity as a function of streamwise location. Two sample profiles: one in the middle of the boundary layer (y/δ = 0.50) and the other in the freestream (y/δ = 2.3)

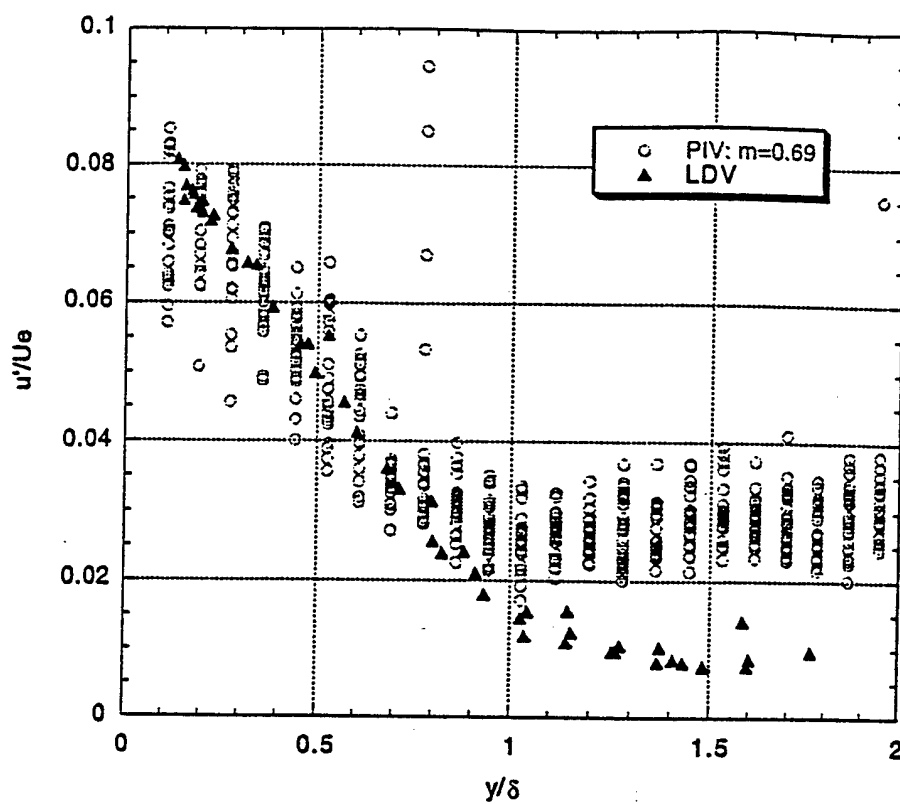Figure 7. Streamwise turbulence intensity
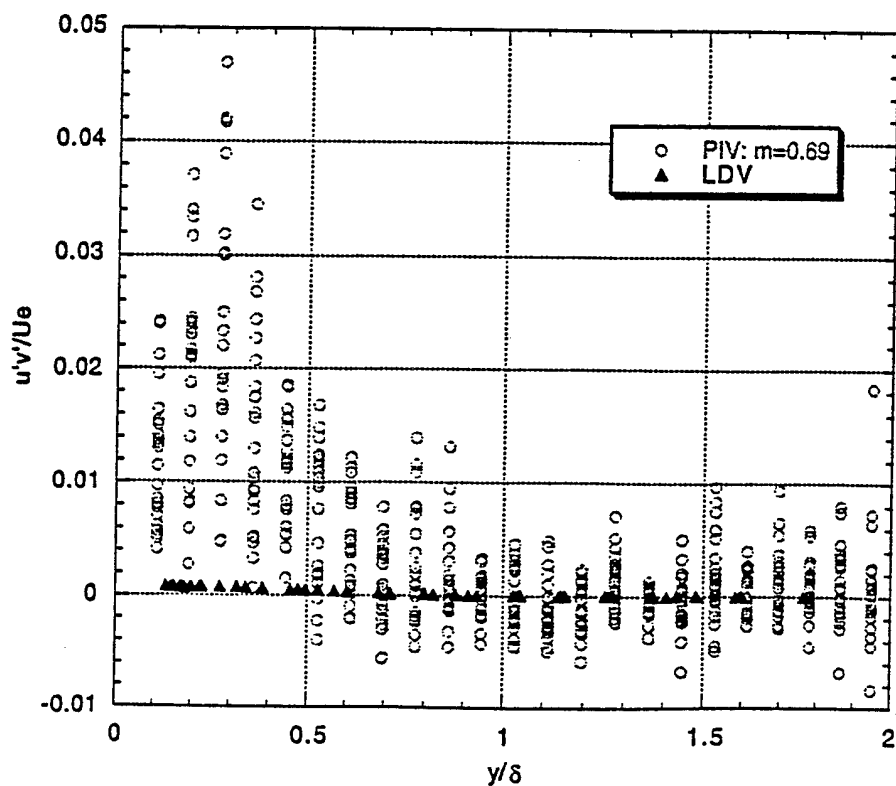
Figure 8. Turbulent shear stress

Development of High-Resolution Digital Two-Color PIV (D2CPIV) for Supersonic Turbulent Flows   D. Glawe (Wright Lab, WPAFB, OH); R. Bowersox (AF Inst. of Technol., WPAFB, OH); S. Gogineni, L. Goss (ISSI, Dayton, OH)

Supersonic turbulent wall boundary layers subjected to a pressure gradient occur in many practical situations. Since these flows are typically intractable from an analytical standpoint, experimental diagnositc techniques are needed. For this purpose a high-resolution (3060 x 2030 pixel) D2CPIV system was developed for making instantaneous velocity measurements. The measurements were made in a Mach-2.9 wind tunnel, and curved walls were used to produce the pressure-gradient and streamline-curvature effects. Several flow-visualization studies were also conducted to explore the qualitative flow features. Results from D2CPIV measurements of mean streamwise velocity and LDV data were compared and found to be in good agreement. The D2CPIV system was calibrated using solid-body translation and rotation data, and the uncertainties and errors were estimated.

Experimental Investigation of Distorted Supersonic Turbulent Boundary Layers   Weir,
R., Bowersox, R. (Air Force Inst. of Tech., WPAFB, OH); D. Glawe (Wright Lab,
WPAFB, OH); S. Gogineni; L. Goss (ISSI, Dayton, OH)
Distorted supersonic turbulent boundary layers occur in practical situations
such as exterior curved surfaces of high-speed flight vehicles and missiles,
supersonic-aircraft engine inlets, and flow within high-performance
compressors and turbofans. These flows are typically intractable from
an analytical standpoint and challenging from both experimental and
numerical perspectives. To understand complex flow features,
experimental investigations were conducted using cross-film anemometry
and laser diagnostic techniques in a Mach-2.9 wind tunnel. It was found
that the magnitude and distribution of turbulent shear stress are strongly
affected by pressure gradients and the favorable pressure gradient
significantly reduces the shear-stress magnitude when compared to
zero-pressure-gradient results. The studies also provided information
on effects of streamline curvature and pressure gradients on large-scale
structures.

Digital Two-Color PIV and Flow-Visualization Studies for Complex Supersonic Flows

S. Gogineni and L. Goss
Innovative Scientific Solutions, Inc.
Beavercreek, OH 45430

D. Glawe
Aero Propulsion and Power Directorate
Wright-Patterson AFB, OH 45430

R. Bowersox and R. Wier
Air Force Institute of Technology
Wright-Patterson AFB, OH 45430

ABSTRACT

Complex supersonic flows such as supersonic turbulent boundary layers subjected to a pressure gradient and supersonic gaseous injection into a supersonic cross flow were investigated using Mie scattering and Digital Two-Color PIV techniques. Instantaneous Mie-scattering visualizations of the jet (M = 1.6) in a cross flow (M = 2.9) provided valuable qualitative information concerning the large-scale turbulent structures. The time-averaged visualizations revealed the penetration and plume-dispersion effects. Flow visualizations of the supersonic turbulent-boundary-layer flows showed that a rather mildly curved wall dramatically alters the overall structure of the boundary-layer flow. For example, the boundary-layer thickness for the adverse-pressure-gradient model decreased by about 50%. Several instantaneous digital PIV images were acquired to obtain the mean-velocity and turbulence-intensity components. A relatively small number of images (25) adequately resolved the mean flow quantities. These results were compared with corresponding LDV data, and good agreement was found. The turbulence-intensity results from PIV samples and the LDV data in the near-wall region of the boundary layer showed good agreement for the zero-pressure-gradient and favorable-pressure-gradient conditions. However, the signal-to-noise ratio of the present PIV setup was insufficient to resolve the low-freestream-turbulence levels. Of the three pressure gradients considered, the PIV results and the LDV data showed the least agreement for the adverse-pressure-gradient condition. This discrepancy is attributed to the decreased signal-to-noise ratio that resulted from the smaller boundary layer.

NOMENCLATURE

ZPG	=	zero pressure gradient
APG	=	adverse pressure gradient
FPG	=	favorable pressure gradient
B	=	pressure-gradient parameter
H	=	δ^*/θ
k	=	turbulent kinetic energy
M	=	Mach number
Re	=	Reynolds number
u, v, w	=	velocity components
β	=	$\delta^*/\tau_w \, dp/dx$
δ	=	boundary-layer thickness
δ^*	=	kinematic displacement thickness
θ	=	kinematic momentum thickness
τ	=	shear stress

Subscript

e	=	boundary-layer edge
t	=	total condition
w	=	wall

Superscript

o	=	Inflow condition
$(\ )'$	=	Reynolds fluctuating component
$\overline{(\ )}$	=	Reynolds mean component

1. INTRODUCTION

A number of new key technologies have allowed the development of advanced laser-based optical flow-diagnostic techniques; the technologies include, but are not limited to, high-resolution digital photography (3060 x 2036 pixels), high-speed computers, mass storage capacity (~ 10 Gbyte), and high-energy (~ 200 mJ) pulsed lasers. The ability to

provide both qualitative and quantitative *global* experimental flow-field information has the potential to be as significant a breakthrough toward the understanding complex-geometry flows as computational fluid dynamics. The focus of the present work is to further develop and evaluate the performance of flow-diagnostic techniques for two complex high-speed (supersonic) flows. First, a two-dimensional, two-color, digital Particle Image Velocimetry (PIV) technique was further developed and evaluated for quantitative planar-velocity and turbulence-intensity data for supersonic flow (M = 2.9) over three wall shapes (flat, convex, and concave). Second, qualitative flow visualizations were obtained for a complex, three-dimensional flow; namely, an angled supersonic jet (M = 1.6) into a supersonic cross flow (M = 2.9). The practical implications and salient flow feature for both of these flow fields are described in Sections 1.2 and 1.3; first, however, a brief review of PIV is in order.

1.1 Particle Image Velocimetry (PIV)

The PIV technique has been used for a number of years to measure velocity distributions in planar cross sections of aerodynamic flowfields (Adrian 1991). In early experimental approaches involving the PIV technique, the particle images were recorded on photographic film. However, this type of recording is time-consuming because of the need to develop the film before digitization and subsequent computer processing. This disadvantage can be overcome by recording the particle images directly onto a two-dimensional CCD array. This approach has been recognized by several investigators, and the appropriate references have been given by Gogineni et al. (1996). The extension of the two-color PIV technique to include CCD cameras has been hampered in the past' by the lack of commercially available high-resolution color CCD camera systems. Because of recent developments in these systems, the difficulty in their use for two-color PIV has significantly decreased. Gogineni et al. (1996) developed a high-resolution digital two-color PIV system and successfully implemented it to simulate turbine-film-cooling flows involving high-freestream-turbulence levels. A similar system was used in the present investigation

1.2 Supersonic Flow with Streamline Curvature

Supersonic flow over curved surfaces has many practical applications, for example, exterior aerodynamic lifting surfaces, supersonic aircraft-engine inlet compression ramps, supersonic turbofans, and supersonic nozzles flows. Because of the large number of practical uses, these flows have been the subject of much investigation [for a comprehensive listing, see Spina et al. (1994) and Luker et al. (1997)]. However, as discussed by Bradshaw (1974) and Spina et al. (1994), the fundamental physical processes are not well understood. Hence, investigations of these flows have important theoretical

implications. The primary reason for the lack of understanding of supersonic flows with pressure-gradient effects has been attributed to the scarcity of accurate experimental data. As indicated by Spina et al., acquiring quality data in these flows is very difficult. A recent survey by Settles and Dodson(1994) exemplifies the current state of affairs. After a review of over one hundred shock/boundary-layer interaction studies with a freestream Mach number greater than 3.0, nineteen passed a criterion that they deemed necessary for turbulence model development. A second factor contributing to the lack of understanding of these flows is the inability of current and foreseeable-near-future computational techniques to perform direct numerical simulation of the turbulence for high-Reynolds-number flows. Many of the terms (e.g., the static pressure-velocity fluctuation correlations) that arise in the equations governing the transport of the second-order turbulent correlations cannot be measured. Hence, this coupling of experimental and computational limitations makes the study of high-speed high-Reynolds-number turbulence particularly arduous and highly empirical.

Although the flow physics associated with a supersonic turbulent boundary layer subjected to a pressure gradient are not currently fully understood, many of the flow features have been well characterized. For example, many of the observed differences between distorted supersonic and subsonic boundary layers can be explained in terms of the fluid-property changes across the boundary layer (Spina et al., 1994 and Smith and Smits, 1994). However, supersonic flows possess phenomena that have no incompressible counterparts. For example, wave (expansion or compression) boundary-layer interactions, where the longitudinal pressure gradients can lead to compression or dilatation which, in turn affects the velocity pressure and density fluctuations, are not present in subsonic flow. An extensive literature review of supersonic flow over curved surfaces is not presented here because of page limitations; instead, a brief synopsis of the salient flow physics is given. As indicated above, a comprehensive review of the literature can found in Spina et al. (1994) and Luker et al. (1997).

A pressure gradient in a supersonic flow can be generated basically in two ways -- wave-boundary layer interaction and streamline curvature. For the case of a curved wall, separation of the effects of streamline curvature and pressure gradient on the turbulent flow properties is difficult; however, for an imposed wave, the streamline deflection angle is usually very small; hence, the effects of pressure gradient can be isolated (Smith and Smits, 1994). The differences between the two methods make characterization of the strength of the perturbation tenuous. A number of characteristics have been proposed to classify the distortion strength caused by wall curvature [see Luker et al. (1997) for a brief listing]. Luker et al.

capitalized on a number of those definitions to establish the "global" parameter:

$$B = \frac{I_T}{(L_i / \delta_o)_T} \equiv \frac{\Sigma(I_p + I_\phi)}{\Sigma(L_i / \delta_o)} \qquad (1)$$

where $I_p = \ln(p_2/p_1)/\gamma$, $I_\phi = \Delta\phi$, L_i = length of the distortion, and δ_o = undisturbed boundary-layer thickness. The global parameter has the form of a nondimensional pressure gradient and makes use of data that are usually readily available to characterize the strength of the pressure gradient. It is important to note that B is not intended to be a true representation of the physics; rather, it is simply meant to be a useful way of classifying the overall strength of the distortion. For $|B| < 0.2$, the peak amplification of the Reynolds shear stress measured for the present wind-tunnel models as well as a number of other studies collapses onto a single curve given by $(\tau_{xt}^T - \tau_{xy}^0)/\tau_{xy}^0 \approx 10B$ (Luker et al., 1997).

The effects of the combined streamline curvature and pressure gradients on the turbulent flow features can be gleaned from the above correlation. For an adverse pressure gradient/concave curvature (i.e., B > 0), the turbulent shear stress is amplified. Thus, concave curvature and adverse pressure gradients have been deemed destabilizing, where the turbulence levels, wall shear stress, and heat transfer all increase. On the other hand, for favorable pressure gradients/convex curvature, the opposite trend is apparent. The effects of the present rather mild wall curvature (wall contours are given in the Facilities Section) on the turbulent flow features are rather pronounced, where the peak shear stress levels vary by approximately ± 100%.

Also, as indicated in Luker et al., practically all of the available data for this type of flow were obtained with hot-wire anemometry and, for a few cases, with Laser Doppler velocimetry (LDV). Hence, the spatial resolution for those studies was limited. Therefore, because of the dramatic effects on the turbulent flow and the importance of global information, the curved-wall experiments are well suited as a benchmark test case for developing and evaluating the digital, two-color, planar PIV technique.

1.3 Injection into a Supersonic Flow

Injection into a supersonic cross flow also has a number of practical applications; for example, thrust vector control, supersonic-combustion ramjet fuel injection, and boundary-layer control. The overall structure of the mean-flow field associated with injection into a supersonic cross flow has been the subject of much investigation. As a result of the large number of studies, the mean-flow physics of supersonic injection into a supersonic cross flow are reasonably well understood. As was the case for the curved-

wall background, an extensive literature review is not given here [see Bowersox (1997) for a reasonably comprehensive background]. A brief synopsis of the flow features is presented here.

First, injection into a supersonic freestream creates what is usually termed the interaction-shock, which generally separates the incoming boundary layer. Thus, the familiar lambda-shock boundary-layer interaction structure is generated. Because of the unsteady nature of the shock boundary layer interaction, the interaction shock position is also unsteady. As the jet emerges, it is turned downstream by the incoming high-momentum freestream. Also, as the underexpanded jet emerges, it expands to conditions requiring termination at a normal shock called the Mach disk (Schetz et al., 1967). Directly behind the injector, the flow is separated, followed by a reattachment of the flow and a recompression shock. Again because of the unsteady separation regions, the recompression shock position is also unsteady. A relatively strong counter-rotating vortex pair is present within the plume, which creates a distorted cartioid shaped plume. A smaller, weaker horseshoe vortex, similar to that generated by a wing-body junction, occurs at the injection-cross flow junction. It has also been documented that a vortex street results from the flow separation just downstream of the jet (Fric and Roshko, 1994). Finally, a fourth, near-field, exit ring-like vortex system has also been reported for low-speed flows (Perry et al., 1993).

The complicated nature and the important applications yield the supersonic jet into a supersonic cross flow an attractive Mie-scattering flow-visualization test case for both instantaneous images (pulse duration of 10 ns) and time-averaged exposures. Further, because of the inherent integration along the optical axis, the more conventional index-of-refraction-based flow-visualization techniques (e.g., shadowgraph, schlieren, and interferometry) are not well suited for three-dimensional jet flows. Hence, the present flow-visualization technique has the potential to illuminate important flow features that would not be discernible on refractive flow visualizations.

1.4 Research Goals

The main goal of the present research was to further develop and evaluate the performance of the digital, two-color, planar PIV technique for both flow visualization and quantitative mean and turbulent properties measurements. In particular, detailed planar PIV data were acquired for the curved-wall models described in Luker et al. (1997). The mean velocity and turbulence intensities obtained with the PIV technique were compared with the LDV data obtained by Luker et al. Hence, the potential benefits and limitations of the current technique were assessed. Secondly, the inherent flow-visualization aspects of the measurement apparatus was used for qualitative assessment of a very complex three-

dimensional flow by providing instantaneous and time-averaged flow visualizations.

2. FACILITIES

All tests were performed in the Air Force Institute of Technology pressure-vacuum supersonic wind tunnel (see Fig. 1). The freestream Mach number was 2.9, with a ± 0.02 variation across the test section. The settling-chamber pressure and temperature were maintained at 2.0 ± 0.03 atm, and $294 \pm 2K$, for all tests. The freestream Re/m was 15 x 10^6. The freestream turbulent kinetic energy was 0.016% of the mean specific kinetic energy. The test section was 6.35 x 6.35 cm in cross-section.

2.1 Curved-Wall Models

The curved-wall sections were built into the tunnel ceiling as shown in Fig. 1. The coordinate system was defined such that x was positive in the streamwise direction, and the origin was located at the nozzle throat. Since all measurements were made normal to the tunnel ceiling, y was defined as positive down and was zero at the test section ceiling; z completed the right-hand system. The contours started at x = 65.08 cm. The curved-wall contours were generated to match a cubic polynomial $\Delta h = a_0 + a_1 \Delta x + a_2 \Delta x^2 + a_3 \Delta x^3$, where Δh(cm) was relative to the tunnel ceiling and Δx(cm) = x - 60.0. The coefficients for each model are given in Table 1, and the wall contours (i.e., tunnel heights above the lower floor) are shown in Fig. 2. The favorable-pressure-gradient (FPG) model is given by the dashed line. For this model, the measurements were acquired normal to the curved wall at x = 71.5 cm. The adverse-pressure-gradient (APG) flow model is indicated by the solid line, where the measurements normal to the curved wall were acquired at x = 68.0 cm. The zero-pressure-gradient (ZPG) data were also taken at x = 71.5 cm downstream of the nozzle throat. These measurement locations were nominally 3500 momentum thickness heights downstream of the nozzle exit, where the boundary layer has been documented to be in a state of equilibrium (Bowersox and Buter, 1997). The boundary-layer and pressure-gradient parameters for the present flow are summarized in Table 2 (Luker et al., 1997).

2.2 Injector Wind-Tunnel Model

The injector model was built into the ceiling of the tunnel, as shown in Fig. 3; also shown is the coordinate system. The injectant gas was air at a Mach number of 1.8. The throat and exit diameters of the conical nozzle were 3.22 and 3.86 mm, respectively. The injector-

nozzle divergence angle was 0.83 deg. The injection angle was 25 deg. relative to the freestream. Since the injector was at an angle, the exit port was elliptical, with 3.86 and 9.14 mm minor and major axis lengths, respectively. The injectant total pressure and temperature were 3.8 ± 0.03 atm and $294 \pm 2K$, respectively. Table 3 summarizes the injection parameters.

3. PIV PROCEDURES

The two-color PIV system employs color for temporal marking of the seed particles in the flow field. The green (532-nm) laser output from a frequency-doubled Nd:YAG laser and the red (640-nm) laser output from a Nd:YAG-pumped dye laser (DCM dye) were combined by a dichroic beam splitter and directed through sheet-forming optics. The laser-sheet energy was typically 20 mJ/pulse, with a thickness of < 1 mm at the test section. The temporal delay between the two lasers is a function of gas velocity, optical magnification, and interrogation spot size. In the present experiments, the time delay between the two color lasers was set at 300 nsec.

The flow was seeded with sub-micron size particles, and the Mie scattering from the seed particles was recorded on a Kodak DCS 460 CCD array. This CCD sensor has a resolution of 3060 x 2036 pixels, and each pixel is 9-μm square. A 105-mm micro lens with an f-number of 5.6 is used to record the images.

The Kodak DCS 460 sensor utilizes a single CCD to record color images. This is accomplished by coating each camera element (pixel) with a red, a green, or a blue filter. Because the green color yields the best measure of brightness, the green pixels make up 50% of the camera sensor. The remaining 50% is equally divided between red and blue pixels. Achieving a full RGB image requires a multi-step process in which red, green, and blue pixels are interpolated. First the 8-bit 3072 x 2048 image is converted into a 12-bit image by scaling with a gray response curve. Next, a pattern correction of the camera image is undertaken to account for variation in pixel-to-pixel sensitivity. The pattern correction is unique for each individual camera. Interpolation of the compressed image into three 3072 x 2048 red, green, and blue images is achieved using Kodak proprietary algorithms. Because green captures the luminance levels that can translate across to the red and blue planes, the green interpolation is carried out first, followed by the red and blue. The RGB images are then processed through both a toe-shoulder and gamma look-up table. The result is a color-corrected full RGB image that is used for PIV analysis. Software for the decompression of the Kodak camera image before processing has been developed by ISSI, and this software subdivides the image into strips corresponding to the image width and the interrogation region height. The strip is

expanded, processed, and then discarded to eliminate the need for large disk storage.

The velocity field from the digital PIV images was obtained using a cross-correlation technique. The correlation function was calculated over small segments (interrogation domains) of the PIV image. The dimensions of each interrogation domain are dependent on particle density, estimated local velocity gradients, particle-image size, and desired spatial resolution. The maximum displacement of each particle must be less than one-half the interrogation spot size. In the present experiments, the interrogation domain measured 128 x 128 pixels, corresponding to 1.76 x 1.76 mm in the measured flow. For enhancing the overall resolution, the interrogation domains were overlapped by one-half the domain size. The peak of the correlation map corresponds to the average velocity displacement within the interrogation spot. An intensity-weighted peak-searching routine was used to determine the exact location of the peak to sub-pixel accuracy. The number of particle pairs normally necessary to ensure a desirable signal-to-noise ratio was reduced to four or five pairs when the cross-correlation analysis was employed.

The calibration of the CCD system was investigated using solid-body translation and rotation, and the details were given by Gogineni et al. (1996). The uncertainty in the velocity measurements was estimated to be ± 1%.

4. RESULTS AND DISCUSSION

4.1 Jet in a Cross Flow

Both instantaneous and time-averaged Mie-scattering visualizations of the supersonic jet into a supersonic cross flow are shown in Fig. 4. As indicated by the instantaneous image in Fig. 4(a), the present flow-visualization technique provides valuable qualitative information concerning the large-scale structures. The time-averaged image is useful for defining penetration and plume dispersion.

4.2 Boundary Layer Flows

For demonstrating the applicability of PIV for measuring supersonic flow quantities particularly under the influence of pressure gradients, three pressure gradients were examined -- a flat-plate (ZPG), an FPG and an APG. The flow field from these models has been studied extensively (Bowersox and Buter, 1996; Luker et al., 1997) by LDV. These LDV data formed the basis for validating the PIV results.

The CCD images were processed through the data-reduction procedure discussed earlier and ensemble averaged to create a single image. The only difference between the three models was the number of images averaged. The number of images used to create the averaged image was 25 for the ZPG, 30 for the APG, and 25 and 93 for the FPG. Two samples sizes were used for the FPG data to examine the effect of sample size on result convergence. Flow visualizations of supersonic turbulent boundary layers with pressure gradients are shown in Fig. 5. Figures 5(a) and 5(b) cover the top and bottom walls of the wind tunnel and display the boundary-layer structure under pressure gradients compared to the no gradient (bottom wall). As can be inferred from these visualizations, these rather mildly curved walls dramatically affect the overall structure of the boundary layer. For example, the boundary-layer thickness for the APG model decreased by about 50%. The magnified view of the boundary-layer structure near the top wall can be seen in Fig. 5(c) for the ZPG condition, which shows that the present technique provided detailed and clear images of the turbulent-boundary-layer structures.

The contours from the ensemble-averaging are presented in Figs. 6, 7, and 8 for the ZPG, FPG and APG, respectively. The ordinate axis of these figures has been non-dimensionalized by the boundary-layer thickness normal to the location indicated by 'LDV measurement location.' Contours of constant velocity and turbulence intensity have been plotted on these figures. Locations where data were insufficient for proper computation of velocity or turbulence intensity are indicated by diamond shapes with locally high velocity or turbulence intensity gradients. All PIV profiles were extracted from a line normal to the wall starting at the location labeled 'LDV measurement location.'

The ZPG results are plotted in Figs. 6a and 6b. The velocity gradient shown in Fig. 6(a) is uniform and smooth throughout the boundary layer. This shows that even a relatively small number of images can adequately resolve mean flow quantities. The turbulence intensity for the ZPG is plotted in Fig. 6b. As is the case with the velocity contours, the turbulence-intensity contours are smooth and uniform.

The FPG results are plotted in Figs. 7(a) and 7(b). Fig. 7(a) shows the effect of the favorable pressure gradient on the velocity profile. Both the boundary-layer height and freestream velocity are large compared to the corresponding ZPG values. For example, a large area of velocity > 600 m/sec that is evident downstream of the LDV measurement location did not appear in the ZPG data. The effect of the FPG on turbulence intensity is shown in Fig. 7(b). The overall FPG turbulence intensity decreased relative to that of the ZPG. The near-wall value is ~ 8%. This is a reduction of ~ 20% from the ZPG result.

The APG results are plotted in Figs. 8(a) and 8(b). Fig. 8(a) shows the effect of the adverse pressure gradient on the velocity profile. The APG boundary layer is not so thick as the ZPG and FPG boundary layers. This is an expected result of the compression that occurs in an APG flow. The effect of the APG on turbulence intensity is shown in Fig. 8(b). The near-wall turbulence intensity is

higher than that of either the ZPG or FPG, with a peak value on the order of 24%.

Since LDV acquires data at only one point and PIV provides data along an entire plane, a line of data was extracted from the PIV images to enable comparison with the LDV results from Luker et al. (1997). The PIV data points were extracted along a line normal to the tunnel wall with the origin of the lines as indicated in Figs. 6 - 8. The profile comparisons of the PIV and LDV results are presented as Figs. 9 - 11. In the velocity comparison plots, the x-axis is normalized by the freestream velocity.

Figures 9(a) and 9(b) present ZPG comparisons for mean velocity and turbulence intensity, respectively. As shown in Fig. 9(a), the PIV and LDV results agree favorably for the velocity profile in the freestream and inner region of the boundary layer. However, PIV slightly underpredicts the velocity profile in the upper region of the boundary layer.

The turbulence intensity comparison is presented in Fig. 9(b). The PIV and LDV results agree favorably in the boundary layer but diverge for $y/\delta > 1.0$. For $y/\delta > 1$, the LDV predicts a turbulence intensity of 1%, while PIV predicts 3%. This discrepancy is repeatable as it appeared in each pressure gradient case and was most likely due to the different signal-to-noise ratios in the measurement techniques.

Figures 10(a) and 10(b) show velocity and turbulence-intensity comparisons for the FPG case. The data from the two different sample group sizes were reduced to gauge the effect of sample size on the results. The sample sizes chosen were 25 (comparable to the ZPG and APG data) and 93 (the total number of FPG images acquired). As shown in Fig. 10(a), the mean-velocity results generated from the 25 images, the 93 images, and the LDV data are in close agreement. Again this demonstrates that only a few images are necessary for accurate measurement of mean-flow quantities.

As shown in Fig. 10(b), the values of turbulence intensity are similar for the 25 and 93 image sample groups. The PIV turbulence intensity matches the LDV data in the near-wall region of the boundary layer. However, as indicated above, the signal-to-noise ratio of the present PIV setup was insufficient to resolve the low freestream turbulence levels. The spikes at $y/\delta = 1.5$ most likely resulted from a scratch in the window or some reflection.

Figures 11(a) and 11(b) present PIV and LDV comparisons for APG. As with the FPG and ZPG, the mean-velocity contour derived from PIV results matches with the LDV data throughout the boundary layer. Of interest is the fact that PIV was able to resolve the velocity closer to the wall than the LDV.

Of the three pressure-gradient cases discussed, the comparisons of PIV and LDV is the poorest for APG turbulence intensity. The APG turbulence-intensity data

are presented in Fig. 11(b). PIV consistently predicts a higher turbulence intensity throughout the boundary layer. This is possibly the result of decreased signal-to-noise ratio that resulted from the smaller boundary layer; increasing the magnification may have improved the agreement here.

5. ACKNOWLEDGMENT

6. REFERENCES

Adrian, R. J., "Particle Imaging Techniques for Experimental Fluid Mechanics," *Ann. Rev. Fluid Mech.*, Vol. 23, 1991, pp 261-304.

Bradshaw, P., "The Effect of Mean Compression or Dilatation on the Turbulence Structure of Supersonic Boundary Layers," *J. Fluid Mech.*, Vol. 63, Part 3, 1974, pp. 449-464.

Bowersox, R., "Turbulent Flow Structure Characterization of Angled Injection into a Supersonic Cross Flow," *Spacecraft and Rockets*, In Print, 1997.

Bowersox, R. and Buter, T., "Mass-Weighted Turbulence Measurements in a Mach 2.9 Boundary Layer Including Mild Pressure Gradients," *AIAA J.*, In Print, 1996.

Fric, T. and Roshko, A., "Vortical Structure in the Wake of a Transverse Jet," *J. Fluid Mech.*, Vol. 279, Nov., 1994, pp. 1-47.

Gogineni, S., Trump, D., Goss, L., Rivir, R., and Pestian, D., "High Resolution Digital Two-Color PIV and its Application to High Freestream Turbulent Flows," Proceedings of the 8th International Symposium on Applications of Laser Techniques to Fluid Mechanics, Lisbon, Portugal, Vol. 1, 1996, pp 18.2.1-18.2.8.

Luker, J., Hale, C., Bowersox, R., "Experimental Analysis of the Turbulent Shear Stresses for Distorted Supersonic Boundary Layers," AIAA-97-0426.

McCann, G., and Bowersox, R., "Experimental Investigation of Supersonic Gaseous Injection into a Supersonic Freestream," *AIAA J.*, Vol. 34, No. 2, 1996, pp. 317-323.

Perry, A., Kelso, R., and Lim, T., "Topological Structure of a Jet in a Cross-Flow," AGARD-CP-534, NATO, 1993, pp. 12.1-12.7.

Schetz, J., Hawkins, P, and Lehman, H., "Structure of Highly Underexpanded Transverse Jets in a Supersonic Stream," *AIAA Journal*, Vol. 5, No. 5, 1967, pp. 882-885.

Settles, G. and Dodson, L, "Supersonic and Hypersonic Shock/Boundary Layer Interaction Database," *AIAA J.*, Vol. 32, No. 7, 1994, pp. 1377-1383.

Smith, D. and Smits, A., "The Effects of Streamline Curvature and Pressure Gradient on the Behavior of Turbulent Boundary Layers in Supersonic Flow," AIAA-94-2227, 1994.

Spina, E., Smits, A., and Robinson, S., "The Physics of Supersonic Turbulent Boundary Layers," *Ann. Rev. Fluid Mech.*, Vol. 26, 1994, pp. 287-319.
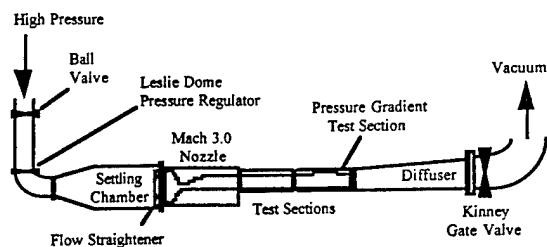
Fig. 1 Schematic of the AFIT pressure-vacuum
supersonic wind tunnel
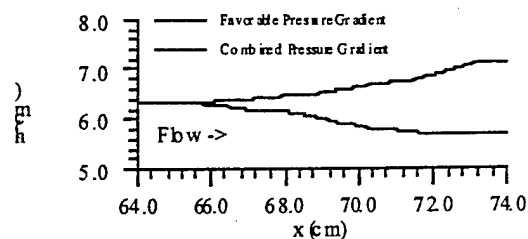
Fig. 2 Schematic of curved wall contours.
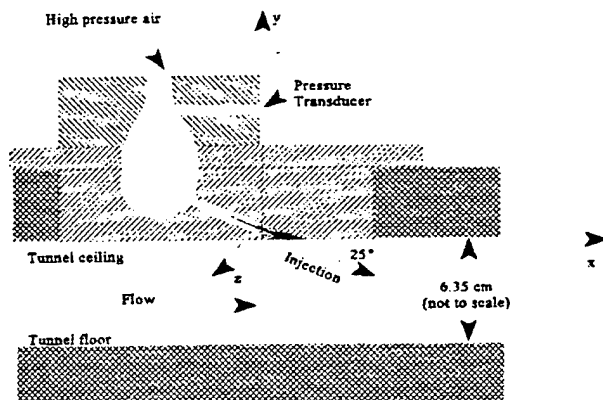
Fig. 3 Schematic of the injector model

Table 1 - Model Contours

Model	a_0 x 1	a_1 x 10	a_2 x 100	a_3 x 1000
FPG	-0.2078	0.8970	-0.9476	-0.03598
APG	1.186	-5.410	7.478	-2.800

Table 2 - Summary of Local Boundary Layer and Pressure Gradient Parameters (Luker et al., 1997)

Model	M_∞	δ(mm)	δ^*/δ	θ/δ	H	Re_θ	C_f[a]	β	B[b]
ZPG	2.79	9.9	0.062	0.050	1.24	1.1×10^4	0.0016	0.02	0.0
FPG	2.91	11.9	0.075	0.056	1.34	1.5×10^4	0.0011	-0.5	-0.08
APG	2.72	9.1	0.083	0.074	1.12	1.2×10^4	0.0022	1.0	0.1

[a]Estimated via the Couette flow assumption
[b]Based on Prandtl-Meyer theory and local wall inclination

Table 3 - Injection Parameters

$P_{tj}/P_{t\infty}$	P_j/P_∞	u_j/u_∞	ρ_j/ρ_∞	$(\rho u)_j/(\rho u)_\infty$
1.5	8.2	0.8	5.0	4.0	3.2

a) Instantaneous

b) Averaged
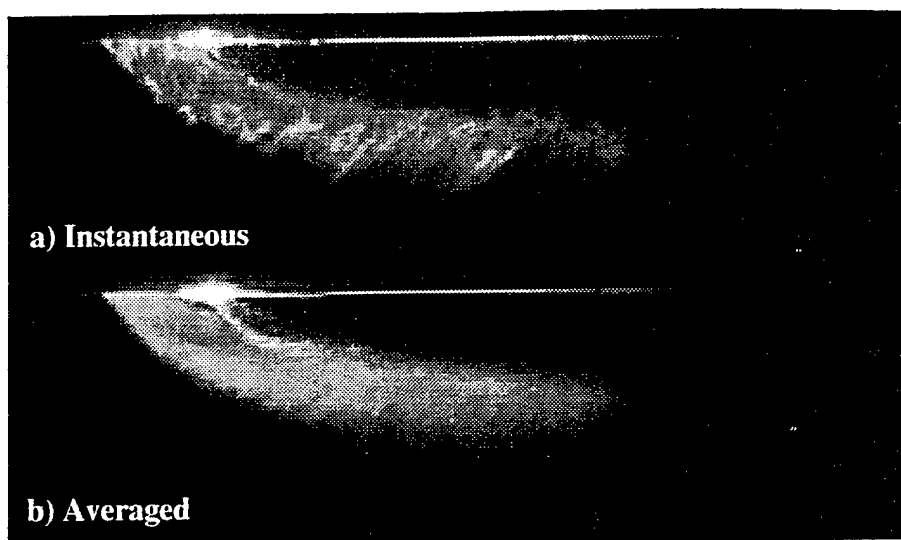
Figure 4. Mie scattering visualization of supersonic jet (M = 1.6) injection into a supersonic cross flow (M = 2.9)

Favorable pressure gradient

Adverse pressure gradient

x = 70 cm   Wall   x = 72 cm

Flow

Zero pressure gradient
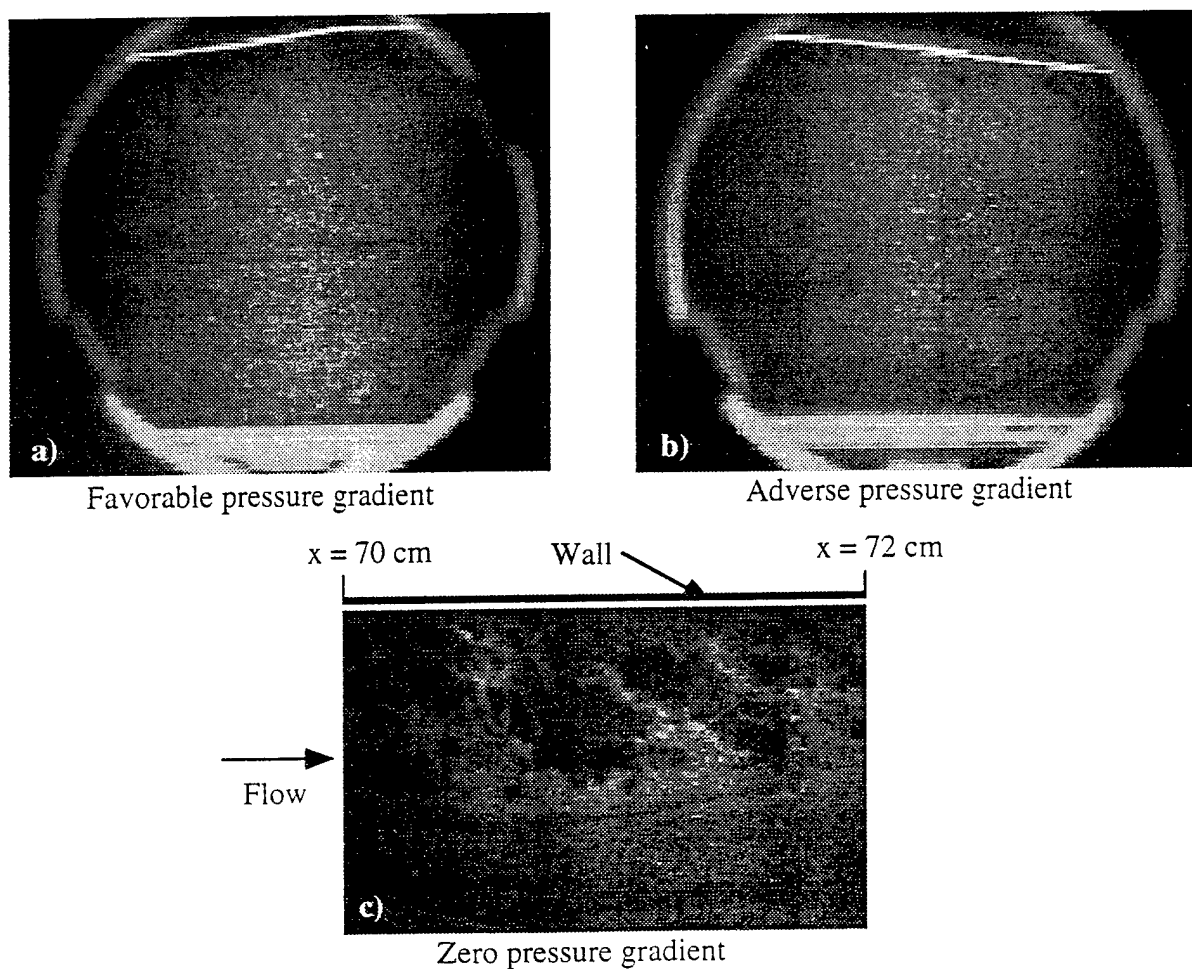
Figure 5. Mie scattering visualization of supersonic turbulent boundary layer with pressure gradients
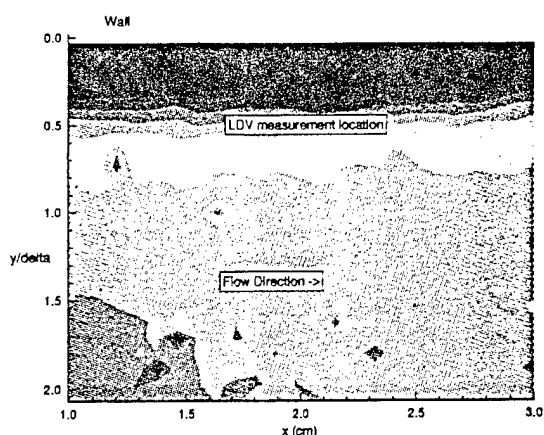
Figure 6a: ZPG U Velocity Contours - 25 Samples
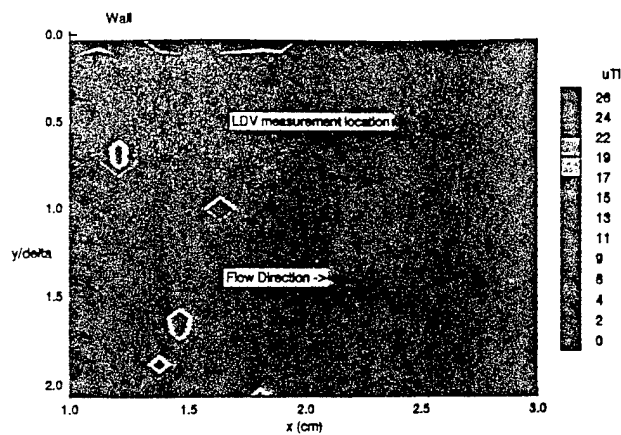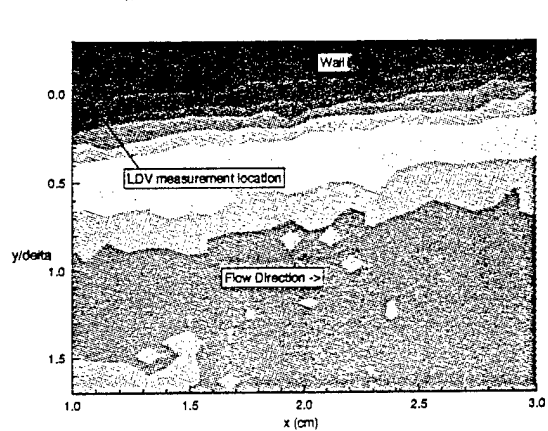

Figure 6b: ZPG U Turbulence Intensity Contours (%) - 25 Samples

Figure 7a: FPG U Velocity Contours - 93 Samples
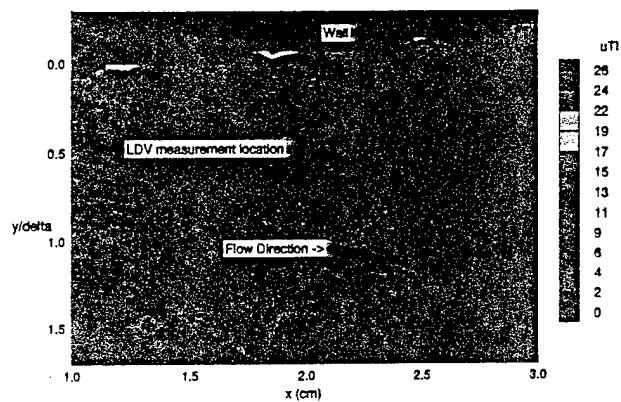
Figure 7b: FPG U Turbulence Intensity Contours (%) - 93 Samples
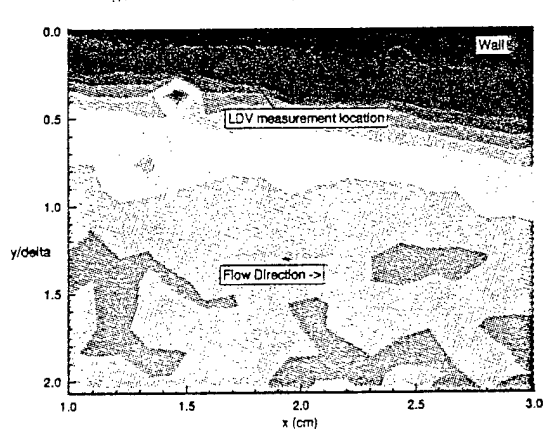
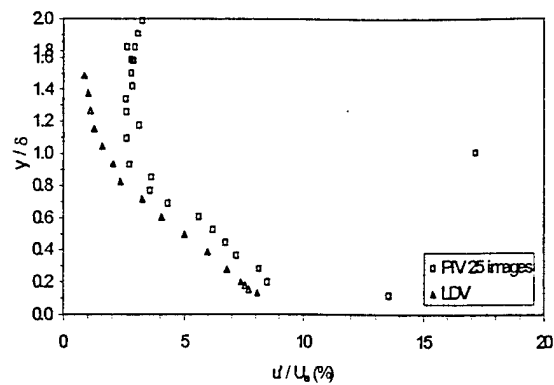Figure 8a: APG U Velocity Contours - 30 Samples
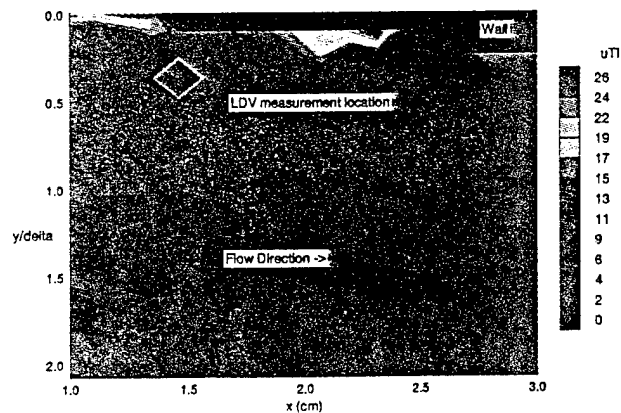
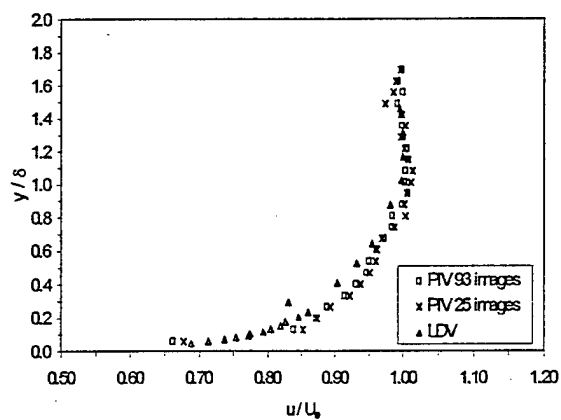Figure 8b: APG U Turbulence Intensity Contours (%) - 30 Samples

63
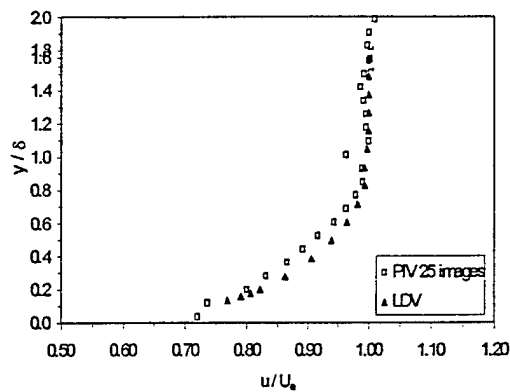
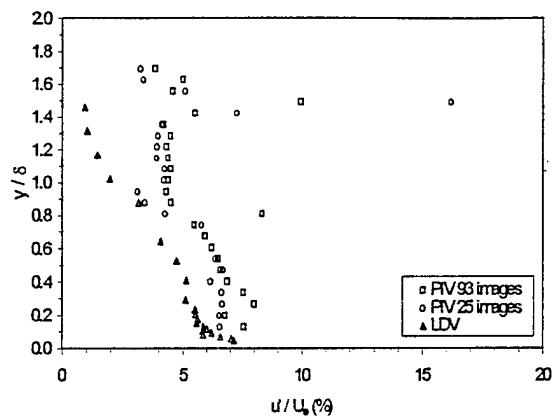a)   b)

Figure 9: ZPG Mean Velocity and Turbulence Intensity Profile

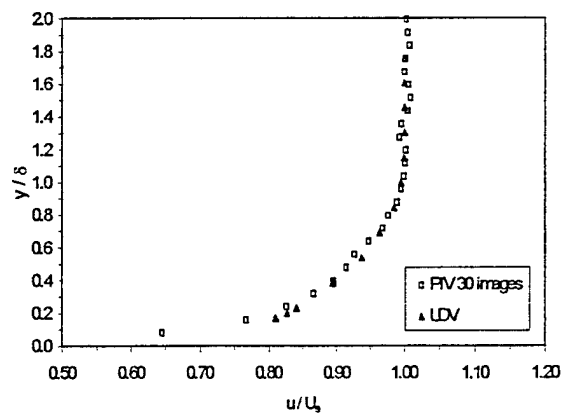
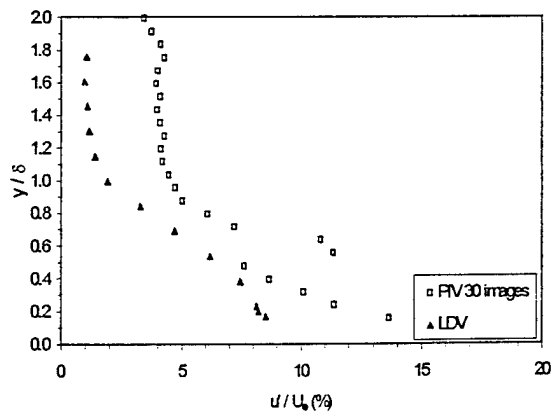a)   b)

Figure 10: FPG Mean Velocity and Turbulence Intensity Profile

a)   b)

Figure 11: APG Mean Velocity and Turbulence Intensity Profile